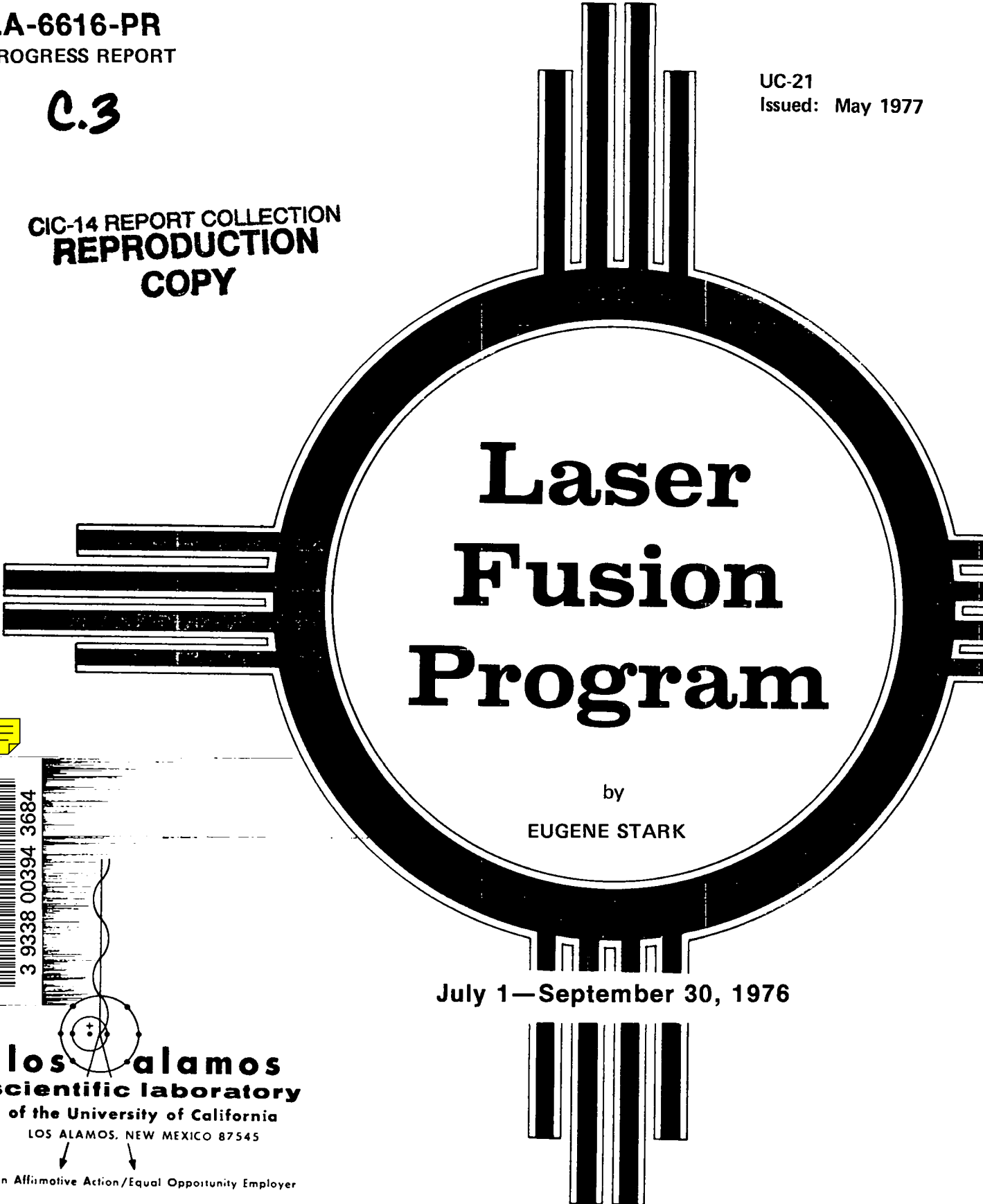


LA-6616-PR
PROGRESS REPORT

C.3

UC-21
Issued: May 1977

CIC-14 REPORT COLLECTION
**REPRODUCTION
COPY**



Laser Fusion Program

by
EUGENE STARK

July 1—September 30, 1976



los alamos
scientific laboratory
of the University of California
LOS ALAMOS, NEW MEXICO 87545

An Affirmative Action/Equal Opportunity Employer

UNITED STATES
ENERGY RESEARCH AND DEVELOPMENT ADMINISTRATION
CONTRACT W-7405-ENG. 36

LOS ALAMOS NATL. LAB. LIBS.
3 9338 00394 3684

The four most recent reports in this series, unclassified, are LA-5919-PR, LA-6050-PR, LA-6245-PR, and LA-6510-PR.

This work was supported by the US Energy Research and Development Administration, Division of Laser Fusion.

Printed in the United States of America. Available from
National Technical Information Service
U.S. Department of Commerce
5285 Port Royal Road
Springfield, VA 22161
Price: Printed Copy \$5.00 Microfiche \$3.00

This report was prepared as an account of work sponsored by the United States Government. Neither the United States nor the United States Energy Research and Development Administration, nor any of their employees, nor any of their contractors, subcontractors, or their employees, makes any warranty, express or implied, or assumes any legal liability or responsibility for the accuracy, completeness, or usefulness of any information, apparatus, product, or process disclosed, or represents that its use would not infringe privately owned rights.

CONTENTS

Abstract	1
Summary and Program Review	2
I. CO ₂ Laser Program	2
Single-Beam System (SBS)	7
Two-Beam System (TBS)	8
Eight-Beam System (EBS)	10
High-Energy Gas Laser Facility (HEGLF)	15
CO ₂ Laser Technology	20
II. New Laser Research and Development	31
Experimental Studies of Rare Gases and Rare-Gas Oxides	31
Metal Vapor Lasers	35
Optical Damage Studies	39
III. Laser Fusion — Theory, Experiments, and Target Design	43
Target Experiments at 1.06 and 10.06 μm	43
Theoretical Studies of Laser Fusion	45
Target Design	49
IV. Laser Fusion Target Fabrication	51
Introduction	51
High-Pressure DT Gas-Filled Targets	51
Cryogenic Targets	59
V. Target Diagnostics	65
Introduction	65
X-Ray Microscope Development	65
Proximity-Focused X-Ray Streak Camera	65
Optical Diagnostics of Target Plasmas	66
Target-Plasma Ion Measurements	69
Calibration of Ion Calorimeters	70
Laser Stabilization and Synchronization	70
Stereoscopic Polarization Camera	71
Thin-Film Scintillator Detectors	72
Soft X-Ray Diffraction Spectrometer	72
Plastic Track Detectors	72
VI. Applications of Laser Fusion — Feasibility and Systems Studies	75
Studies of Magnetically Protected Laser Fusion Reactor Concept	75
Studies of Ion-Beam Fusion Concepts	76
Fusion Pellet Output Parameter Studies	79
Systems Analysis Computer Program Development	79

LOS ALAMOS NATIONAL LABORATORY



3 9338 00394 3684

VII. Resources, Facilities, and Operational Safety	80
Manpower Distribution	80
Facilities	80
Operational Safety	80
VIII. Patents, Presentations, and Publications	81
Patents Issued	81
Presentations	81
Publications	82

Progress Report on the

LASL LASER FUSION PROGRAM

July 1 – September 30, 1976

by

Eugene Stark and the Laser Division Staff

Edited by

Frederick Skoberne

ABSTRACT

Progress in the development of high-energy short-pulse CO₂ laser systems for fusion research is reported. The use of saturable absorbers to suppress parasitic oscillations in the Two-Beam System was studied. Initial gain measurements were made on the first amplifier module in the Eight-Beam System, and system construction continued. Progress in the HEGLF prototype program is reported, and advances in CO₂ laser and diagnostics technology are described.

Our understanding of the Ar-O₂ electron beam-controlled discharge is described. Our progress in rare-gas kinetics, preliminary gain/absorption measurements in Hg⁺, the use of heat pipes for metal-vapor lasers, and damage studies at 0.335, 0.532, and 1.064 μm are reported.

Experimental and theoretical results that bear on wavelength scaling in laser fusion are presented. Studies of laser-plasma interface stability and self-generated magnetic fields, as well as an important modification to LASNEX, are described. Advances in fabrication and characterization of laser fusion targets, deposition of target coatings, and formation of uniform DT ice layers are summarized. New results on optical and other target-interaction diagnostics are described.

New results on studies of the magnetically protected reactor concept, and on a study of one conceptual ion-beam fusion cavity are given.



INTRODUCTION

The Laser Fusion Program was established at Los Alamos in 1969, with the initiation of research into high-pressure CO₂ laser systems. Within the next few years, we developed the electron beam-controlled CO₂ laser amplifier and expanded our efforts into a complete, balanced research program of laser fusion for energy and military applications.

Our long-range goal is the completion of a comprehensive set of experimental and theoretical studies to test the scientific and engineering feasibility of using laser-induced microexplosions of small fusion pellets to produce heat for commercial electric-power generation and other applications.

Basic elements of this work include: the development of efficient, short-pulse, high-energy laser systems to illuminate small fuel pellets; advanced laser research; the design and fabrication of fusion pellets; the conduct, diagnosis, and analysis of laser-target interaction experiments; theoretical studies of the physics of laser-matter interactions; and systems and applications studies.

Significantly, our Laser Fusion Program has contributed to the initiation of other important programs, ranging from a large laser-isotope separation effort and a joint development program with Union Carbide Corp.'s Y-12 plant on mirror fabrication by micromachining -- expected to have a wide impact on the optics industry -- to a small project on basic research into photosynthesis.

CO₂ LASER PROGRAM

It is generally agreed that the high energies (several hundred kilojoules), short pulse lengths (0.25 to 1.0 ns), and smooth, focusable beams required for laser fusion can be achieved efficiently and repetitively only by gas laser systems. Economical systems require large-aperture beams to avoid laser damage to the optical components. Only gas lasers can operate in such a large-aperture configuration. Historically, the CO₂ laser has received major emphasis in our development effort be-

cause of its high efficiency and its well-developed short-pulse generation and amplification technology. We have chosen a sequence of progressively more powerful CO₂ laser systems, requiring with each new system a reasonable extension of the state of the art while providing the capability for important new target experiments. Our existing and planned CO₂ laser systems include the following.

Single-Beam System (SBS)

This system includes an oscillator and four electron beam-controlled amplifiers. Three amplifiers were used in the first 10.6- μm laser target experiments early in 1973, delivering 10 J in a 1-ns pulse. Since then, the SBS has been upgraded to generate a maximum of 250 J in 1-ns pulses and to deliver 180 J to a target with a peak intensity of $7 \times 10^{14} \text{ W/cm}^2$. The SBS also serves as a developmental test bed for new laser system components, e.g., oscillators, isolation schemes, and optical systems. Progress is summarized as follows.

- An overhaul of the fourth amplifier was completed.
- Construction began on a beam alignment system for complex targets, with an estimated pointing resolution of 20 μm .
- During the overhaul of the fourth amplifier, a number of important target and diagnostics experiments were carried out with 10-J pulses.

Two-Beam System (TBS)

The heart of this system is a dual-beam amplifier module, in which two gain chambers share one cold-cathode electron beam ionization gun. The oscillator pulse is split into two beams, each of which is amplified in three passes through a single gain chamber. The TBS was originally intended only as a prototype for the Eight-Beam System. However, the need for additional target experiment capability at higher intensities became apparent, and the TBS program was enlarged to include a target irradiation capability. The design point for the TBS is a total output of 2 to 4 TW, or 1.25 kJ per beam

in a 1-ns pulse. Because of several accidents, the only major experimental progress was the installation and optimization of saturable absorbers placed between the power amplifier and the target chamber to suppress parasitic oscillations in which the target is a critical element.

Eight-Beam System (EBS)

This system will include an oscillator, preamplifiers, and four dual-beam amplifiers, with a design-point performance of 10 to 20 TW in a 0.25- to 1-ns multiline pulse (maximum energy output, 10 kJ in 1 ns). This design point should be reached in 1977, with target experiments to begin in 1978. Progress is summarized as follows.

- System assembly is on schedule. Small-signal gain measurements were completed on one side of the first amplifier module, and assembly of the multiline front end is in progress. Development of computer software and installation of the control systems are proceeding well.

- Testing has begun on a new triple-pass optics system for the power amplifiers.

High-Energy Gas Laser Facility (HEGLF)

The HEGLF, planned for completion in 1981, represents a major step in laser fusion research. This system is expected to demonstrate scientific breakeven (i.e., fusion yield equal to incident laser pulse energy) and will serve as a major test bed for the study of a variety of target designs. It will be subsequently available for laser engineering optimization studies for a prototype reactor. The power stage of this system will consist of six large annular amplifiers, which will yield a total energy of 100 kJ in a 1-ns pulse, or 100 to 200 TW -- the latter value is for a 0.25-ns pulse. The associated target irradiation facility will permit the symmetric irradiation of a fusion pellet by the six beams.

We feel that this program represents a least-risk path to scientific breakeven. The system represents a reasonable extrapolation of existing technology and engineering. Major subsystems will be evaluated in a prototype program. Progress is summarized as follows.

- Experimental studies, performed under contract to LASL, verified that current control in a cold-cathode electron gun can be effected by a self-biasing grid.

- Power supply modeling showed the advantage of single-section Guillemin networks.

- Title I drawings and specifications prepared by the Architect-Engineer were accepted by ERDA.

CO₂ Laser Technology

Scientific support for our CO₂ system development programs includes studies of short optical-pulse generation techniques, system isolation to prevent parasitic oscillations, laser system diagnostics, and other work to improve and optimize system performance. For example, oscillator pulses containing multiple rotational transitions will increase both pulse energy and peak intensity significantly and will reduce the risetime. Target deposition of only 50 μJ by parasitic oscillations or by laser precursor pulses can melt the target prior to the arrival of the main pulse. System isolation must prevent this unwanted energy deposition as well as alleviate the problem of optical damage by amplified reflections from the target. Extensive efforts in temporal and spatial beam diagnostics and in beam improvements are under way to achieve a small, focused spot size. The following progress is significant:

- Our multiline CO₂ oscillator was modified to provide reliable four-line operation producing an output pulse 50 ns in duration (FWHM) with a peak power of 40 MW (the electro-optic shutter system can then switch out a short pulse from this output).

- Our first spatial filters were found to have damage thresholds more than an order of magnitude above the design point.

- Preliminary design concepts for the automatic alignment of the Eight-Beam System were developed.

- Development of laser system isolation continued, with very promising results for plasma breakdown concepts and narrowband saturable absorbers.

- We used our 5-GHz oscilloscope and free-induction pulse generator to evaluate the response of fast 10- μm detectors, with very promising results.

NEW LASER RESEARCH

In the early years of laser fusion research, it was felt that the "ideal" short-pulse laser for fusion research had not yet been invented. Its desired characteristics included high efficiency, visible or near-uv output, and a small-gain cross section coupled with high-density energy storage. However, recent experimental and theoretical results at CO_2 laser wavelengths may relax the projected requirement for a shorter wavelength.

Our efforts in new lasers are concentrated in three areas: fundamental investigations of kinetic processes and laser excitation methods, investigation of related technology areas, and establishment of a general experimental capability in electrical discharges and laser kinetics measurements. Our major emphasis has been on Hg_2 and on rare-gas oxides (to produce the green auroral line of atomic oxygen). The following progress is noteworthy.

- We have developed an initial data base for Ar- O_2 electron beam-controlled discharges.

- Initial gain/absorption measurements have been carried out at 325 nm in Hg_2^* .

- We have obtained new results on the kinetics of krypton and xenon and their excited and molecular states' transfer kinetics.

- We have refined our perspective on the applicability of heat pipes to metal-vapor lasers.

- Laser-damage measurements on refractory-oxide thin films were made at 0.335, 0.532, and 1.064 μm . We developed scaling laws for the damage

thresholds: multiphoton absorption appears to be important at the shortest wavelength.

LASER FUSION--THEORY, EXPERIMENTS, AND TARGET DESIGN

The laser fusion program is a coordinated effort in theory, experiment, and target design. Because the interaction of high-intensity laser pulses with target plasmas represents a new regime of physics not previously studied in detail, there have been many uncertainties in modeling the relevant processes. Experimentally, we require precise spatial and temporal resolutions, the spectra of emitted particles and radiation, as well as a complete characterization of the incident laser pulse. These experiments are conducted to test theoretical models and often lead to major modifications of theory. Theoretical efforts examine, for example, the various light-absorption mechanisms, hydrodynamic motion and instabilities, energy-transport mechanisms, and the deposition of nuclear reaction products. In turn, target design efforts must take account of our present theoretical understanding and of problems that may have arisen with previous designs. Significant progress was made in various areas.

- We have developed a model for determining the hydrodynamic velocity of the critical density surface and find it to be independent of wavelength at a constant intensity. For a laser pulse with peak intensity of 10^{15} W/cm^2 , this velocity is less than 10^7 cm/s during most of the laser pulse.

- Measurements of the silicon K_α radiation from layered targets (aluminum over silica), as a function of aluminum thickness, have verified previous results on hot-electron temperature and transport.

- Calculations with the simulation code WAVE show a $\lambda^{1/2}$ scaling of hot-electron temperature.

- We developed a simple analytic model of self-generated \bar{B} fields, which agrees with more detailed simulation calculations.

- We have added the important ponderomotive force to the LLL target-design code, LASNEX.

LASER FUSION TARGET FABRICATION

Fabrication and characterization of target pellets are important areas of supporting technology in our laser fusion program. Small, often complex, target pellets must be fabricated to strict specifications, e.g., filling a sphere to several hundred atmospheres with DT and depositing a uniform DT-ice layer on the inside of a microballoon. The characterization of completed pellets is also an important and challenging task. Our progress in this effort included the following.

- We have improved our characterization of glass microballoons (GMBs) in two areas. We developed a new two-axis device for interferometer examination of the entire surface of GMBs. We also obtained an x-ray resolution target for precise calibration of our x-ray microradiography.
- We improved the fabrication of freestanding plastic spheres and cylinders by improving the surface finish of the metal mandrels, onto which the plastic is deposited.
- We obtained considerable data on chemical vapor deposition of molybdenum from Mo(CO)_6 . Standards for coating stress and surface smoothness were developed for this work.
- Our fast isothermal freezing technique became operational, advancing our ability to condense uniform, transparent, solid layers of DT onto the inside surface of GMBs.

TARGET DIAGNOSTICS

Measurements of laser-plasma interactions, which may last from 50 ps to 1 ns, impose severe constraints on the diagnostics, requiring much equipment to be designed in-house and pacing the state of the art in many areas. Progress in diagnostics development included the following.

- We have tested the dynamic range of the proximity-focused x-ray streak camera, and have found it to be in excess of 100. With a better image intensifier, it is expected to achieve a dynamic range $>10^3$, yielding information from both the target interior and the target surface.
- We have designed a two-grating interferometer for use in studying steep density profiles. Our analysis code has indicated that quantitative data will be obtained if the probe light has a wavelength $\approx .25 \mu\text{m}$.
- We have analyzed the possibility of using the angular deviation of light as a diagnostic probe of steep density gradients. We estimate that the Abel inversion will have reasonable accuracy for deviations $<14^\circ$.
- An extensive study of the proper handling and storage of plastic track detectors was concluded with the assistance of Washington State University.
- We have built a stereoscopic polarization camera to photograph the second-harmonic light emitted in a $1.06\text{-}\mu\text{m}$ target experiment, with a resolution of 160 line pairs/mm.

APPLICATIONS OF LASER FUSION -- FEASIBILITY AND SYSTEMS STUDIES

Our feasibility and systems studies are performed to analyze the various commercial and military applications of laser fusion, and to identify technological problems requiring long-term development. Analysis, optimization, and tradeoff studies are performed on conceptual power-plant designs, and alternative applications of laser fusion are investigated. Progress made in recent studies has included the following.

- We have continued studies of the magnetically protected reactor concept. We used the computer code LIFE to optimize the energy-sink surface shape to make sputtering by energetic ions as nearly uniform as possible over the reactor cavity

surface. We found carbon to be the best material choice for the energy-sink surface because of its x-ray attenuation characteristics, its physical properties, and the atomic number dependence of sputtering.

● The most widely accepted laser fusion cavity-protection concepts may not be applicable to ion-beam fusion, because they may interfere with ion-beam transport. We completed a preliminary

study of the use of solid ablative material as a reactor cavity liner for ion-beam fusion. A carbon liner for a cavity of 10-m radius was studied, but sputtering by energetic ions was found to be unacceptable.

These and other results of our efforts during the third quarter of 1976 are discussed in detail in the following sections.



I. CO₂ LASER PROGRAM



The research and development programs on high-energy short-pulse CO₂ lasers were begun at LASL in 1969. Three large systems are now either operating or are being installed. The Single-Beam System (SBS), a four-stage prototype, was designed in 1971 and has been in operation since 1973, with a peak output energy of 250 J in a 1-ns pulse, and a peak on-target intensity of 7.0×10^{14} W/cm². Target experimentation has begun on the Two-Beam System (TBS), which will ultimately generate pulses of 2 to 4 TW for target-irradiation experiments. Construction is under way on all subsystems of the Eight-Beam System (EBS), which is scheduled for completion in early 1977 and will begin target experiments at 10 to 20 TW in 1978. A fourth system, the High-Energy Gas Laser Facility (HEGLF), is in the design and prototype stage. This system will generate laser pulses of 100 to 200 TW.

SINGLE-BEAM SYSTEM (SBS)

Introduction

The Single-Beam System (SBS) is operated both as a service facility for single-beam laser target-interaction experiments at 10.6 μm with a 1.0-ns pulse as well as a developmental system for many aspects of operating and controlling high-energy CO₂ laser systems for target experiments. The SBS consists of a gated oscillator and four electron beam-stabilized amplifiers. The system delivers on target a maximum intensity of 7×10^{14} W/cm² and yields new information for fusion-target design development.

Considerable effort is under way to upgrade the reliability of the Single-Beam System (SBS) so that useful target experiments with 1.5-ns pulses at the 100- to 200-J level can be performed. A major task is to identify those problems of the system that can be eliminated through improved design and components, as distinguished from problems that can be reduced through systematic routine maintenance schedules.

Specific improvements which have so far been implemented are outlined below.

New flashboards were installed in the oscillator to reduce jitter. In the pulse-selection system, the damaged germanium window to the laser-triggered spark gap was replaced, and the system was redesigned to prevent future damage and to switch out the third pulse in the modelocked pulse train.

A major overhaul of the electron beam gun filament structure of the fourth amplifier was completed. The filament wire holders were modified to

prevent the wires from being ejected by the discharge shock wave. Preliminary indications are that the filaments are staying in place during operation of the amplifier; however, the device has not yet been operated at full power.

A beam alignment system for structured targets for the SBS is under construction and should be incorporated into the system by the end of 1976. This alignment system automates three basic alignment functions.

- **Beam Pointing:** A motor-driven mirror-turning system with feedback from a monitor will operate the final turning mirror in front of the target chamber.
- **Target-Positioning Wheel:** A mechanical, detented target wheel with indexing and rotation about the target vertical axis and translation along the beam direction has been constructed (Figs. 1 through 3). The wheel will hold targets at 12 stations, one of which will be a pyroelectric quadrant detector for the alignment monitor. The positioning accuracy of this system is $\sim 5 \mu\text{m}$.
- **Position Sensor:** The quadrant pyroelectric alignment sensor has a $50\text{-}\mu\text{m}$ spacing between elements. This spacing should result in a position resolution of $\sim 20 \mu\text{m}$.

The following target experiments at the 10-J level (using the first three amplifiers) were performed:

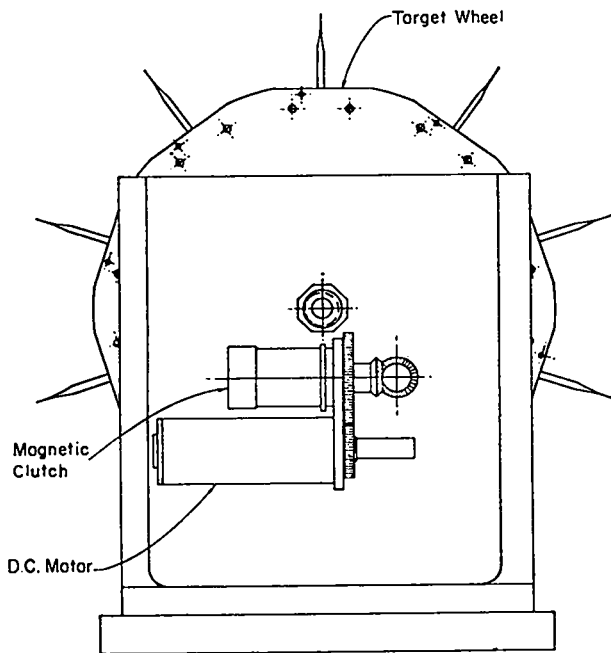


Fig. 1. Mechanically detented target-wheel actuation system.

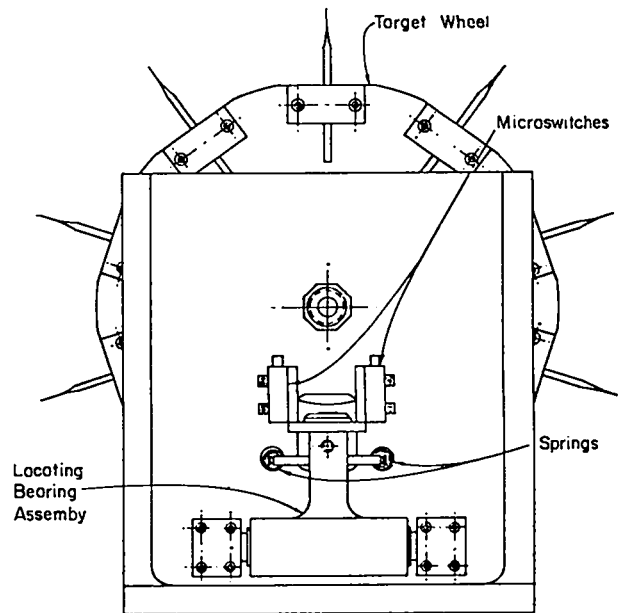


Fig. 2. Mechanically detented target-wheel locating bearing assembly.

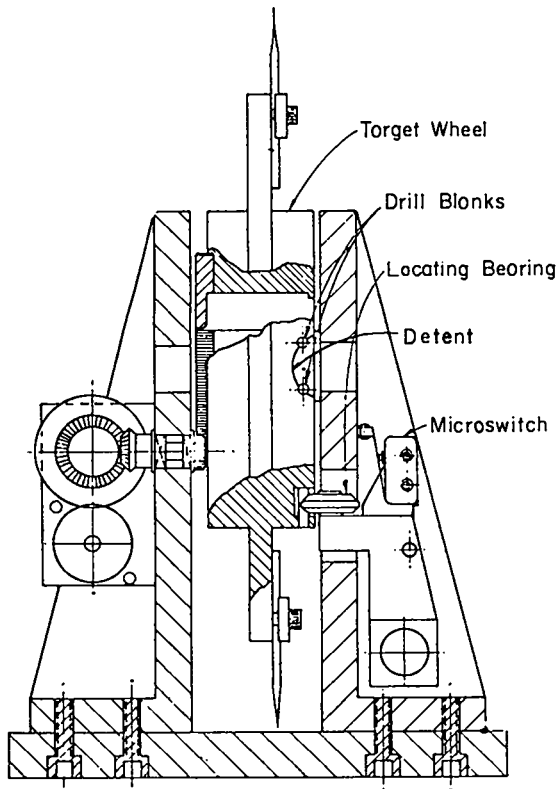


Fig. 3. Mechanically detented target-wheel section view.

- Ion distribution from flat targets.
- Electron current measurements.
- Layered-target x-ray measurements.
- Experiments on classified targets.
- Checkout of 5-GHz oscilloscope to test for noise problems in the target-chamber area.
- Beam profile measurements in the focal plane in the target chamber, using only the oscillator pulse.

TWO-BEAM SYSTEM (TBS)

Introduction

The two major functions of the Two-Beam Laser System (TBS) are to serve as a developmental prototype for the dual-beam modules of the Eight-Beam Laser System (EBS) and to provide a facility for target irradiation experiments for laser fusion research and military applications. All major components of the TBS have been installed.

Our major experimental goal was to determine the effect of a gaseous absorber cell placed be-

tween the triple-pass amplifier and the target chamber. The principal results are:

- SF_6 up to 10 torr-cm is useful in suppressing system oscillation with flat targets.
- The addition of hexafluoroacetone as an R-branch absorber appears to degrade the effectiveness of the SF_6 .
- An unexpected oscillation has been detected in the dual-beam amplifier module at a gain of $\sim 3.0\%/cm$. The newly identified parasitic oscillation requires only the last mirror in the triple-pass optics and may represent a serious limitation in the present design. Further work on this problem will be deferred to the Eight-Beam System so that target experiments may begin on the Two-Beam System in October 1976.

System Development

Our major facilities effort concentrated on repair and cleanup after two major and one minor accidents. In addition, we enlarged the warning-light system to include all means of access to the DBM (dual-beam module) area and installed a low-pressure warning system on the bottled gas supply, which feeds the front end to protect the oscillator and preamplifiers from operations with incorrect or contaminated mixtures.

In preparation for installation of the new optical system for the DBM, the new mirror mounting chambers and supporting structures have been given a trial assembly, leak check, and hydrostatic pressure test.

Dual-Beam Module

Two accidents involving the DBM occurred in July. The first resulted from an arc in the electron gun and a consequent arc in the south pumping chamber. Because electron beam arcing is neither predictable nor preventable with certainty, our response to this accident was to redesign components and modify the machine to limit the extent of damage should future accidents occur. In particular, the electron beam bushing was reinforced to

help withstand the transient overpressure resulting from a foil-window failure. Burst diaphragms were installed on the electron beam chamber to relieve the pressure within <0.5 s.

To limit the damage to the cathode components, the mounting plate was segmented so that individual plate segments could fold back under the force of the intruding gas without applying excessive force to the mounting structure nor hitting the foil supports structure of the opposite foil window.

The second accident occurred when voltage was applied in the main pumping chamber without electron beam ionization. The cable-terminating tank and a high-voltage bushing on the south pumping chamber were damaged mechanically. Subsequently, the cable-terminating tank was replaced with a reinforced design, and an oil-containment shroud and collection tank were installed on both cable-terminating tanks.

Repair, refitting, and checkout were completed, and the DBM was put back into service in late August 1976.

During September, an arc inside the gas-discharge pulser enclosure, which powers the south pumping chamber, cracked a weld. After repairs the DBM was used in experimental measurements of oscillation suppression. Between August 25 and September 21, the DBM was fired 138 times for purposes of experimentation. On 106 shots, the system functioned as expected, but on 28 shots malfunctions prevented the acquisition of useful data. This represents a reliability of 73%, which is quite adequate for our experimental program.

Experimental Program

Our effort has been devoted to studying the utility of various saturable absorber gases for increasing the threshold for self-oscillation of the laser target system. We determined that target experiments would be possible with flat targets at a DBM gain up to $3\%/cm$. The saturable absorber cell at the entrance to the target chamber will not be required, thus eliminating the losses associated with one salt window (7.5%) and with the saturable absorber (20 to 40%). Measurements were performed with the setup shown in Fig. 4. Saturable absorber Cell 1 contains 28 torr cm of SF_6 , which provides a small-signal, single-pass transmission of $<10^{-4}$ in

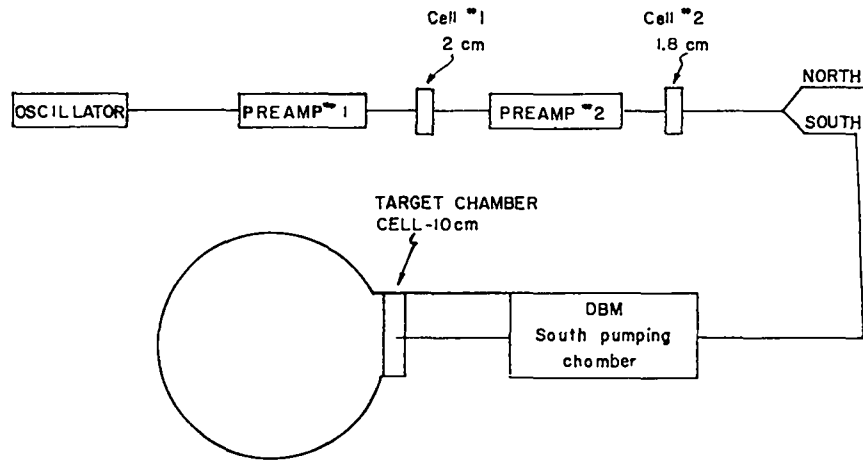


Fig. 4. Schematic of experimental configuration used in oscillation studies.

most of the 10.6- μm P branch. The second cell contains a 232:193:155::FC113:Freon502:CO₂ mixture, which provides an attenuation factor of $\sim 10^3$ in the 9- μm band and of ~ 200 in the R branch of the 10.4- μm band.

EIGHT-BEAM LASER SYSTEM (EBS)

Introduction

The Eight-Beam Laser System (EBS) is the next-generation high-power short-pulse CO₂ laser system we will use to study the interaction of intense light beams with matter, with emphasis on investigating problems relating to laser fusion and military applications. This system is designed to deliver 10 to 20 TW to a target -- 10 kJ in a multifrequency 1-ns pulse, or 5 to 8 kJ in a single-line subnanosecond pulse. The EBS will consist of an oscillator-preamplifier system which generates a subnanosecond multiline optical pulse at the several-hundred-megawatt level, and which will drive four dual-beam amplifier modules (DBMs) clustered around a target chamber. Each of the eight 35-cm-diam beams will deliver ~ 650 to 1250 J (depending on pulse length) to the target chamber, which will contain an optical system to steer and focus these beams onto a target.

Occupancy of the facility is complete; major activities may be summarized as follows.

- DBM Assembly I is complete; DBM II is nearly finished; and the electron gun system for DBM III is ready for testing.
- Small-signal gain measurements are complete on one side of DBM I.
- The electron gun for DBM II has been tested, and DBM II has been used as a high-voltage test facility to resolve some high-voltage breakdown problems.
- Testing of the modified triple-pass optics system has begun.
- The baseline design for the subnanosecond front end is complete, and assembly of a 1-ns, multiline front end is progressing satisfactorily.
- Satisfactory progress continues to be made in the installation of the control systems and in the development of the computer software needed to operate the system.

Power Amplifier Tests

Chamber A of DBM I has been tested at electrical conditions approaching design operating conditions. At 90% of the design-load voltage (290 kV), the pumping-chamber diverter spark gap pre-fired causing the pumping-chamber voltage to ring for many cycles, during which a breakdown occurred near

one of the pumping-chamber high-voltage bushings. Trapped air pockets in certain fiber glass layers of the chamber led to breakdown with attendant arcing and subsequent damage to the chamber. To correct this problem, a spacer will be inserted to move the pumping-chamber cable-termination tank 10 cm away from the chamber, and a field-forming ring will be inserted inside the spacer to reduce the electrical stress along the outside surface of the spacer.

A trial set of parts has been fabricated and installed in Chamber B of DBM II. High-voltage tests so far led to no breakdown at applied voltages of ~275 kV, which is 80% of design point; these tests are continuing. The presence of trapped air pockets in glued or layed-up impregnated fiber glass layers continues to be a source of annoying problems (gas leaks as well as breakdowns) and is related to improper fabrication techniques. Attempts to identify the defective fiber glass flanges by x-ray and ultrasonic tests have failed. We are considering replacing these flanges with solid epoxy castings and the fiber glass chambers with metal ones.

The high-voltage cable used in the EBS has failed on a number of occasions because the semi-conducting sheath around the outside of the virgin polyethylene deteriorates when submerged in oil. The material bubbles and pulls away from the polyethylene, leaving gas pockets which break down when high voltage is applied. The TBS uses apparently identical cables with no difficulty; our investigation, however, revealed that a change in the composition and manufacture of the semiconducting sheath had been made, rendering it incompatible with our application in oil. The change was made without our knowledge. Tests have shown that the cables are useful under normal conditions if the sheath is simply removed, but that the cable does not survive the voltage excursions produced by faulty conditions. Impregnating the sheath so as to prevent its contact with the oil and improved bonding of the sheath to the dielectric (and thus avoiding bubbles) appear to offer solutions to this problem, and are being evaluated.

Master Oscillator and Preamplifier

The oscillator-preamplifier system will produce a subnanosecond multiline pulse with suffi-

cient energy (10 to 100 mJ) to drive the DBM. The subnanosecond master oscillator uses a plasma-smoothing tube to obtain a smooth gain-switched pulse, and an electro-optic switch to chop out a short pulse. The oscillator-preamplifier system and its associated beam-transport optics have been analyzed and designed to incorporate spatial filters and p-doped germanium saturable absorbers.

We made a first attempt at interfacing the preamplifiers and oscillator to the master electronic control and gas-handling systems. The general result was favorable.

Two of the three spatial filters required for the initial single-beam front-end system have been fabricated and have been installed. The entire front-end beam-transport system, with the exception of the cylindrical spatial filter, has been installed.

An extensive series of computer calculations has been completed, which establishes the requirements for the base line design of the front end of the EBS. By varying the input pulse energy to the DBM amplifier from 1 to 100 mJ and varying the input pulse width from 0.25 to 1.0 ns (FWHM), we found, for a multiline input pulse consisting of four lines on the 10- μ m band and for a DBM amplifier small-signal gain of 4%/cm, that the DBM input pulse energy need be only 1 mJ and that the input pulse width should not exceed 0.5 ns to achieve the desired output-pulse characteristics. However, for a small-signal gain of 3%/cm in the triple-pass amplifier, the input pulse energy needed to obtain the desired output pulse characteristics was 10 mJ.

A baseline design for the front end of the EBS is shown in Fig. 5. The oscillator pulse was assumed to have the following characteristics:

- Pulse energy, 1 mJ;
- Temporal width, 0.5 ns (FWHM), Gaussian;
- Spatial width, 2.4 cm (FW at $1/e^2$ intensity), Gaussian;
- Spectral content, four lines on the 10- μ m band [P(12), P(16), P(20), P(24)].

The six preamplifiers shown in the figure have a small-signal gain of 3.9%/cm, a length of 130 cm, and operate at a pressure of 600 torr. The satur-

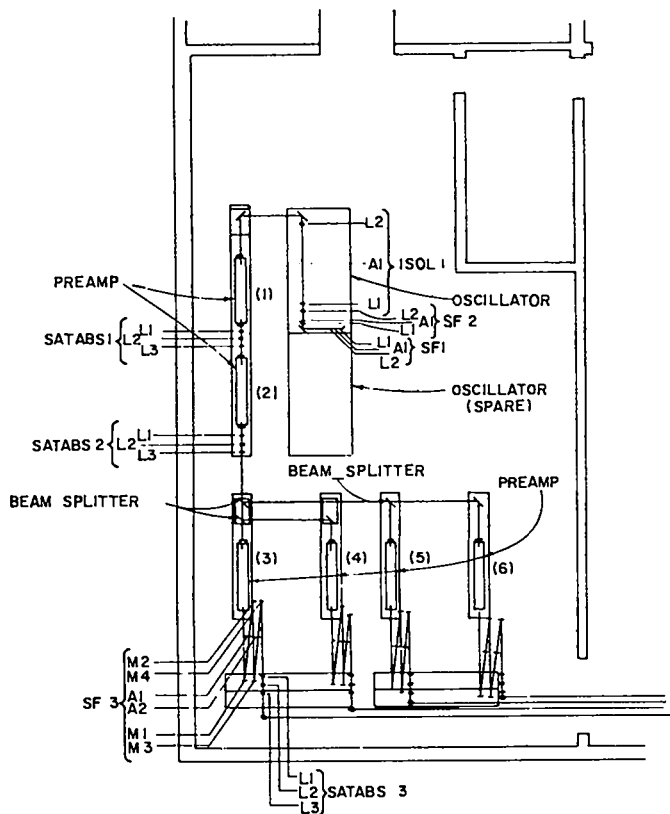


Fig. 5. Front end of oscillator-preamplifier for Eight-Beam System.

able absorbers were assumed to be slabs of p-doped germanium at Brewster's angle with an $\alpha_0 L = 5$, where α_0 is the small-signal absorption coefficient, assumed to be 2.0 cm^{-1} over the spectral band considered, and L is the crystal length, 2.5 cm, through which the beam passes.

Each of the four beams has an energy of 55 mJ with a pulse width of ~ 0.25 ns. Hence, the input pulse energy to each of the triple-pass power amplifiers should be ~ 25 mJ and should be sufficient to drive the triple-pass power amplifiers even at a gain of only 3%/cm in the power amplifiers.

Results for the entire system (front end and triple-pass power amplifier) are given in Table I,

TABLE I
PREDICTED DBM
OUTPUT PULSE CHARACTERISTICS PER BEAM

Gain (%/cm)	Output Energy (J)	Peak Output Power (TW)	Pulsewidth (FWHM) (ns)
4	1000	4.0	0.2
3	450	2.0	0.3

for gains of 4 and 3%/c, in the power amplifiers and for the oscillator pulse characteristics listed above.

Note that these calculations do not take into account coherent effects in the amplification process nor do they accurately take into account multiline saturation effects. Similar calculations, which do take into account these effects, but which differ in some specific geometrical aspects, have been performed using a coherent code. The two different methods agree to within 10 to 20% in most cases so that we feel some confidence in the results here quoted.

DBM Small-Signal Gain Measurements

The small-signal gain of DBM I, Chamber A, has been measured spatially and temporally for the P(20) transition of the $10.4\text{-}\mu\text{m}$ band, using a gas mix of 3:1/4:1::He:N₂:CO₂ at 1200 torr. Figure 6 is a sketch of the equipment layout used in these measurements. A single-pass gain of 3.8%/cm was observed, using the standard gas mix at a pressure of 1100 torr and charge voltages of 240 kV on the

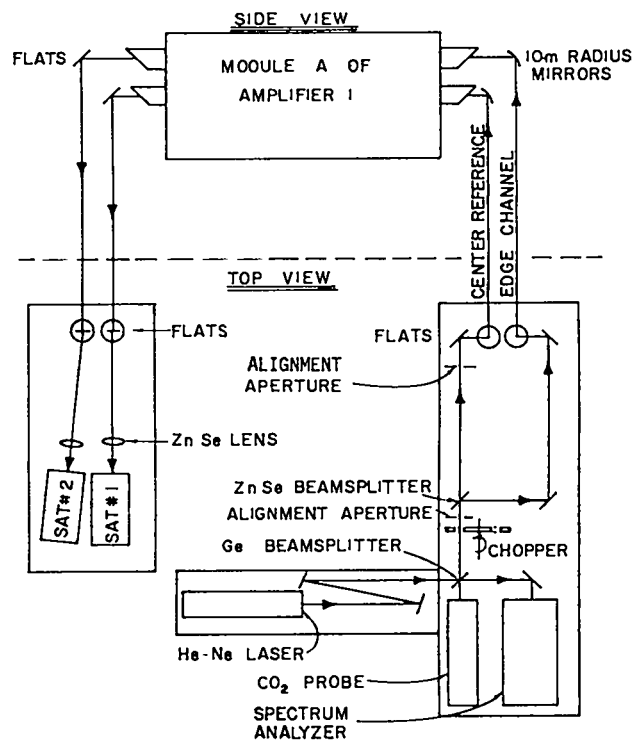


Fig. 6. Layout of experimental apparatus for small-signal gain measurement of Amplifier 1A.

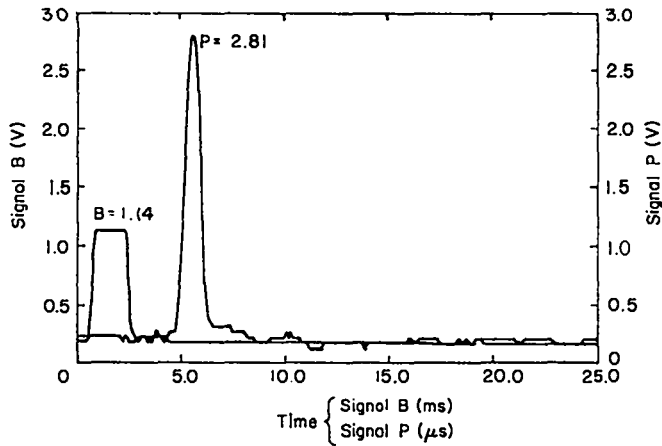


Fig. 7. Computer display of center-channel data from small-signal gain measurement of Amplifier 1A.

electron beam and of 250 kV on the pulse-forming network (PFN). One of the purposes of the gain measurement was to characterize the gain medium, in support of the oscillation stability testing of the modified triple-pass optical system. Because this gain was not high enough for this purpose, we used a helium-free gas mix (0:1:4::He:N₂:CO₂) operated at low pressure to obtain a large ratio of electric field to pressure (E/P) and, hence, a high gain coefficient. At 750 torr, a center-line gain of 4.3%/cm was measured. Gain mapping of the optical aperture was carried out under these conditions.

Figure 7 shows typical center-channel data, as processed by the computer system for the 0:1:4 mix at a voltage of 220 kV on the PFN modified to four-stage operation; Fig. 8 shows the computer-generated diagnostic plots for the electron beam voltage and current, and the gas-discharge voltage and cur-

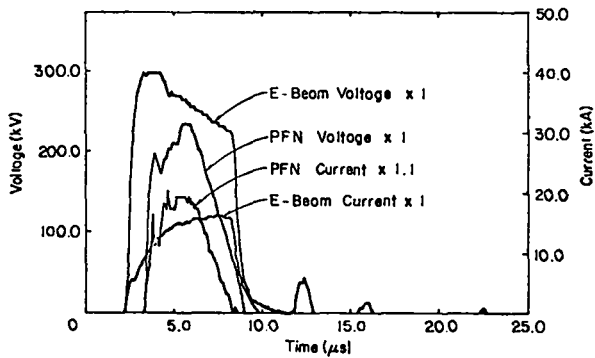


Fig. 8. Computer-generated discharge diagnostics for typical small-signal gain-measurement shot.

rent for a typical small-signal gain measurement; and Fig. 9 shows the spatial distribution of gain over the optical aperture. The results have been normalized to the gain along the center channel (where the actual gain coefficient was 4.3%/cm). The gain variation is very similar to that observed in the prototype module in the TBS and is thought to be produced by the divergence of the electron beam from the gun and by the subsequent increase in the electric field in the regions of reduced ionization near the anode.

Because of the necessity of proceeding with stability measurements on the modified triple-pass system, the gain measurement at Locations B1 and C1 were not made. Based on the gain measurements at the symmetric locations (B3 and C3) and on the spatial distribution data from the TBS, Locations B1 and C1 should not show abnormally large gain coefficients and thus should not cause uncertainty in the interpretation of the triple-pass measurements. In summary, 97 electron beam shots and 115 full system shots were fired to obtain 23 data points.

Installation of the triple-pass system components is complete, and testing of that system commenced at the end of September 1976.

Control Systems Hardware

Installation of the controls system hardware continues satisfactorily, and recent accomplish-

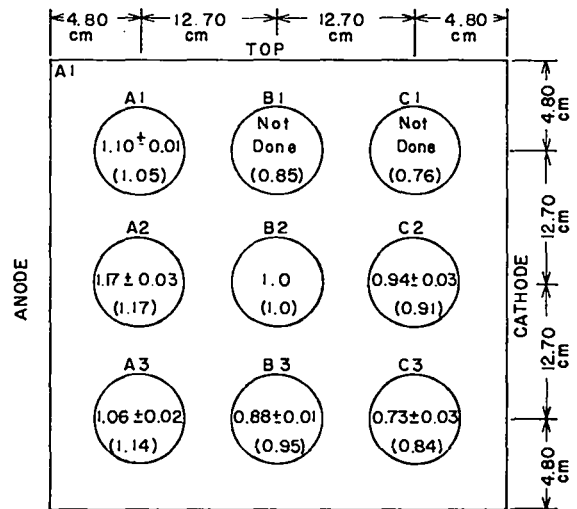


Fig. 9. Distribution of small-signal gain in Amplifier 1A, normalized to center-channel gain. Values in parentheses are corresponding values measured in Two-Beam System.

ments may be summarized as follows.

- The sensors and the wiring for the DBM amplifier gas-fill system are complete and have been checked out as far as the computer.
- The vacuum control systems are operational for three of the four DBMs.
- Control and status-signal cables between the control room and the front-end system are installed.
- All nine (eight plus a spare) 40.5-cm (16-in.) mirror mounts for the triple-pass system have been assembled; several have had the motor drives inserted and wired.
- The mirror motor control system is nearly complete. A portable control unit is available for use with the 38-cm (15-in.) mirror used in the triple-pass test now in progress.
- The spark-gap gas systems for the PFN and the electron gun pulsed power supply are complete. The gas-gap system for the existing front-end lasers is also complete and operational.

Safety System for EBS Building

A microprocessor-based safety interlock system that will monitor the room interlocks, display the safety status of the EBS, and enable the firing of high-voltage pulsers has been built. This design will also serve as a test of the microprocessor in a severe electromagnetic pulse environment. The system consists of a M-6800 microprocessor (installed at a control panel for operator input and display of optical and CAMAC interfaces) and various building interlocks. The single-task program, directed by the panel switches, will check all building interlocks, inhibit system operation under unsafe conditions, display the safety status, test itself, and provide a fail-safe output.

Computer-Controlled Monitoring, Diagnostic, and Control System

For full-system operation of the EBS, all the various subsystem controls are tied to, and con-

trolled by, a Data General computer system. Computer operation also offers the ability to monitor and diagnose the operation of the laser system and of its related components.

The computer system, consisting of a Data General S-200 Eclipse central processor, a disk system, a tape unit, a CAMAC interface and several CAMAC crates, of Tektronix 4010 and 4014 graphics interface terminals, and of a Versatek printer, is complete and operational. We have acquired FORTRAN V and FORTRAN IV (with hardware arithmetic) and the latest revision of the RDOS Operating System; the new operating system is in routine use. A more powerful plotting system has also been acquired from Tektronix and is operational. Most of the effort is devoted to writing the programs needed to operate the controls hardware.

Mechanical Assembly

Mechanical assembly is progressing ahead of schedule and is devoted to integration of the four DBMs and to repairs brought about by high-voltage breakdown.

- DBM I: The pumping chambers are being strengthened by placing a thick layer of epoxy around the high-voltage feedthrough flanges. A new mount has been installed for the protective diverter gap so as to place it closer to the high-voltage bus and render its operation more reliable. The modified triple-pass system has been installed on one side.
- DBM II: The electron gun has been tested successfully. As indicated earlier, the use of DBM II as a high-voltage test facility indicated that the high-voltage modifications were successful at ~80% of design-point operation. The test was interrupted by a breakdown due to a defective fiber glass flange.
- DBM III: The electron gun is ready for testing.

HIGH-ENERGY GAS LASER FACILITY (HEGLF)

Introduction

The objective of the High-Energy Gas Laser Facility Program (HEGLF) is to extend the present CO₂ laser capabilities to power levels at which fusion experiments can be expected to yield thermonuclear energy release in the range of scientific breakeven (defined as equality between the thermonuclear energy output and the laser-beam energy incident on target). The investigation of laser fusion phenomena at these levels will provide more complete understanding of the physics involved and allow laser and target design parameter requirements to be established with confidence. The program specifically calls for the construction of a six-beam, 100- to 200-TW CO₂ laser (100 kJ in 1 ns or 50 kJ in 0.25 ns) and of an associated target-irradiation facility.

We have undertaken a prototype program to verify experimentally the analytical conclusions and to confirm from an engineering standpoint the design concepts before beginning procurement of the major laser hardware.

Significant progress was recorded in three areas. First, experimental studies by Systems, Science and Software, San Francisco Division, demonstrated the viability of current control in cold-cathode electron guns by a self-biasing grid. Second, additional modeling of the power supplies for the gas discharge in the power-amplifier modules showed the advantages of single-section Guillemin networks. And third, Title I drawings and specifications prepared by the Architect Engineer (Norman Engineering Co.) were accepted by ERDA.

Prototype Programs

Gridded Cold-Cathode Gun -- Ionization of the laser gas in the HEGLF power amplifier modules will be controlled by electrons from a cylindrical gridded cold-cathode gun. The grid is an 80% transparent electrode interposed between the cathode and the anode, in which the grid potential is self-imposed by returning the grid current to ground through a resistor. This arrangement allows adjustment of the gun current and, because of the self-biasing arrangement for grid potential, should greatly reduce the time variation in current nor-

mally experienced in cold-cathode guns. To verify the concept, Systems, Science and Software built and tested a 200-cm-long gun with an anode diameter of 135 cm. For this geometry, space-charge-limited theory predicts, for cases of interest,

$$I \approx \frac{V}{R\alpha}, \quad (1)$$

where I is the gun current in amperes; R the grid resistance; V the gun voltage; and α is the fraction of gun current flowing to the grid. The unit built by Systems, Science and Software has an α of 0.2. Test results show that the observed gun current is about half to two-thirds that predicted in Eq. (1). The difference is probably due to the cathode consisting of 12 line sources equally spaced around the cathode circumference as opposed to a continuous cathode as postulated in the theory. Tests indicate the uniformity of current density at the anode is about $\pm 15\%$ when the gun is operated at the highest test voltage (450 kV). Magnetic effects are seen at the higher gun currents, but these effects have not yet been determined quantitatively.

Prototype Power Amplifier Module -- We have devoted much effort to the detailed design of major parts of the amplifier module as well as to the power supplies to operate the unit. Modifications to the laboratory and buildup of controls and auxiliary systems to operate and test the module also received considerable attention. All larger amplifier components have been designed and are in the procurement cycle. Design of handling equipment and smaller parts is estimated at 75% complete.

High-Voltage Test Module -- A test module was designed for the purpose of obtaining electrical breakdown data on ionized CO₂-N₂ laser gas and surface flashover data for electrical feedthrough bushings in the same medium. The module can be considered a full-scale setup in terms of all critical dimensions to be encountered in the HEGLF power amplifiers. A cold-cathode electron-beam gun provides the same ionization level and distribution as the real machine. The electron beam is controlled by a grid to obtain the required laser beam density and to gain more experience with a grid-

TABLE II

DESIGN DATA OF TEST MODULE

Pumping Chamber:

Peak voltage	= 750 kV
Peak current density	$\approx 12 \text{ A/cm}^2$
Peak current	$\approx 6 \text{ kA}$
Maximum pulse length	$\approx 2 \mu\text{s}$
Energy deposited	$\approx 10 \text{ kJ}$
Gas pressure	= 2.5 atm

Electron Beam Gun:

Peak voltage	= 750 kV
Peak current density	$\approx 100 \text{ mA/cm}^2$
Peak current	$\approx 50 \text{ A}$
Maximum pulse length	$\approx 2.5 \mu\text{s}$
Energy in beam	$\approx 100 \text{ J}$
Gun chamber pressure	= 10^{-5} T

controlled cold-cathode gun. All components and subassemblies for this experiment have been designed, fabricated, and tested; experimental work will begin in October 1976. Pertinent data are summarized in Table II.

A schematic of this test module is shown in Fig. 10, and a schematic of the electrical circuit is shown in Fig. 11.

HEGLF Laser Design

Parameter Studies -- To verify the adequacy of the double-pass power amplifier module design, we modeled the pulse performance by using both a code based on the Frantz-Nodvik rate-equation method, and a coherent pulse-propagation code. Five-line, single-band operation was assumed. With the amplifier filled to a pressure of 1800 torr, a single-pass gain-length product of 9 was more than adequate to provide desired output pulses, given easily achieved input pulses. Good agreement between the two methods was obtained. Figure 12 shows the input-output behavior calculated for a range of pulse heights and widths for a single amplifier sector (1/12th of a module or 1/72nd of the entire system). Superimposed on the plot are points representing the HEGLF design criteria.

Power Amplifier Module Electrical Design -- We have conducted tradeoff studies with the aim of optimizing the electrical design of the power-amplifier module around the amplifier requirements. One of the requirements is the beam geometry; others are the pumping energy and electron beam needs of the amplifier. Important design criteria and limitations are reliability, simplicity of electrical circuit, and minimization of total cost.

The pumping requirements have been calculated for the required electric field of 18 kV/cm, a

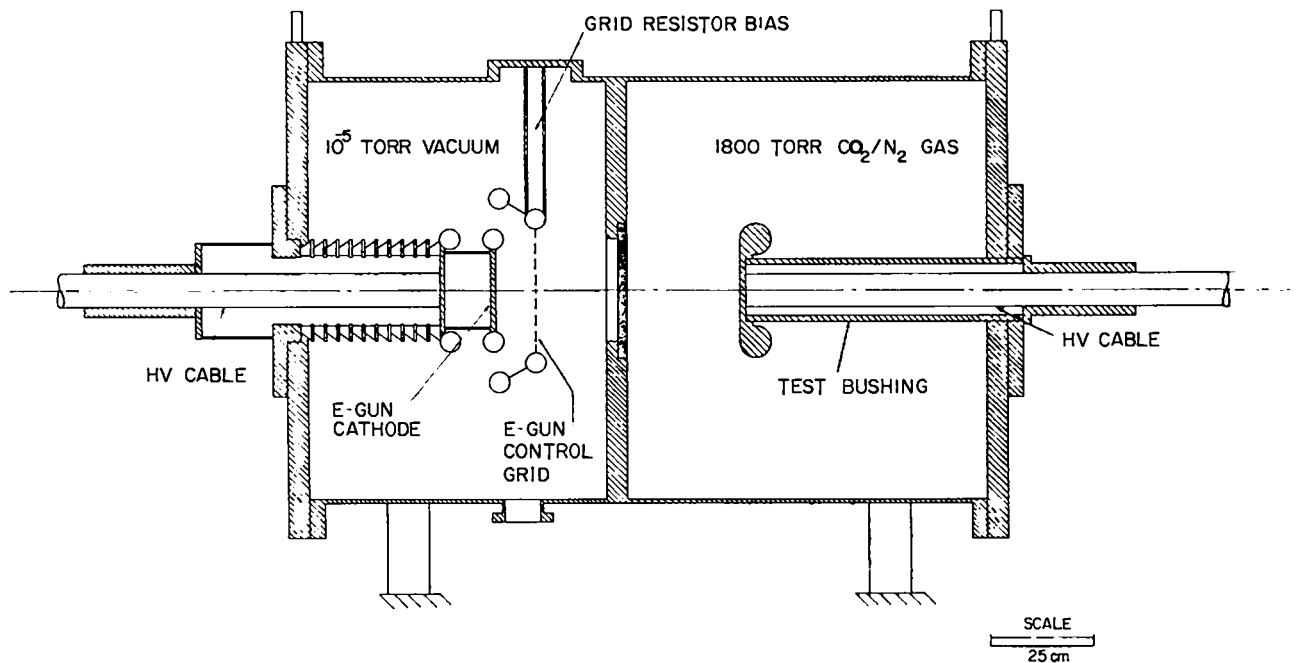


Fig. 10. Schematic of test module.

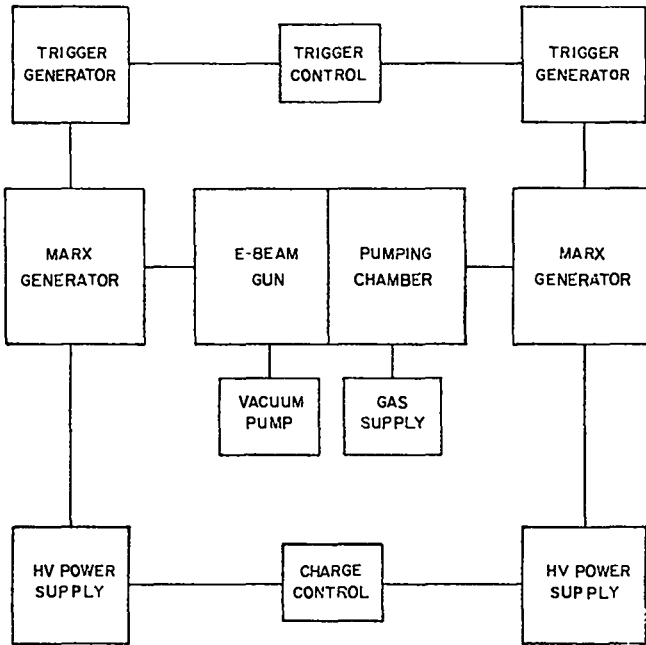


Fig. 11. Electrical circuit of test module.

laser gas pressure of 1800 torr, and a gain-length product of 9, as a function of time and current density for a square power input pulse.

Table III shows the laser parameters as a function of current density, where the pumping pulse is terminated as soon as 90% of peak gain is reached. By terminating the pumping pulse at gains

smaller than the possible peak gain, the efficiency is considerably increased.

Two designs for the energy storage units have been studied: a two-mesh and a one-mesh PFN (Type-C Guillemin). The two-mesh network produces a reasonably square waveform if the loop inductance associated with a 1-MV Marx generator does not become large compared to the mesh inductances. However, for the required short pumping pulses (1.0 to 1.5 μ s), this is exactly the case. Consequently, the one-mesh network (matched RLC circuit) produces equally good waveforms (Fig. 13).

The incentives for using the one-mesh network are great because it results in simpler circuitry, allows for a higher inductance and consequently fewer energy storage units, and permits the use of more readily available components. The only disadvantage is the need for somewhat more stored energy.

We built a model to better visualize the routing of the high-voltage cables from the energy-storage units to the power amplifiers (Fig. 14).

Mechanical Design -- Finite-element analyses of prospective mirror designs have continued and resulted in the selection of two designs, one in aluminum and one in beryllium copper, for the manufacture of two 71-cm (28-in.)-diam prototype mirrors.

We completed the structural analysis for a single design of a target-area turning-mirror sup-

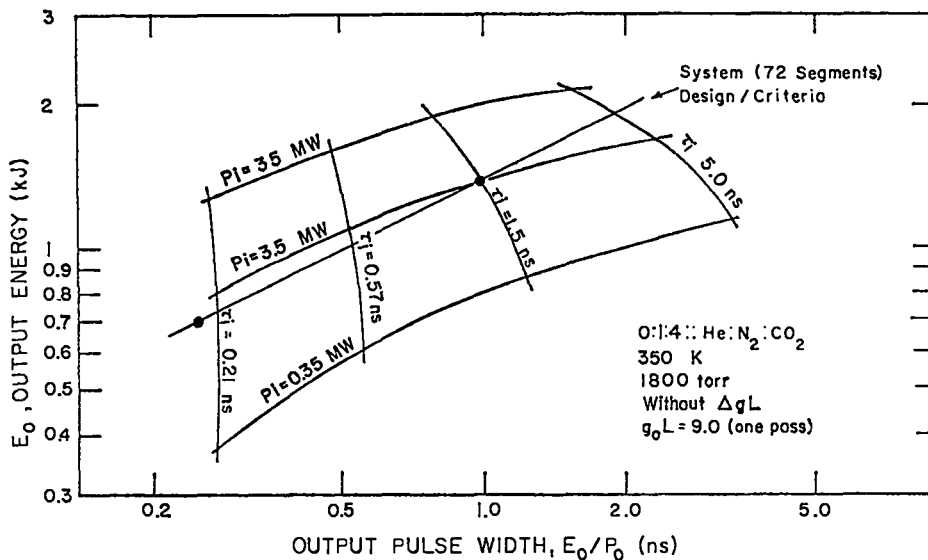


Fig. 12. Calculated single-segment input-output characteristics for HEGLF double-pass power amplifier module.

TABLE III

LASER PARAMETERS AS FUNCTION OF CURRENT DENSITY
 AT 18 kV/cm and 1800 torr,
 AND WITH A 1:4::N₂:CO₂ MIXTURE

J (A/cm ²)	g (m ⁻¹)	T (μs)	l (m)	I (kA)	W (MJ)
10	3.31	1.05	2.72	68	2.6
9	3.13	1.12	2.87	65	2.6
8	2.94	1.22	3.06	61	2.7
7	2.72	1.25	3.31	58	2.6

where:

J = peak current density,

g = 90% of maximum gain attainable with the given current density,

T = square-pulse length,

l = the length to give $gl = 9$,

I = current per beam, and

W = the total energy delivered to 72 beams at constant current.

port structure. The design was adequate; its natural frequency was satisfactorily high with respect to the expected environmental frequencies.

Target Subsystem -- The vibrational analysis of a space frame for the target focusing system was initiated. It was performed on a design concept for an aplanatic pair/turning-mirror system. Emphasis has now been directed toward a turning-mirror/on-axis parabola focusing system with the result that a different and slightly smaller space-frame design will be developed.

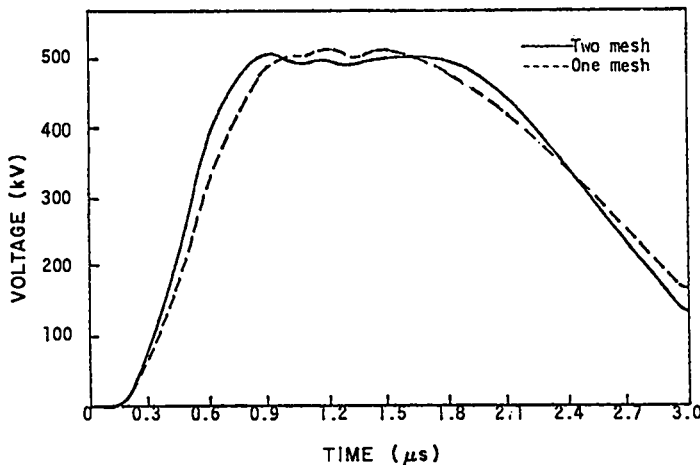


Fig. 13. Gullemin network waveforms.

Instrumentation and Controls

Microprocessor Development -- We have begun the conceptual design of a stepping-motor controller system for HEGLF. The concept provides control of multiple stepping motors from a standard asynchronous communications interface of a digital computer. The stepping-motor commands are transmitted serially over fiber optics to each stepping-motor controller. Each controller contains the fiber-optics interface, a microprocessor, and the stepping-motor drive circuits for three motors. Multiple controllers are connected in a daisy-chain configuration, which allows many motors to be controlled from one asynchronous communication channel.

Fiber Optics -- A fiber-optic data-link transceiver for HEGLF data communications links has been designed, built, and tested. This circuit, arranged as an optical repeater station, will allow tapping into a fiber-optic bundle and transmitting into, or receiving, the serial data stream; thus the circuit will have the capability of a multi-

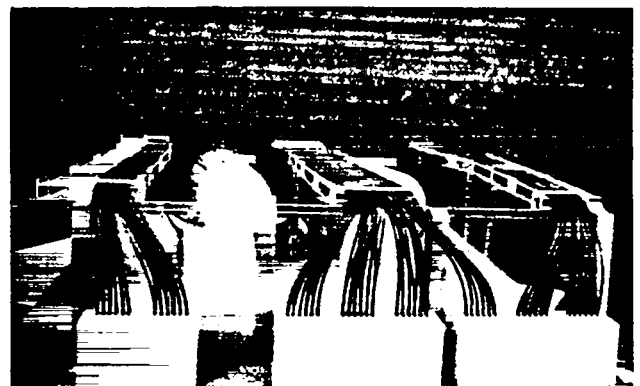
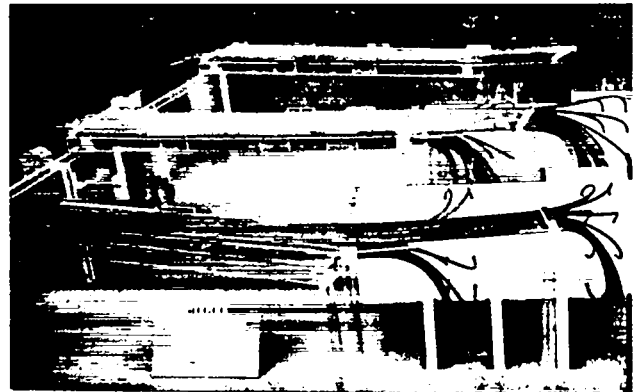


Fig. 14. Model showing routing of high-voltage cables from energy storage units to HEGLF power amplifiers.

terminal optical data bus. When used as an optical repeater, the circuit has an optical power gain of 2×10^4 , enough to drive a 50-m link at a bandwidth of 4 MHz. For optical connections, the transceiver uses the AMP, Inc., fiber-optic bundle connectors and Gallite 1000 or 2000 fiber-optic cable.

HEGLF Facility

The Title I drawings, specifications, and estimates were submitted by Norman Engineering (NECO) for LASL and ERDA review. These preliminary drawings and specifications for the most part comply with the design criteria, although many comments and minor changes are forthcoming.

The vacuum system, which is a part of the NECO package, is being considered for a negotiated fixed-price contract that is separate from the building construction contracts.

A rough draft Preliminary Safety Analysis Report and a preliminary proposal were submitted for review.

Optical Engineering

The Y-12 Diamond-Turning Facility -- The quantity and configuration for large HEGLF optical components leave diamond turning as the only cost- and time-effective method of fabrication. The Y-12 Plant of the Union Carbide Corp. in Oak Ridge, TN, has a diamond-turning development program dedicated to the production of mirrors. In FY 77 we are supporting a continuation of the diamond-turning development project, which includes programs in:

- optical finish and figure improvements;
- optical inspection and interferometry;
- substrate development;
- part fixturing and mounting; and
- electroplating.

The University of Arizona and the University of Tennessee support the Y-12 program in the areas of optical engineering and structural analysis, respectively.

We are also funding a facilities modification at Y-12. The modification will provide a clean, quiet environment to house the diamond-turning

facilities. Three Excello machines and two Moore machines will be located in the facility. The quiet environment is required to fully realize the ultimate potential of the machines.

Optical Evaluation Facility -- An optical evaluation facility will be constructed to accommodate all components, including the 200-cm-diam mirrors for HEGLF. An optical path length of 55 m (180 ft) on two seismic blocks is possible with one folding mirror. A maintenance area is included. The design criteria are now in preparation.

NaCl Windows -- NaCl has been chosen as the window material for the HEGLF. However, production facilities for the size and number of windows required are limited. To meet the completion dates for the program, additional production capacity is needed. Potential suppliers have been surveyed, and requests for proposals have been sent to those with the necessary technical base. We have retained the option to select one or two suppliers.

Samples of polycrystalline NaCl have been successfully diamond-point machined at Y-12. After machining, a minimum of conventional polishing may be required to finish the surface. This approach to finishing halides is confirmed by recent test results on KCl obtained at the Naval Weapons Center. Diamond turning promises to be a relatively simple method to optically finish difficult materials such as the halides.

The Naval Weapons Center and Optical Coatings Laboratory, Inc., have completed programs that included studies in the surface finishing and anti-reflection coatings of halides. Relevant results include these findings:

- Single-layer antireflection coatings of materials such as NaF and SrF_2 appear immediately applicable to short-pulse CO_2 laser systems, as suggested by damage tests with nanosecond pulses.
- Coating uniformity over sizes approximating those of windows used in the HEGLF appears adequate.
- Work should continue to improve the quality of thin coatings and to minimize defects on large components.

Optical Analysis Codes -- We have added to the LASL geometrical optics code FRESNEL options for sevenfold aspheric surfaces, internal checks on ray tracing, and an optimization subroutine. Test problems have been run. The optimization routine proceeds reliably and converges rapidly. The upgraded code is now known as MAXWELL and includes an option to give rms wavefront errors at the focus.

ACCOS V, a commercial code, has been purchased and installed. A basic language computer program has been written for the HP-9830 computer to allow general conic-toric mirror elements to be expressed in terms suitable for use with ACCOS V. The base line ring-focus power-amplifier system was modeled on ACCOS V. Preliminary results indicate excellent agreement with results from FRESNEL calculations.

Error budget calculations have been initiated for the base line HEGLF design. The budget will be prepared in terms of both rms wavefront error and wavefront variance.

CO₂ LASER TECHNOLOGY

Introduction

Each of our CO₂ laser systems described earlier represents a significant advance in the state of the art of reliable CO₂ laser subsystems, components, and diagnostics. The design, construction, and improvement of the systems require, therefore, basic support of CO₂ laser technology. Some important areas are: the development of short-pulse multifrequency oscillators, amplifier optimization, development of optical subsystems, development of subsystems for the prevention of system self-oscillation and removal of prepulse energy, improvement of the transverse profile of the amplified laser pulses, and basic measurements, e.g., of the optical damage thresholds in system components.

Oscillator Development

General -- Future laser fusion target-interaction experiments at 10.6 μm will require subnanosecond pulses. We are therefore actively pursuing the design, testing, and construction of a subnanosecond oscillator system capable of operating on multiple vibrational-rotational frequencies of the CO₂ molecule. This short-pulse requirement has led

to the development of new methods of short-pulse generation in gas lasers and of techniques for obtaining multifrequency performance from CO₂ laser systems. Results have been most encouraging; we are now able to generate temporally smooth pulses containing a single rotational line or containing several rotational lines in one or both bands of the CO₂ laser. This multifrequency capability is essential for efficient energy extraction by subnanosecond pulses in 1800- to 2000-torr CO₂ amplifiers.

We have modified a multiline, temporally smoothed oscillator to produce high peak power, and will employ it as the basic oscillator for subnanosecond pulse generation. Modifications to the TEA subsystem in our oscillator laboratory permitted operation with any mixture of CO₂, N₂, and He. The statistical fluctuation of the oscillator output spectrum was characterized. Our electro-optical switch which generates a subnanosecond pulse from the above oscillator is described, and data taken with a 5-GHz detection system are presented.

High-Power Multiline Oscillator Development --

The multiline CO₂ oscillator described in the previous progress report (LA-6510-PR) has been modified for high peak power operation. The resulting source, used in conjunction with a fast electro-optic switch discussed below, will be the basic oscillator for the subnanosecond pulse system. This oscillator system will generate a 40-MW, 40-ns FWHM optical pulse consisting of four to five rotational lines in the P branch of the 10- μm band.

By precisely positioning the electrodes, electrical operation was made independent of laser gas mixture. In particular, a helium-free mixture consisting of equal parts CO₂ and N₂ permitted an increase of electrical energy deposition to 440 J/liter, and improved gain risetime characteristics. Peak P(20) gain was 0.021 cm^{-1} , occurring 0.49 μs after discharge initiation. These improved characteristics were matched by installing an optimum output coupling mirror (65% transmission), giving a 40-MW peak power, smoothed, multiline output pulse of 50-ns FWHM duration.

In a parametric study of the oscillator output spectrum, we tried to characterize the content and statistical variation of the multiline performance. In this test, a small, commercial spectrometer was

coupled to an infrared vidicon camera, video disk recorder, and television monitor to permit quantitative scans of the 10- μm band P-branch oscillator output on each shot. A typical scan is reproduced in Fig. 15.

In this figure, five adjacent rotational lines [P(14) through P(22)] are shown to have been present in a single oscillator pulse. A study of data from 50 shots showed that at least four of these lines were always present, with a maximum line-to-line intensity ratio of 10 and a mean ratio of 5. This result is well within the limiting line-to-line ratio of 20 indicated by computer studies of multiline pulse propagation in the EBS.

Full-Wave Electro-Optic Shutter -- With the oscillator described above as our input source, a subnanosecond pulse is generated by using a fast electro-optic shutter driven by a laser-triggered spark gap (LTSG) to gate a pulse of the desired duration and shape from the 50-ns envelope produced by the multiline oscillator.

Previous progress reports have described in detail the oscillator for the 0.25-ns system. Recent calculations have shown that pulses between 0.25 and 0.5 ns (FWHM) with equal risetimes from the oscillator will give the same output pulse shape from an amplifier system. This allows us to simplify the design of the fast Pockels cell. A 50- Ω LTSG is used to generate the high-voltage (hv) pulse. The hv output cable is mounted at the end of the CdTe switchout crystal, allowing the half-

wave hv pulse to propagate down the length of the crystal with the CO₂ laser pulse. Reflection of the hv pulse from the other end of the crystal results in an asymmetric multiline pulse with 190-ps risetime and 400-ps duration (FWHM), as shown in Fig. 16. Voltage reflectance and dispersion at the hv cable to the crystal interface are shown in the time-domain reflectometer/sampler data in Fig. 17. From these data, we conclude that the characteristic impedance of the crystal in the longitudinal direction is $\sim 60 \Omega$ and that the ringing after the pulse is $< 5\%$, as shown in Fig. 16.

Spatial Filters

Mechanical design and construction of one spatial filter unit was completed by E.G.&G. (Los Alamos). This unit was tested and installed in the Gigawatt Test Facility (GWTF). The unit operated as planned; however, our estimates of the optical flux limits imposed by optical damage to the focal-plane iris had been quite conservative, considering the minimal amount of beam cleanup required in this application. With a reasonably clean Gaussian input beam, peak focal-plane intensities as high as 600 GW/cm² could be endured without unacceptable long-term iris damage. This value is 20 times higher than the design optical flux limit for nanosecond pulses.

The limiting iris in our design was chosen to be four times larger than the focal-plane beam waist (defined as the 1/e² intensity point) for an

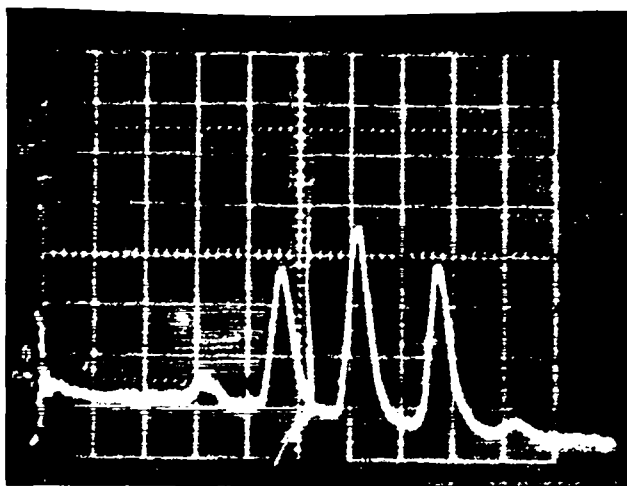


Fig. 15. Line scan from Ir vidicon display on TV monitor; P(14), P(16), P(18), P(20); 10 μm .

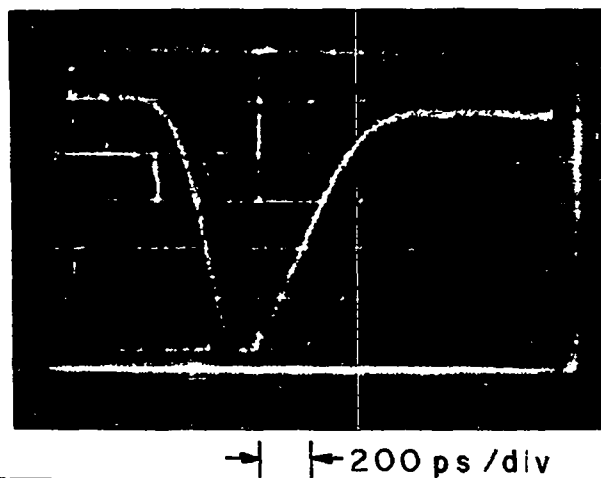


Fig. 16. Full-wave electro-optical pulse.

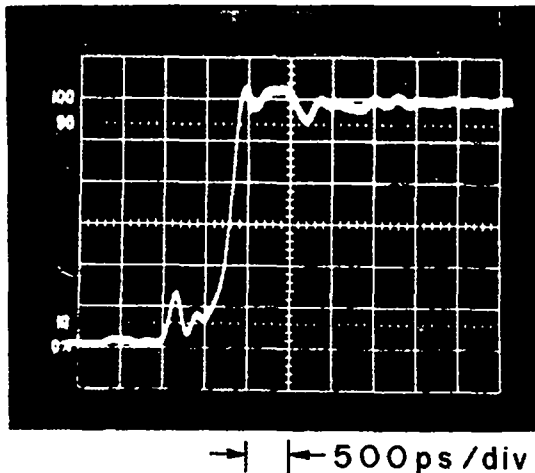


Fig. 17. TDR/Sampler reflected pulse from end-mounted CdTe crystal.

input Gaussian distribution of the assumed diameter. This iris should, then, intercept no more than 2.7×10^{-9} of the peak intensity of an ideal Gaussian distribution, perfectly aligned through the filter unit, or $\sim 2 \text{ kW/cm}^2$ in our case.

In each experimental situation, the permissible spatial filter input intensity will depend on input beam quality and on alignment uncertainty (a 600-GW/cm^2 intensity level produced unacceptable cratering and spallation of the iris when the beam was deliberately misaligned). About five such damage sites were sufficient to ruin the iris surface, producing a surface with a high scattering coefficient that significantly lowered the self-oscillation threshold of the amplifier system.

In practice, it was relatively easy to pre-align the spatial filter to produce no more than $250 \mu\text{rad}$ of beam deviation upon insertion. A pressure of less than 0.5 torr was sufficient for proper operation of the filter at the highest intensities used.

Optical Subsystems

General -- Work in the design and analysis of optical subsystems is of increasing importance in our CO_2 laser systems. The length of the system and the large number of reflecting and transmitting optics in our larger systems, along with strict requirements on the accuracy of aiming and focusing

the pulses onto targets, require careful system design for alignment and optical stability.

After stability measurements of the floor and optical stands, we conclude that the system should remain in alignment for at least many hours and probably days without readjustment. However, the mirror and mounts are expected to be much less stable.

Two approaches are being considered for automatic alignment of the EBS:

- Remove the three p-type germanium saturable absorbers; if this can be done without deflecting the beam path significantly, alignment will be performed with a cw or long-pulsed CO_2 laser in the same cavity as the short-pulse oscillator.
- Use the nanosecond oscillator and some preamplifiers.

Because of the need for frequent alignment after only a few shots, we need detectors which can sense the magnitude of the misalignment and permit the computer to calculate the degree of mirror motion needed to correct the error. These detectors are now being designed.

A system to detect and measure misaligned energy deflected by spatial filters is being designed and experimentally simulated with an He:Ne mockup.

Target Alignment in Two-Beam System-- Hartman-mask pyroelectric vidicon systems have been proven feasible and have been purchased and modified; permanent installation is expected in mid-October 1976.

Optical Modifications of Single-Beam System -- As the prototype laser, many modifications have been made to the optical system of the SBS. We now plan to simplify both the optical and the alignment system. The new systems will increase stability, shorten alignment time, and, in general, improve laser performance. To avoid a cessation of target experiments, the new system will be installed piecemeal, about a week at a time, during pauses in the target program.

EBS Target Chamber and Optical Support Structure -- The optical-error budget and sensitivity

analysis should be completed in October 1976. Preliminary designs of the target-chamber optical support structure and vacuum vessel have been prepared. A review of the final engineering drawings will be held with the vendor in October to freeze the design and to start the construction after contract negotiations are completed.

CO₂ Laser Imaging System -- We plan to improve the alignment accuracy of high-power CO₂ laser beams, using a microscope and television system that works with 10.6- μ m light. A similar system performed very well on our glass laser system at 1.06 μ m. A photograph made with a germanium lens and a pyroelectric vidicon camera was included in the last progress report. It indicates that such a system can have adequate resolution for accurate alignment of CO₂ beams on laser fusion targets.

Rapid development and improvement of pyroelectric vidicon tubes continues. We purchased some new state-of-the-art tubes and ordered a custom-built camera for operation with these tubes. The camera will have a signal-compression capability that will vastly improve its dynamic range. The manufacturer has encountered some difficulties in the development of the camera, but we expect delivery soon and will evaluate its performance.

Isolator Development

Introduction -- We examined three methods of protecting large oscillator-amplifier systems from the damaging effects of amplified target reflections. We found that both optically and electrically triggered plasma breakdowns in a gaseous laser medium, and self-induced plasma breakdown in

spatial filters, can substantially attenuate high-power CO₂ laser pulses.

Work also continued on the use of narrow-band resonant absorbers to prevent system self-oscillation and to help to remove prepulses in CO₂ laser systems. The results demonstrated that our modeling of hot CO₂ absorbers is in agreement with our experimental observations.

Optically Driven Plasma Absorbers -- The use of self-induced optical breakdown in gases seems an attractive method of protecting laser and amplifier components from damage arising from target retro-reflections. Basically, the idea is to find a point, or points, in the amplifier where the generated pulse can pass through a focus with little or no attenuation while the more intense repulse causes gas breakdown, leading to substantial energy loss through plasma absorption and refraction. To ascertain the effectiveness of this approach, we have measured the transmission of a nanosecond, 10.6- μ m pulse through a focus in CO₂.

The experimental apparatus is shown schematically in Fig. 18: A 10.6- μ m, 1.0-ns pulse produced by the SBS was used for the transmission experiment. The useful beam energy ranged from 30 mJ to 5.0 J in an ~5-cm-diam beam, corresponding to an energy density ranging from 1.5 to 255 mJ/cm². This energy density was increased by a factor of ~2000 with the mirror arrangement in Fig. 18. By reducing the input beam size (d) to this mirror system from 5.0 to 3.65 cm, the peak focal-plane intensity could be varied from 1200 to 480 J/cm². Reduced values were obtained with attenuating filters. At these high-energy shots the visual break-

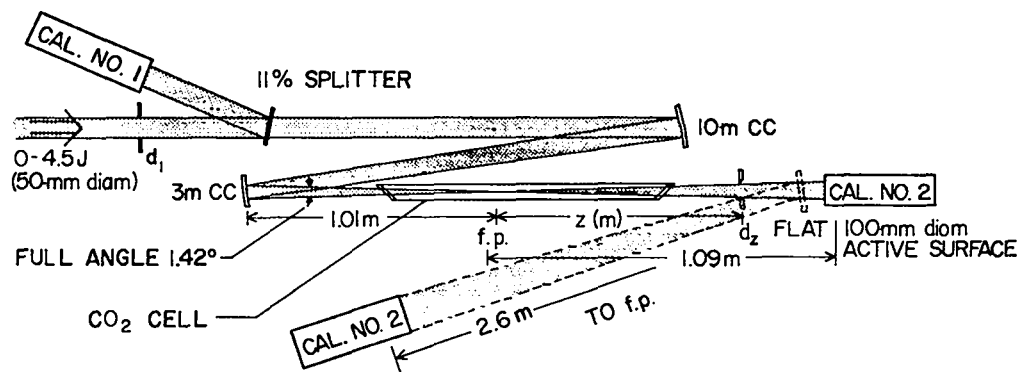


Fig. 18. Schematic of plasma absorption experiment.

down occurred along the tube axis 20 cm before the focal point. Because of this distributed spark channel, it is not meaningful to discuss the data in terms of energy density except for the threshold effects.

Typical data are plotted in Figs. 19 and 20 for various values of d and distances of Calorimeter 2 from the focal point. We see that at low incident energies ($E_{inc} \leq 0.10$ J for P_1 , Fig. 19, corresponding to ~ 11 J/cm² and $E_{inc} \leq 0.04$ J for P_2 , Fig. 20, corresponding to ~ 4 J/cm²), the pulse passes through the gas cell with virtually no attenuation. At incident energies above 1.0 and 0.7 J, minimum transmissions of 20 and 15% are obtained for P_1 and P_2 , respectively. As expected, the gas at higher pressure is broken down more readily and is a slightly more significant attenuator.

The data also provide some information about the amount of refraction of the light transmitted through the focus. For example, at high incident energies, the total energy transmitted through the cell [■] is $\sim 30\%$ larger for P_1 and 50% larger for P_2 than the energy transmitted into the light cone in the absence of refraction [□]. This difference for both pressures is significant when one considers the small change in solid angle for the two cases. For the first case, the solid angle is ~ 0.07 steradian. Probably an even greater amount of pulse energy is refracted. However, in the present experiment, the tube walls prevent a determination of the exact ratio between energy refracted and attenuated, and the distributed breakdown region further complicates the measurement.

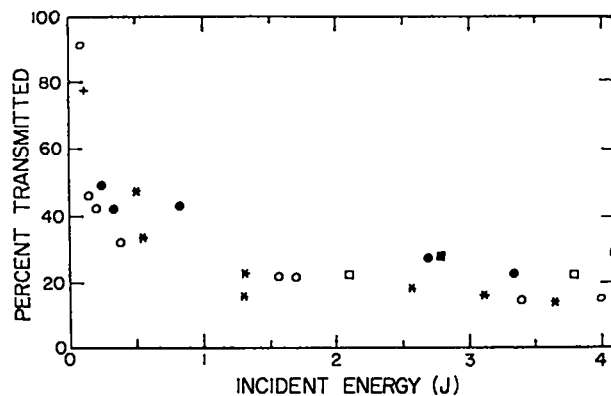


Fig. 19. Percent transmitted energy at 775 torr CO₂.

A detailed analysis of these data will require a pulse propagation-gas breakdown code. Preliminary analysis indicates that the transmission is consistent with the theory that the pulse passes through the focal region virtually unattenuated until the transmitted energy density reaches 5 to 10 J/cm² and the remainder of the pulse is completely attenuated.

Electrically Driven Plasmas -- Work continued on the characterization and understanding of optically induced breakdown in the presence of a large background electron density. In these experiments, a 10- μ m laser is focused through a region of space that can be preionized ($n_e \sim 10^{17}$ /cm³) by an electrical spark discharge in air.

We have measured the attenuation of 10.6- μ m radiation by an electrically driven, laser-augmented plasma in air for laser input energies up to 250 mJ in a passively modelocked train of 50-ns (FWHM) duration. Streak photographs of the plasma evolution with and without the electrical input have also been taken. These experiments employed a segmented pyroelectric detector array with 500- μ m element spacing, and an imaging system having a twentyfold linear magnification and 30- μ m spatial resolution in the plane of the spark. This setup permitted us to measure simultaneously the solid-angle-independent transmission of the plasma, as well as its transmission into the diffraction-limited solid angle of the incident laser beam. These data are displayed in Fig. 21. The error bars include 85% of the observed attenuation values for each laser input energy. This variation is due

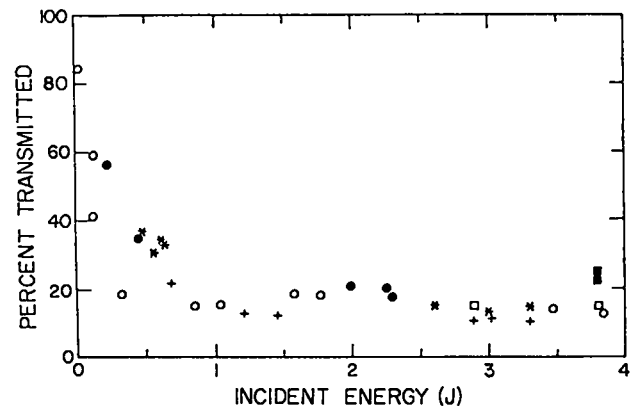


Fig. 20. Percent transmitted energy at 1552 torr CO₂.

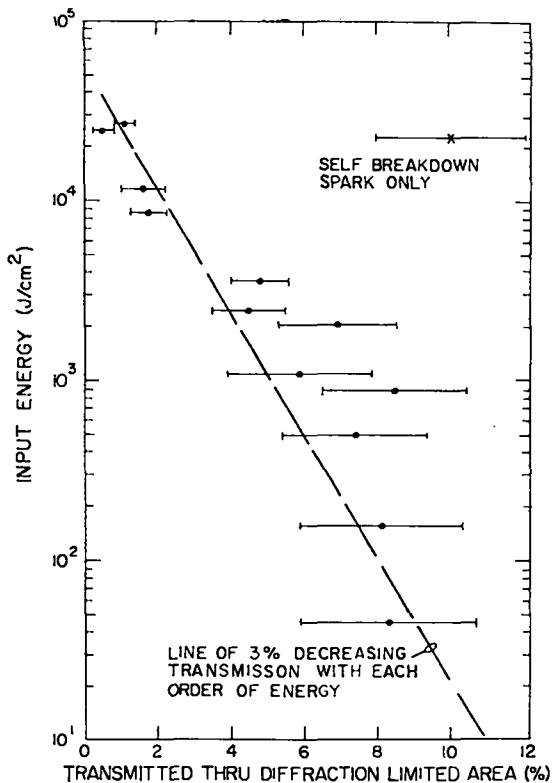


Fig. 21. Percent transmission through electrically initiated spark in air.

to the varying temporal history of the self-mode-locked laser pulse. At energy densities approaching $3 \times 10^4 \text{ J/cm}^2$, the measured transmissions were less than 0.5% into a diffraction-limited cone. An analytical fit to the data in Fig. 21 assumes a 3% decrease in transmitted intensity for each tenfold increase in energy density. As a point of comparison, we measured the pulse transmission in the absence of an electrical spark (10%, $2.3 \times 10^4 \text{ J/cm}^2$ of Fig. 21.). In this case, the transmission was ten times that measured with the electrically initiated plasma. This indicates that the effective absorption constant of a laser-augmented plasma can be improved substantially by preionization of the focal volume.

Streak photographs were taken of the plasma plume (Fig. 22) caused by absorption of the corresponding incident laser pulse (Fig. 23). It was seen that a high-intensity spike occurring early in the laser pulse (Fig. 23, Curve A) produced a corresponding early increase in the plasma light emission (Fig. 22, Curve A). For laser pulses of lower intensity, the plasma emission showed a corresponding decrease (Figs. 22 and 23, Curve B). Structure

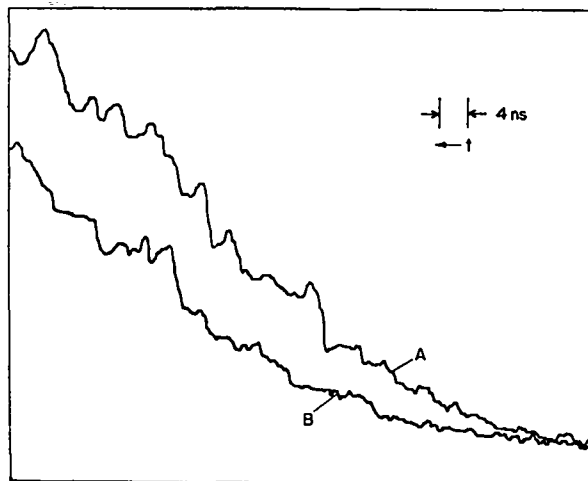


Fig. 22. Densitometer scans of two streak photographs of plasma light.

in the plasma light at an early time (100 ns) did not correspond with the laser time structure. Light emission from the plasma created by the laser proper had a duration exceeding $1 \mu\text{s}$, and the lateral growth of the plume was delayed for several hundred nanoseconds, relative to the beginning of the laser pulse.

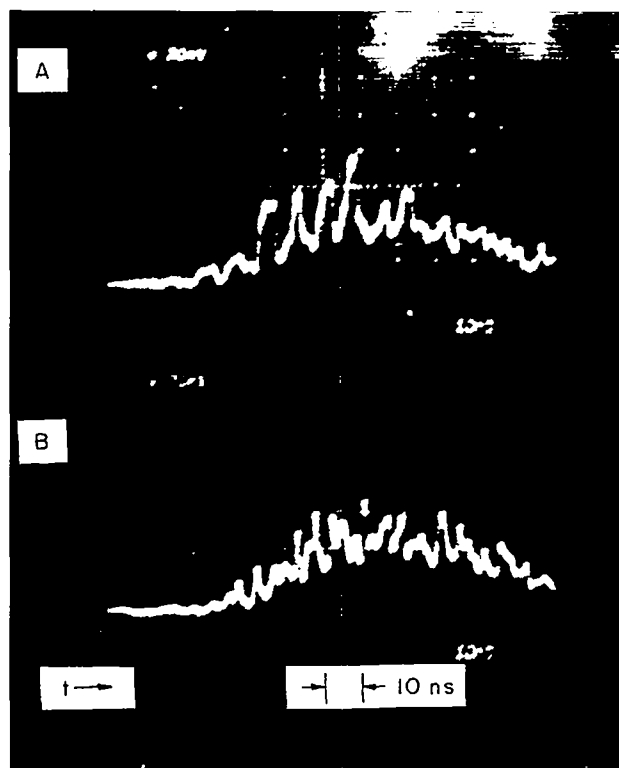


Fig. 23. Laser pulses corresponding to the streak photographs of Fig. 22.

This work will be extended to nanosecond laser-pulse durations, because the streak photographs indicate that the early plasma growth is characterized by brief density fluctuations that are not simply correlated with the laser intensity time history. Recent results show that retro-pulse isolation for CO₂ laser systems via inverse bremsstrahlung may be substantially enhanced by electrical initiation of the plasma.

Aperture Isolator -- Another method of protecting CO₂ laser systems from amplified target reflections is to use self-induced plasma breakdown in a spatial filter. The main amplified pulse deposits some energy in the edges of a pinhole aperture, creating a plasma in the pinhole. With less than one joule of incident light energy, this plasma exceeds the critical density for 10- μ m light for at least tens of nanoseconds. Thus, the isolator, shown schematically in Fig. 24, can be located meters away from the target chamber.

This aperture-isolation device requires accurate beam positioning. In the SBS, we have succeeded in aligning the beam center to within 50 μ m of the aperture center by using pyroelectric detection of the transmitted CO₂ oscillator pulse.

Narrow-Band Resonant Absorbers

Introduction -- Hot CO₂ has often been considered as an isolator for large, short-pulse CO₂ laser systems because of the hot CO₂ line-to-line absorption coincidences with the CO₂ laser transitions. It had been shown that hot CO₂ was unsuitable because of its large saturation flux.¹ However, investigations² revealed that hot CO₂ may be an attractive suppressor of prepulse energy

because of the difference in the bandwidth of the undesired prepulse baseline energy and the desired short pulse. It was subsequently shown³ that by reducing the beam diameter in the hot CO₂ (and therefore raising the intensity), the effective saturation parameter of hot CO₂ could be reduced so that the CO₂ would simultaneously behave as a practical saturable absorber and as a prepulse-energy suppressor.

One-Nanosecond Pulse Results -- Although hot CO₂ was originally considered for quarter-nanosecond systems,^{2,3} we checked our theoretical understanding first by using the recently available one-nanosecond pulses from the GWTF. Our results are in relatively good agreement with theory. The experimental setup (as shown in Fig. 25) is as follows: a 1.0-ns, 0.5-mJ pulse switched out from the smoothing-tube-stabilized GWTF oscillator was directed through two heated Pyrex cells filled with CO₂ and fitted with NaCl windows at Brewster's angle. The cells were 190 cm long, of which 160 cm were heated to 573 ± 10 K for a total heated path of 320 cm. Temperatures were measured with three Chromel-Alumel thermocouples on each cell. The 1-ns pulse clipper consisted of a CdTe crystal (0.8-by 0.8-by 4-cm) switched by a 13- to 16-kV pulse from a LTSG. The resulting pulses were detected by a Moletron-P5-00 pyroelectric detector, and signals were recorded on a Tektronix-7904 oscilloscope.

Figure 26 shows typical results. Note the growth of the second peak as the CO₂ pressure is increased. Even with no hot CO₂ there is a second peak; this is merely ringing in the oscilloscope.

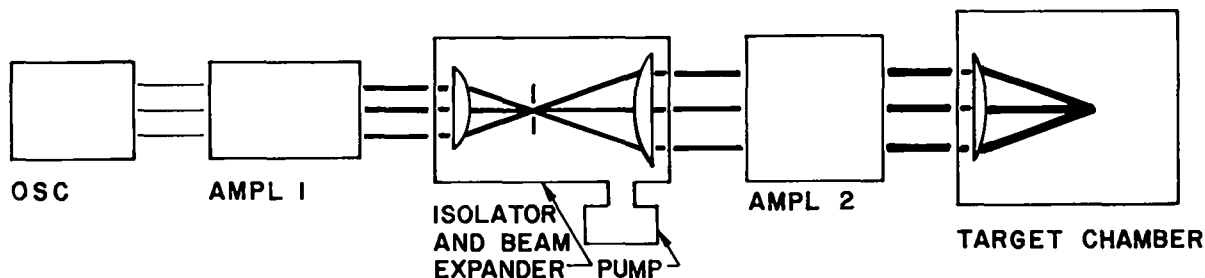


Fig. 24. Retroreflection Isolator.

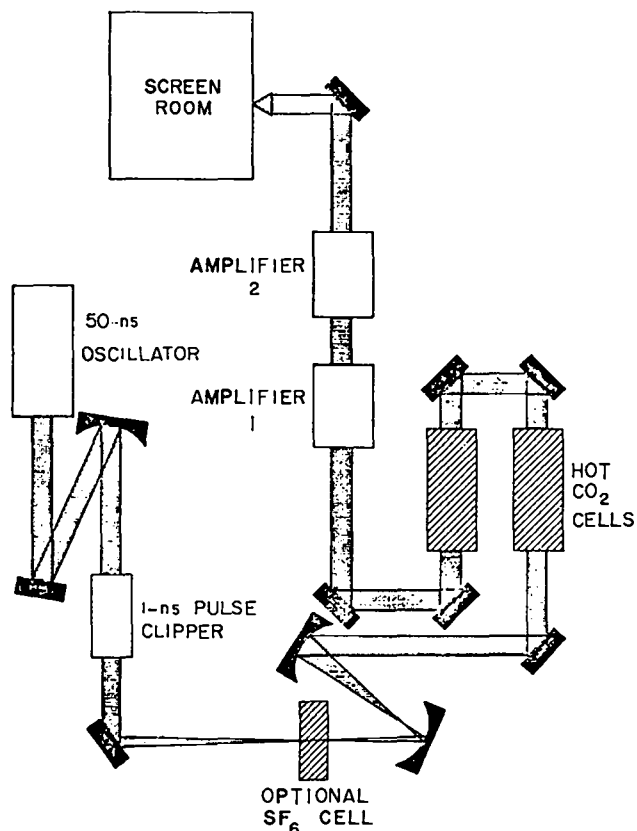


Fig. 25. Adaptation of Gigawatt Test Facility (GTF) for experiments; normally the SF₆ cell and the hot CO₂ cells are missing.

This ringing was subtracted from each picture before evaluating the ringing due to the hot CO₂. Figure 27 shows the measured corrected ratio of the second peak to the first peak as a function of hot CO₂ pressure. This figure indicates that in the linear regime one must use low CO₂ pressures to reduce the undesired secondary ringing. Unfortunately, at these reduced pressures the base line rejection will be only slight because $\alpha_0 l$, the absorption coefficient times cell length, is small (0.554/torr up to 5 torr). The calculated base line reduction factor ($e^{-\alpha_0 l}$) is shown in Fig. 28. Note that adequate baseline reduction is not available at low pressures. Thus, consistent with our expectations, good base line rejection and lack of ringing are incompatible for 1.0-ns pulse durations. However, for quarter-nanosecond pulses, the situation is much improved.

Saturation of either the hot CO₂ or the subsequent amplifier chain will reduce the secondary ringing. Although the pulse was not energetic

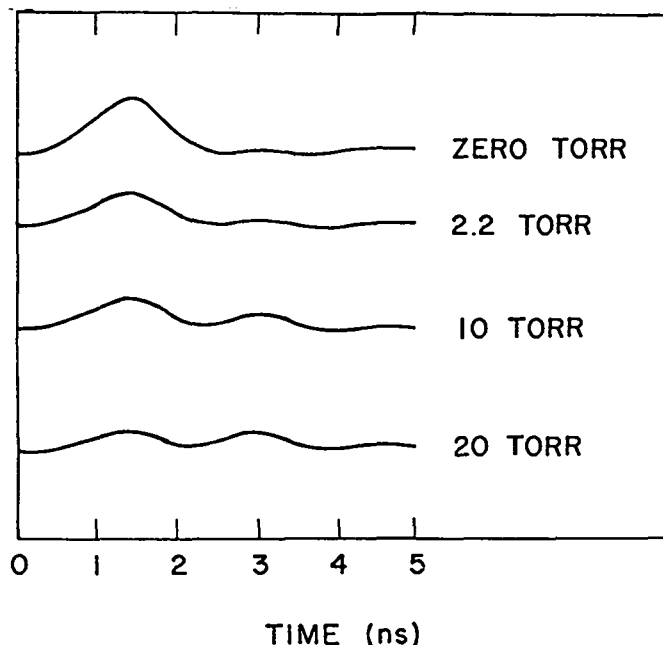


Fig. 26. Reconstruction of oscillograms taken to study ringing induced by short-pulse transmission in hot CO₂. The hot CO₂ pressures corresponding to each shot are indicated in the figure; cell temperature, 573 K.

enough to saturate the entire sample length of CO₂, we telescoped the beam diameter down to see whether any evidence of hot CO₂ saturation could be obtained; our results showed only a slight reduction of the second peak. The testing of saturated operation of hot CO₂ with 1.0-ns pulses will be addressed in a future experiment.

170-Picosecond Results: Pulse Compression in SF₆ -- To test the effects of hot CO₂ on pulses shorter than 1.0 ns, we cannot use the ultrashort pulses generated by optical free-induction decay⁴ (FID - an effect also obtained in hot CO₂), because these FID pulses are characteristically different from the electro-optically switched-out pulses. The FID pulses have a narrow spectral notch in an otherwise broad spectrum, and there is postpulse temporal ringing out of phase, with the main lobe. In our attempt to obtain a shorter pulse, we have tried to compress a 1.0-ns switched-out pulse by saturating SF₆ in a short cell. The beam was telescoped down to a 3-mm diameter (corresponding to $\sim 5 \text{ MW/cm}^2$ in the 1.0-ns pulse) and was passed through a 3.3-cm-long cell of SF₆ heated to 285.8 K. A Rofin photon-drag detector was used.

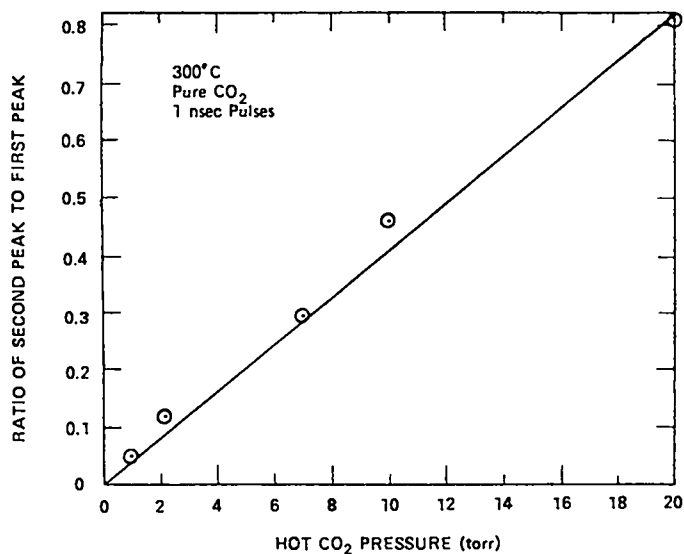


Fig. 27. Measured fractional height of second peak after propagation through hot CO₂ cells. The ringing in the oscilloscope (as in the zero-torr trace in Fig. 26) has been subtracted.

After passage through the SF₆ the pulse passed through the hot CO₂ cells and then through Amplifiers 1 and 2 of the GWTF. The amplifiers were needed because of the attenuation in the SF₆ (~90%). Typical results obtained with 10 torr of

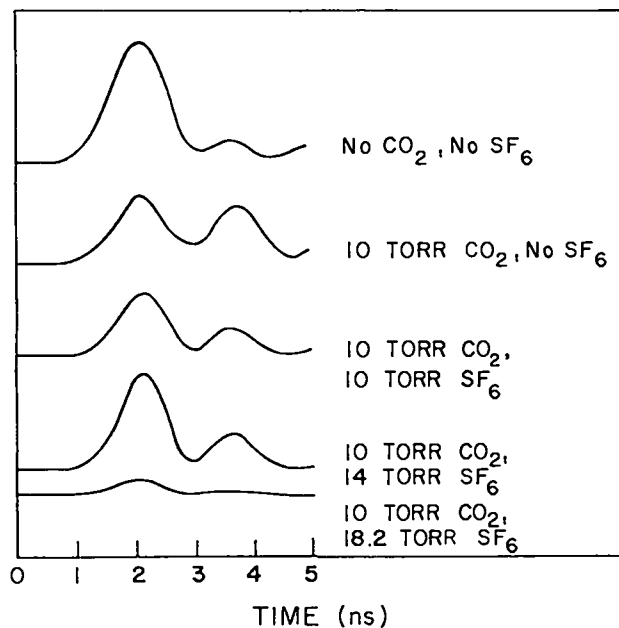


Fig. 29. Reconstruction of oscillograms showing the reduced ringing in hot CO₂ when the pressure in the preceding 3.3-cm SF₆ cell is increased; the vertical scales are different on each of these traces.

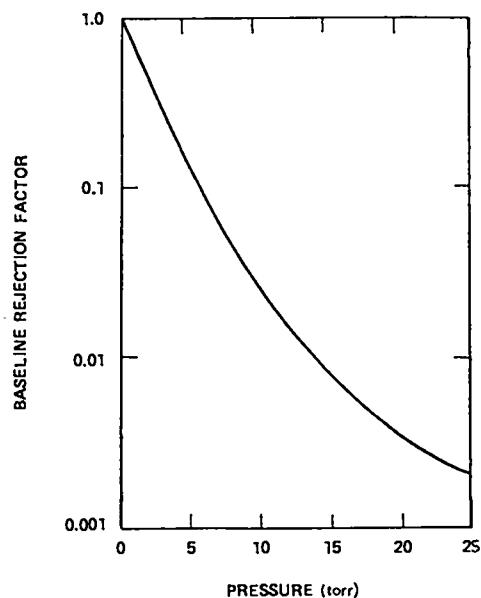


Fig. 28. Calculated base line reduction factor ($e^{-\alpha_0 l}$) versus pressure in the hot CO₂ cells.

hot CO₂ in the cells are shown in Fig. 29. As the pressure of the SF₆ was increased, the hot-CO₂-induced ringing was reduced. Several data points were taken at each of a set of SF₆ pressures; the averaged results are plotted in Fig. 30. Again, detector and scope ringing were subtracted prior to constructing this figure.

Although this evidence is preliminary, it is consistent with the explanation that, at 18 torr,

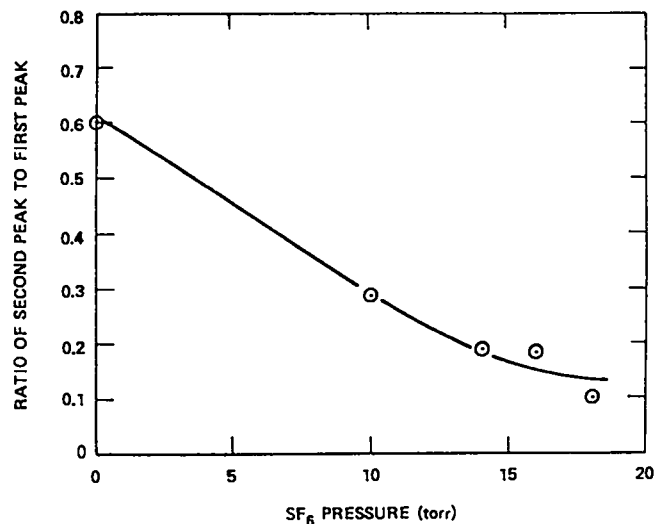


Fig. 30. Measured ratio of hot CO₂-induced secondary peak as a function of pressure in the 3.3-cm SF₆ cell (T = 332 K).

the SF₆ cell reduced the pulse duration by a factor of 6 to 170 ps. This would have reduced the hot CO₂-induced ringing by precisely the same factor. In our numerical simulations in 3.5 m of hot CO₂, the ratio of the second peak to the first is ~0.61 T_p/T₂, where T_p is the duration of the pulse full-width 1/e and T₂ is the homogeneous lifetime of the absorbing transition. There are, of course, other explanations which do not require SF₆-induced pulse shortening; these other possibilities must be eliminated before we can be assured that shortening does occur. We intend to carefully measure the shortening effect with the new 5-GHz scope and with fast detectors.

All results obtained thus far have been consistent with our theoretical models of short-pulse propagation in resonant absorbers.

Diagnostics Development

By using the 5-GHz oscilloscope system and the free-induction pulse generator described in the last progress report (LA-6510-PR), we have begun a comprehensive program to evaluate and improve the current state of the art in subnanosecond infrared detector technology. To date, detectors from Molelectron Corp. and from Santa Barbara Research Co. have been evaluated. Their measured performance was compared to time-domain reflectometer/sampler data on these detectors to determine the accuracy with which detector response time can be predicted from the TDR data.

The Molelectron P5-00 pyroelectric detector used in the above-described system had no appreciable effect on the measured pulse shape as shown in Fig. 31, Curve a. From this test it was concluded that the detector bandwidth was greater than 5 GHz (i.e., <70 ps rise- and falltime with <100 ps FWHM). Figure 31, Curve b shows the TDR/sampler data for the same detector. The oscillations at the beginning of the reflected pulse are caused by a ground loop within the detector and can be eliminated by redesign of the detector mount. If the series inductance L within the detector is significant, then an oscillation will result at the frequency $\omega = 1/\sqrt{LC}$, where C, the detector element capacitance, was measured as 1.2 pF. The absence of oscillation means that

$$L < \frac{CR^2}{4} = 7.5 \times 10^{-10} \text{ H} \quad (2)$$

or that

$$L < (\omega_{\text{tdr}}^2 C)^{-1} = 1.5 \times 10^{-10} \text{ H}, \quad (3)$$

whichever is larger, and the detector risetime L/R could be as short as 15 ps. Falltime of the detector is determined by the RC time constant, which is the risetime of the TDR pulse in Fig. 31, Curve b. From these data, and independently from the measured capacitance, the falltime is ~60 ps to the 1/e point. These TDR results are consistent with the domain measurements. Further work is necessary to completely characterize these detectors

Results of the Santa Barbara Research Co. mercury-doped germanium, liquid-helium-cooled photo-

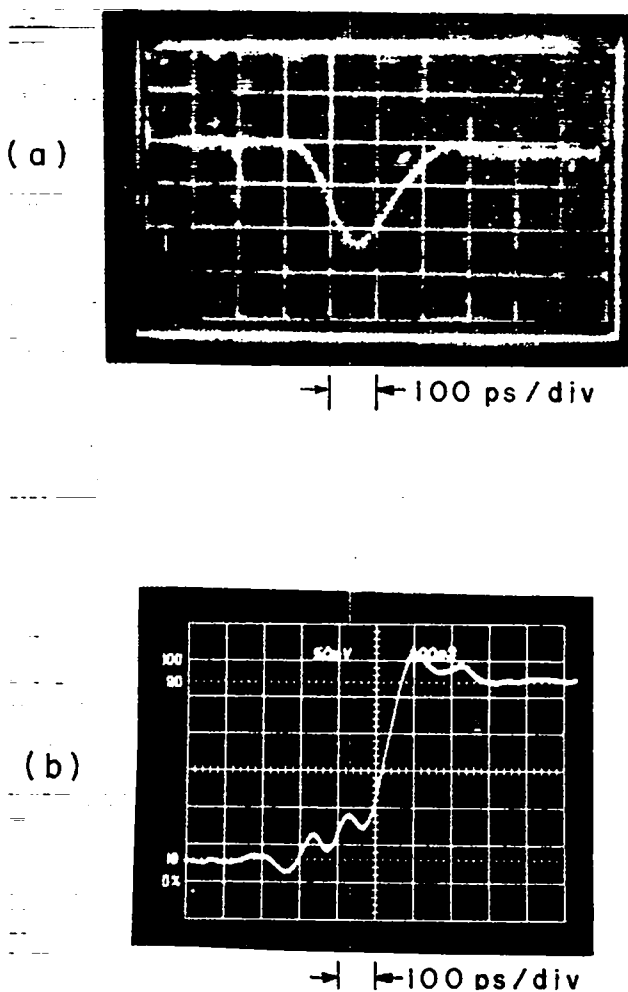


Fig. 31. Pyroelectric detector data: (a) impulse response to 50-ps, 10.6- μm input pulse; (b) TDR data from detector.

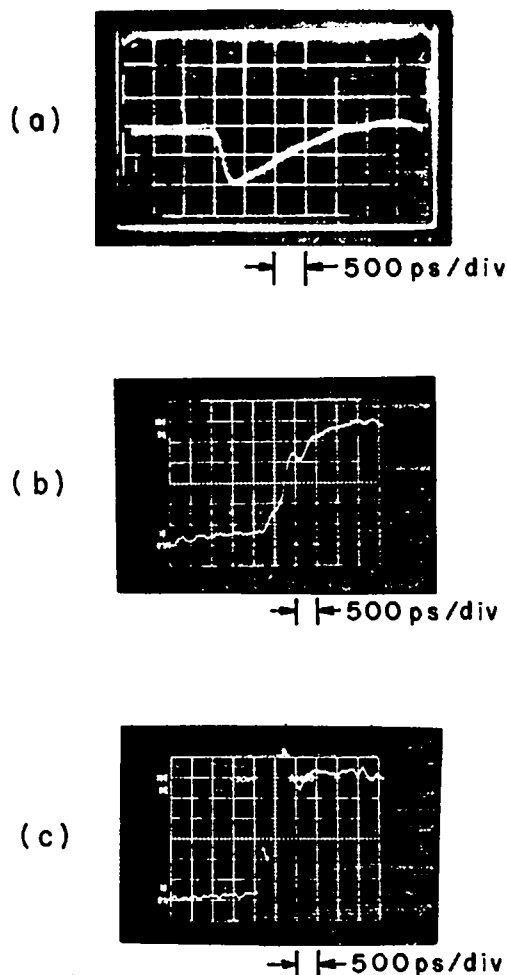


Fig. 32. Mercury-doped germanium detector system data: (a) Impulse response to 50-ps, 10.6- μm input pulse; (b) TDR data with RC coupling network in; (c) TDR data with RC coupling out.

conductive detector data are shown in Fig. 32. The response of the detector to a 50-ps, 10.6- μm pulse is shown in Fig. 32a. The risetime is 200 ps with a falltime in excess of 1 ns. Figure 32b shows the effective RC time constant of the detector system with the coupling network in place, and Fig. 32c shows the time constant of the detector without the coupling network. Our conclusion is that the detector response measured in Fig. 32a is limited by the coupling network capacitor and will be improved by the redesign of this network, already completed. Data will be taken to determine the detector response time so that design improvements can be employed to improve the detector bandwidth to 5 GHz or better.

Optical Damage with 1-ns Pulses

The oscillator-preamplifier system of the Two-Beam System is occasionally available for damage experiments on window and mirror materials and for other experiments that require a 1-ns, 1-J pulse of good beam quality.

A large-diameter (28-cm) sample polished by Harshaw was damaged on the exit surface at a flux of $\sim 2.9 \text{ J/cm}^2$ with a 1.4-ns pulse. Another large sample (20 cm), polished at Air Force Weapons Laboratory, sustained no surface damage up to a flux of 8.7 J/cm^2 , at which point, bulk damage occurred.

The front-end system was also used to investigate the anomalously low sensitivity exhibited by commercial pyroelectric detectors. These units were only one-tenth as sensitive as the commonly advertised sensitivities of 2 to 8 V/mW, and investigation of a Laser Precision Model KT 1540 detector showed that the detector's sensitivity was reduced and its usefulness restricted to either very short or rather long pulses ($>5 \mu\text{s}$) if faithful waveform reproduction is required.

Gigawatt Test Facility (GWTF)

The Gigawatt Test Facility (GWTF) contains a tunable CO_2 oscillator and two amplifiers capable of producing 1-J, 1-ns laser pulses. The facility is being used for studies on the transmission properties of solids and gases, for measurements of the damage thresholds of optical components, and for investigations on other fundamental problems related to the laser-fusion program. Studies of pulse propagation in hot CO_2 and of pulse compression in SF_6 were conducted, as discussed above. The system itself was upgraded by the installation of a spatial filter before the first amplifier.

REFERENCES

1. G. T. Schappert, LASL, unpublished data.
2. B. J. Feldman, R. A. Fisher, E. J. McLellan, and J. F. Figueira, IXth Int'l. Quantum Electronics Conf., Amsterdam, The Netherlands (June 1976).
3. B. J. Feldman, LASL, unpublished data.
4. B. J. Feldman, R. A. Fisher, E. J. McLellan, and S. J. Thomas, IXth Int'l. Quantum Electronics Conf., Amsterdam, The Netherlands (June 1976); also, Opt. Commun. 18, 72 (1976).

II. NEW LASER RESEARCH AND DEVELOPMENT



New types of lasers must be developed to provide the desired energy per pulse, pulse length, pulse shape, wavelength, and efficiency for laser fusion applications. Our advanced laser research has focused on rare-gas oxides and on Hg₂ excimers.

INTRODUCTION

We have placed major emphasis on the investigation of the rare-gas oxides, of molecular mercury, and of methods of excitation of these prospective lasers. The approach we took combined experiments with theoretical analyses. Optical damage measurements on several dielectric coatings have been taken at visible and near-uv wavelengths.

EXPERIMENTAL STUDIES OF RARE GASES AND RARE-GAS OXIDES

General

Primary efforts included (1) investigations of Ar-O₂ gas mixtures at high pressures in an electron beam-controlled electrical discharge; (2) continued kinetics studies of the rare gases and rare-gas oxides using high-power optical pumping techniques; and (3) testing and modification of the Cassandra electron beam accelerator for rare-gas oxide laser studies.

Electron Beam-Controlled Electrical Discharges

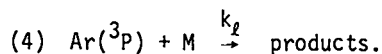
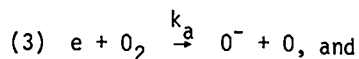
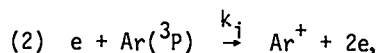
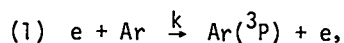
Improvements have continued in the high-pressure electron beam-controlled discharge system. The electron beam now operates at a beam voltage of 230 kV and a current density of 1 A/cm² incident on the gas. This system has been used to investigate electrical-discharge initiation in several gas mixtures at high pressure.

We have demonstrated stable operation in nitrogen up to 7800 torr at discharge current densities of 270 A/cm² at an electric field-to-particle density (E/N) ratio of 2×10^{-16} V·cm². Analysis of voltage and current waveforms indicates that the discharge behaves quantitatively as expected: The discharge is recombination-controlled with a measured recombination coefficient of 3.5×10^{-8} cm³/s. Electron densities of 6.7×10^{14} /cm³ have

been achieved. The discharge has also been observed in pure argon up to 7800 torr; current densities in the range of 100 to 200 A/cm² have been obtained, corresponding to an electron density $< 10^{15}$ /cm³. The addition of oxygen to argon changes the discharge behavior markedly. Observed oscillations in the gas discharge current and voltage are attributed to the dissociative attachment instability. In addition, the absolute stability of the discharge current (exponential growth coefficient) decreases as the oxygen concentration is reduced to 2%. The electron density produced in the discharge under stable operating conditions appears to be near 10^{14} /cm³.

We have also used our Boltzmann computer code to calculate the electron-distribution functions, transport coefficients, and inelastic excitation rates for Ar-O₂ gas mixtures as a function of E/N. Twenty-nine inelastic processes occurring in the two gases have been incorporated into the calculation; the code has been checked in various limits and is now operational. The data developed from this calculation are necessary for evaluating the performance of the electron beam-controlled discharge.

The discharge instability in Ar-O₂ gas mixtures can be understood on the basis of processes occurring in the discharge, as described by the following set of reactions:



We have assumed that the dominant sources of avalanche ionization are the excited electronic states (Reaction 2) and have assigned a general loss pro-

cess (Reaction 4) for these states. The equations describing these processes are

$$\frac{dn_e}{dt} = S_0 + (k_i n^* - k_a n_a) n_e \quad (1)$$

and

$$\frac{dn^*}{dt} = k n n_e - k_l n^* \quad (2)$$

where n_e is the electron density, n^* is the $\text{Ar}(^3P)$ population density, n_a is the density of attaching molecules, n is the number density of ground-state argon, and S_0 is the ionizing source function due to the external electron beam. We then consider the linearized solutions to these coupled equations and look for unstable solutions. Instability is found for the zero-order condition¹

$$k_a n_a \leq 2k_i n_0^* \quad (3)$$

where n_0^* is the zero-order value of n^* .

Because k_i and k_a depend only on E/N , Eq. (3) may be rewritten

$$\frac{n_a}{n} \leq 2 \frac{k_i}{k_a} \frac{n_0^*}{n} = f(E/N) \quad (4)$$

Because the middle term is primarily a function of E/N , Eq. (4) predicts that the discharge will become unstable if the fractional concentration of the attaching gas (O_2) is decreased. This is observed experimentally; substitution of calculated quantities into Eq. (4) also indicates semiquantitative agreement.

The experimental device has been upgraded to reduce interference of transients with the acquisition of data; testing of these modifications is in progress. We also intend to incorporate a crowbar switch on the gas-discharge power supply to alleviate discharge arcing problems after turnoff of the electron beam. Diagnostics will be incorporated to measure the fluorescence of the 557.7-nm transition in ArO and the 125-nm radiation from Ar_2^* . These measurements will provide information about the

efficiency for electrical discharge production of the lasing species and the related kinetic processes.

Kinetic Studies in Rare Gases and Rare-Gas Oxides

We have continued optical pumping experiments aimed at understanding the basic kinetics of krypton and xenon and the transfer kinetics from their excited atoms and molecules to receptors such as O_2 and N_2O . Figure 33 shows the potential-energy curves of the states of interest. If a Kr_2^* light source is used to pump the 3P_1 level of xenon and if the xenon is at low pressure, then the three-body reaction via k_1 is very much slower than the two-body relaxation via k_2 . Under these conditions, molecular formation via k_4 is observed by monitoring the excimer signal at $\lambda \approx 172$ nm originating from the lowest bound molecular states. Figure 34 is a plot of the decay frequency of the emission decay at 172 nm versus xenon pressure. The data at low pressure yield a three-body association rate of $1.4 \times 10^{-31} \text{ cm}^6 \text{ s}^{-1}$. At higher pressure, the data indicate a rate of $\sim 8.5 \times 10^{-32} \text{ cm}^6 \text{ s}^{-1}$ and are in closer agreement with published values. Note that our data at higher pressure do not extrapolate through the origin and that this (higher) pressure region is the lower limit for the majority of the work reported in the literature.

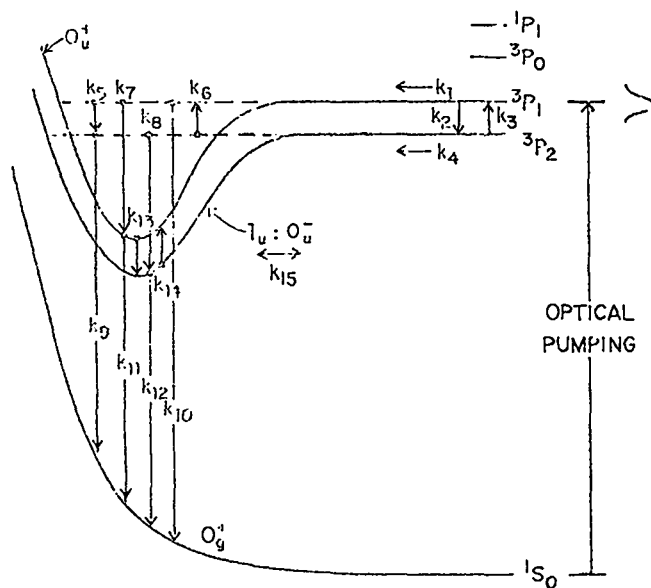


Fig. 33. Representative potential-energy curves and three-body association rates for krypton or xenon.

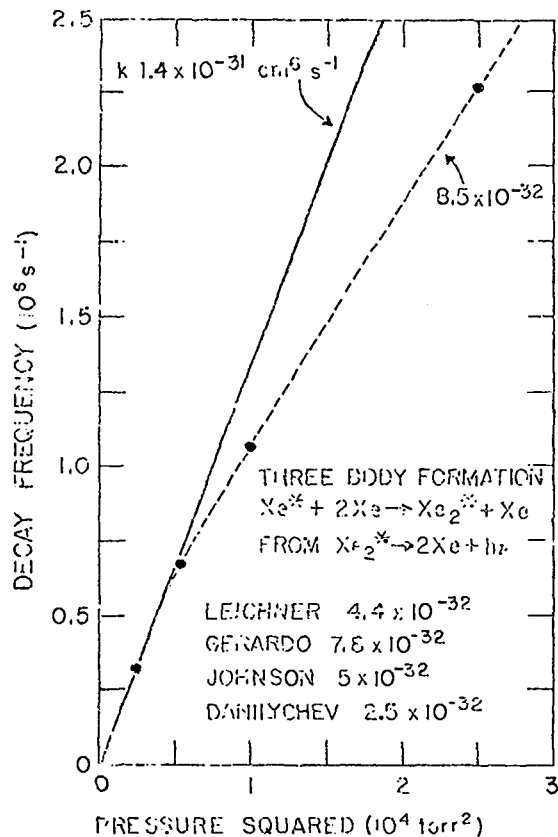
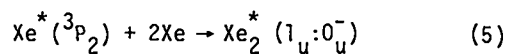


Fig. 34. Final decay frequency of the excimer signal from low-pressure xenon versus xenon pressure squared. The linear part of the curve is used to calculate the three-body association rate out of $Xe(^3P_2)$.

Evidently, the process



can be clearly observed only at low pressure. Here we consider the 1_u and 0_u^- states as a single state, $1_u:0_u^-$, because they are degenerate. A similar experiment was conducted in krypton; these results are presented in Fig. 35.

Kinetics data have also been obtained in high-pressure krypton. A fluorescence signal at 145 nm, before and after computer processing, is shown in Figs. 36 and 37, respectively. The base line corrected and normalized data are plotted on a logarithmic scale in Fig. 37 over a subjectively chosen time interval. Excellent signal-to-noise ratios are obtained over a reasonably wide dynamic

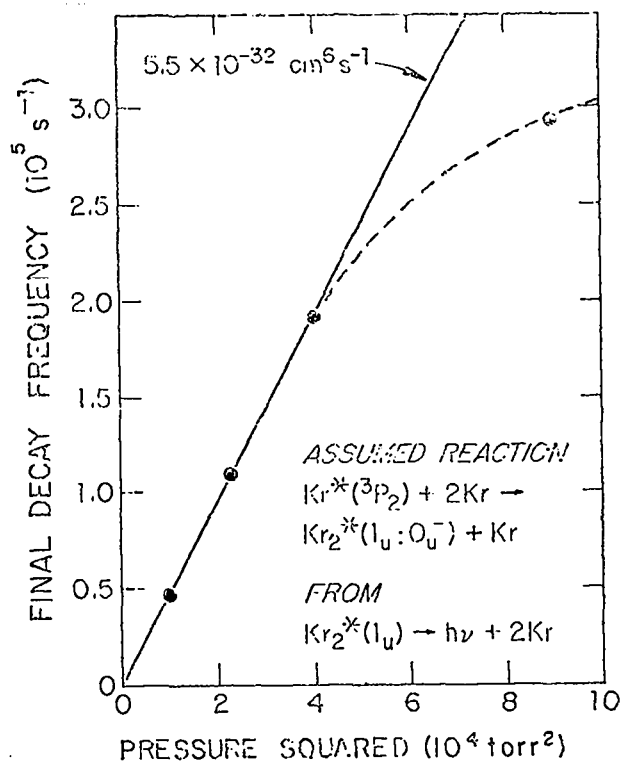


Fig. 35. Final decay frequency of the excimer signal from low-pressure krypton versus krypton pressure squared. The linear part of the curve is used to calculate the 3 three-body association rate out of $Kr(^3P_2)$.

range of signal level. Data taken to determine the pressure-dependent lifetime of the 0_u^+ and $1_u:0_u^-$ states in krypton are shown in Figs. 38 and 39, respectively. The lifetimes extrapolated to zero pressure are 5.7 and 286 ns, respectively. The observed pressure-dependent lifetimes could be due to a variety of effects, including excited-state mixing, quenching, collisional stimulation, and trimerization. The latter two processes represent radiative losses at other wavelengths.

Collisional transfer from excimer donors to background gas acceptors has been investigated for other reactions of interest in rare-gas oxide lasers, and the results include:



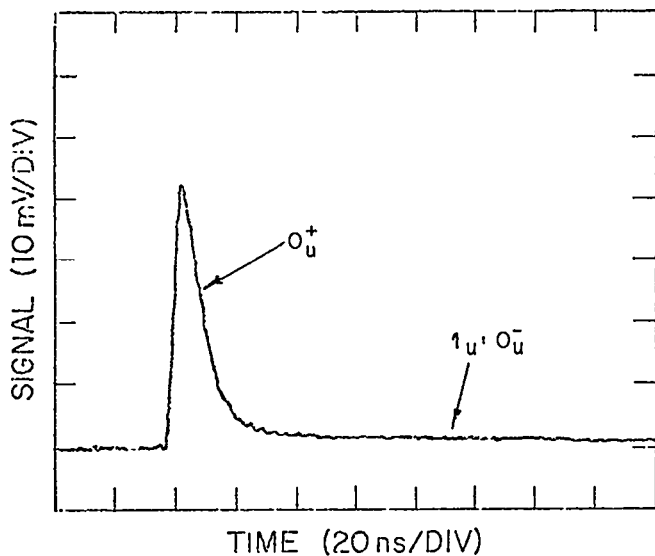


Fig. 36. Excimer emission versus time from high-pressure optically pumped krypton.

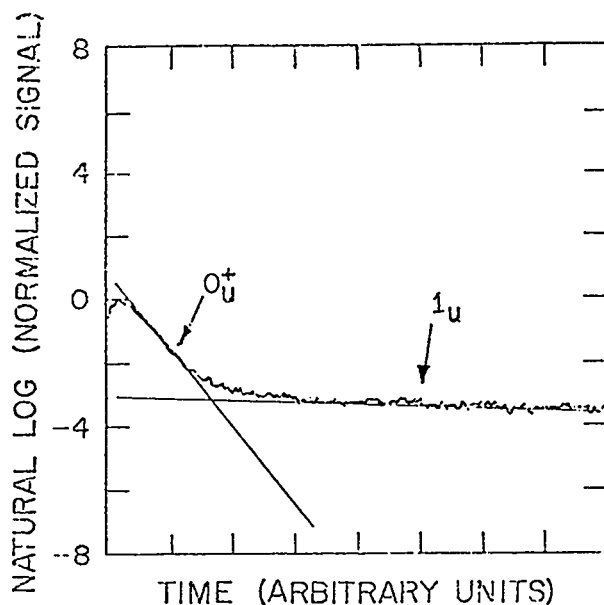


Fig. 37. Excimer signal shown in Fig. 36 plotted on a logarithmic scale with straight-line fits to the double exponential signal.

In comparison, a rate of $10^{-10} \text{ cm}^3 \text{ s}^{-1}$ was obtained for Reaction 1 with a quiescent light-output technique¹ rather than in a lifetime measurement as in our experiments. Another group used direct electron beam deposition in a Xe- O_2 mixture² and measured a rate of $1.5 \times 10^{-10} \text{ cm}^3 \text{ s}^{-1}$ for Reaction (3). Our more recent data for Reactions (1) and (3) deviate from the literature references by more than

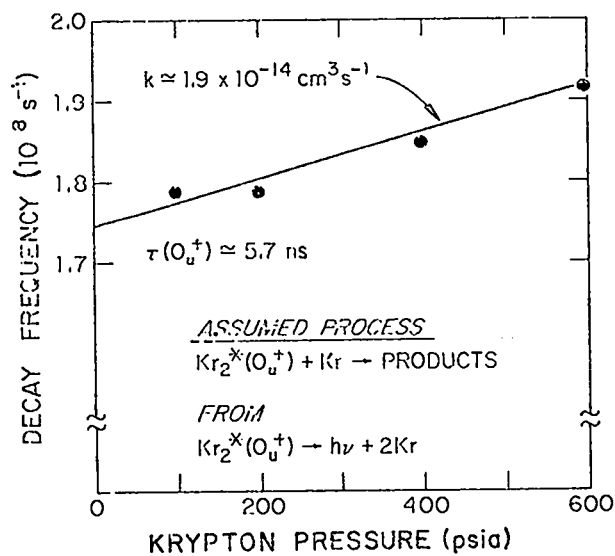


Fig. 38. $\text{Kr}_2(\text{O}_u^+)$ decay frequency versus krypton pressure.

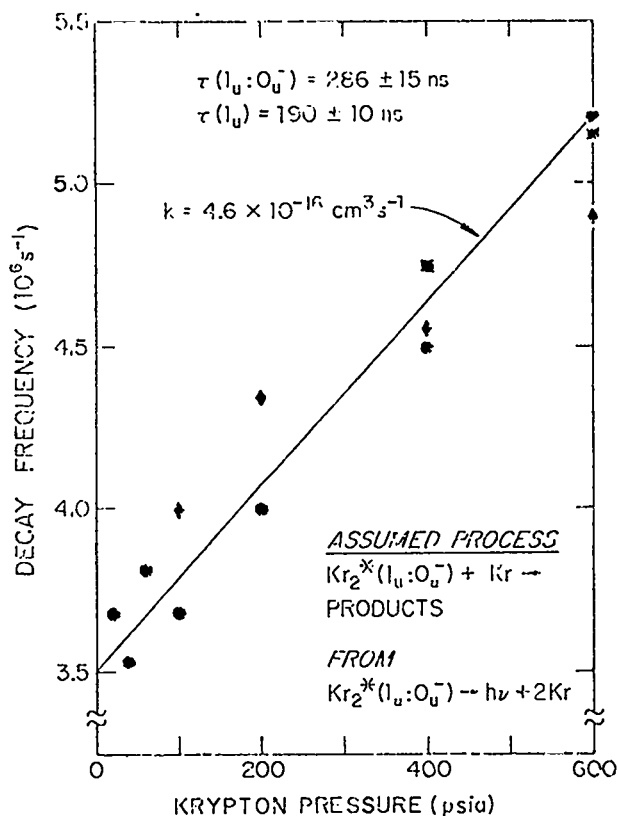


Fig. 39. $\text{Kr}_2(1_u, \text{O}_u^-)$ decay frequency versus krypton pressure.

a factor of 3. Currently, deviations of this magnitude are common and could have very drastic effects on the results of code calculations for rare-gas oxide lasers, particularly if more than one rate in the code was uncertain to such a degree. The uncertainty in our experiments is relatively small, $\sim +20\%$, and is largely determined by uncertainties in signal-to-noise ratio and gas pressure. In addition, the processes are well defined because of the relatively simple excitation conditions and the fact that the experiments were performed at high krypton and xenon pressures, where excited-state identification in the rare gas is straightforward.

High-Energy Electron Beam Experimental Facilities

The Cassandra electron beam accelerator is a large device intended for excitation studies of high-pressure gas laser systems; its characteristics are:

Beam energy	2 MeV
Beam current	200 to 400 kA
Current duration	20 or 40 ns
Current risetime	11 ns
Energy deposition	15 kJ
Transverse dimension	50 cm by 4 cm or 100 cm by 2 cm.

Both 5- and 10- Ω transmission-line configurations are available for the machine. The 5- Ω line has performed satisfactorily. During performance tests of the 10- Ω line, carried out at LASL by representatives of Maxwell Corp., the main output switch failed catastrophically. The damage was limited to the switch, but a replacement will not be available until early December 1976, and the machine is therefore inoperable in both configurations.

During this downtime, we are incorporating some modifications into the design to prevent damage to other parts of the machine and possible injury to operating personnel in the event of another switch failure. These changes include the erection of large standpipes on the top of each section of transmission line to release the pressure generated during such a switch failure. These modifications should be completed by the end of October 1976.

The fabrication of the laser chamber for this machine is near completion and delivery is expected by mid-October. Pressure testing will be performed by the vendor. The chamber will be installed on the electron beam machine as soon as operation is resumed. Experiments will be initiated immediately thereafter.

METAL VAPOR LASERS

Introduction

As discussed in the last progress report (LA-6510-PR), many low-vapor-pressure metals offer the possibility of laser action in their molecular form either as pure metal-vapor dimers (or trimers) or in combination with buffer-gas atoms to form excimers. Such molecules may lase because they radiate either in bound-free transitions or in bound-bound transitions between states with displaced potentials. In either case, a population inversion is virtually assured whenever an upper-state population is produced.

For most metal vapors, the cross sections for excitation to the resonance levels dominate all other inelastic electron-collision cross sections at low energies; it therefore appears that energy could be deposited into these prospective laser systems most efficiently by means of electrical discharges. Our efforts to develop metal-vapor lasers, therefore, have been directed toward developing techniques for producing high-pressure, pre-ionized transverse electrical discharges in these high-temperature corrosive gases and confinement of these gases in heat pipes.

The primary systems studied to date include mercury and the alkali metals. The former was chosen, e.g., because of its relatively high vapor pressure (reasonable pressures can thus be obtained in a heated cell without the need of a heat pipe); because of recent acquisition of accurate data concerning the lowest-lying molecular states, appropriate lifetimes, and kinetic rates;³ and because our calculations indicate that mercury may offer extremely high efficiency at an attractive wavelength for laser fusion. The alkali metals were chosen because a wealth of data exists on alkali dimers, alkali monomers, and alkali rare-gas

complexes, and because considerable previous experience has been gained in our laboratories in the use of these metals as heat-pipe fluids.

Electrical Discharges in Mercury

Successful transverse discharges have been obtained in high-pressure mercury by using the apparatus shown in Fig. 40 (see LA-6510-PR). The initial results were obtained in a transverse-discharge structure with an area of 11.5 by 1.5 cm and an electrode spacing of 9.6 mm. The discharges were initiated by uv preionization produced by a flashboard, which consisted of tungsten dots deposited on an alumina substrate. The flashboard illuminated the discharge volume from the side. Uniform glow discharges could be obtained over a wide range of current densities. Low current discharges were obtained with a CuSO_4 resistor to limit the current density to ~ 100 to 200 mA/cm^2 . The discharge was a very uniform transverse glow, which quickly stabilized to a steady-state value of $E/N = 1$ to $2 \times 10^{-16} \text{ V}\cdot\text{cm}^2$, which could be maintained for ~ 60 to $70 \mu\text{s}$ before becoming unstable and arcing. This value of E/N is quite appropriate for depositing a large fraction of the input electrical energy into the $^3\text{P}_1$ mercury atomic state. Our calcula-

tions of energy deposition as a function of E/N show that for an $E/N < 3 \times 10^{-16} \text{ V}\cdot\text{cm}^2$, more than 80% of the discharge energy can be coupled into the $^3\text{P}_1$ state.

The discharge characteristics have also been studied in the much more interesting high-current-density mode. In this mode of operation, the current-limiting resistor is removed and a capacitor is discharged across the electrodes through a thyatron switch after an appropriate delay ($\sim 0.5 \mu\text{s}$) following the preionization pulse. Results for the discharge behavior at atmospheric pressure (750 torr) are shown in Fig. 41. These results correspond to a peak current density of $\sim 6 \text{ A/cm}^2$ at $E/N \approx 2 \times 10^{-16} \text{ V}\cdot\text{cm}^2$ for a duration of $\sim 1.5 \mu\text{s}$ (FWHM) and a specific energy deposition of 15 J/l into the gas. Crude calculations indicate that under the most favorable conditions of conversion from $^3\text{P}_1$ excited atoms to $^3\text{I}_u$ excimers, a steady-state density of $N(^3\text{I}_u) \approx 2 \times 10^{15} \text{ cm}^{-3}$ could be obtained. Such an excited-state density, together with the stimulated-emission cross section of $\sim 10^{-18} \text{ cm}^2$ deduced in a positive gain measurement on Hg_2 ,⁴ yields an estimated maximum gain of $\sim 0.2 \text{ cm}^{-1}$.

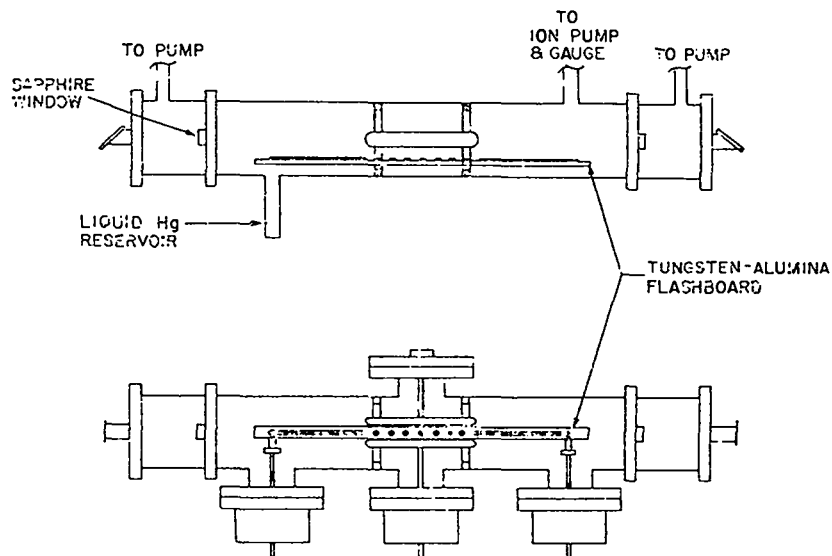


Fig. 40. Schematic of heated-cell transverse discharge apparatus for high-pressure mercury.

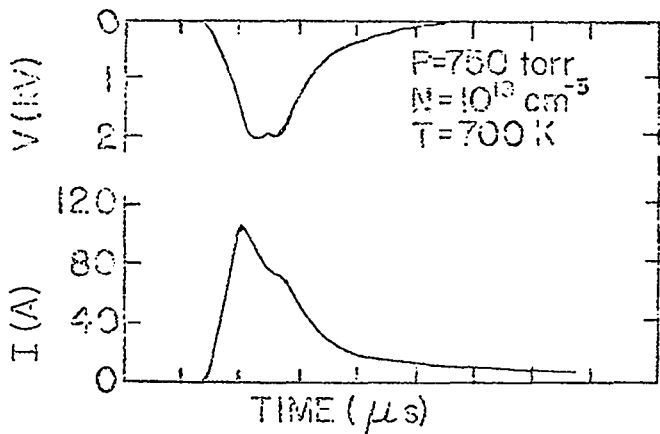


Fig. 41. Oscilloscope recording of voltage (upper trace) and current (lower trace) of high-pressure, high-current-density ($J \approx 6$ A/cm²) mercury transverse discharge.

We measured the gain with the apparatus depicted in Fig. 42. In this very simple technique, a He-Cd laser operating at 325 nm (i.e., at 66% of the Hg₂ gain curve, as illustrated) is used as a probe beam to search for gain during the discharge pulse, at a current density of ~ 6 A/cm². The results of such a measurement are illustrated in Fig. 43. As can be seen, the transmitted laser signal decreases sharply shortly after application of the discharge pulse. The predicted gain may exist early in the pulse but may be masked by the noise in the laser signal. However, the loss of signal is substantial and occurs very rapidly after excita-

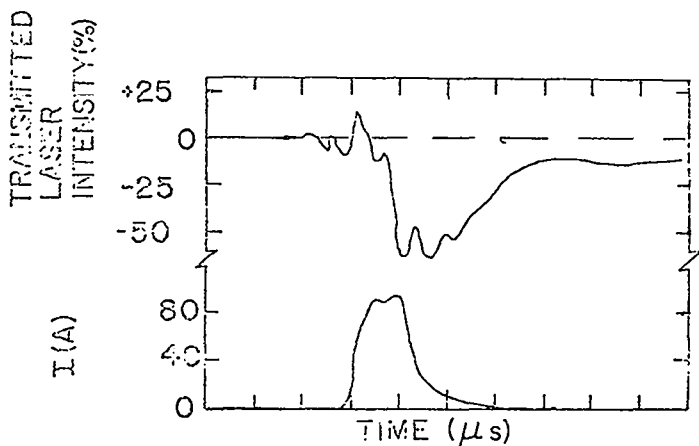


Fig. 43. Oscilloscope recording of results of gain measurement in mercury. Upper trace is probe-laser signal, lower trace is discharge current. The conditions for this measurement were $J \approx 6$ A/cm², $N \approx 10^{19}$ cm⁻³.

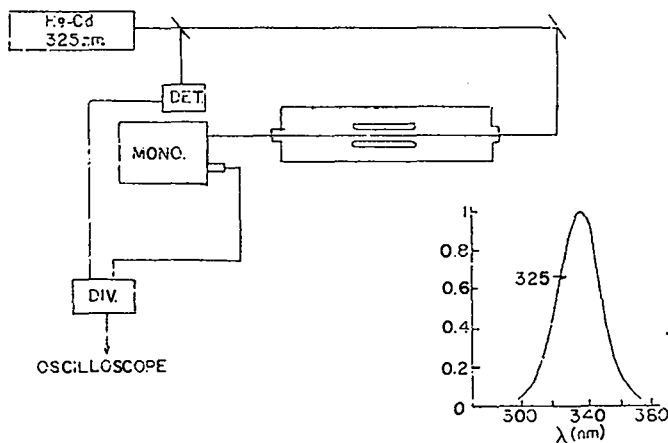


Fig. 42. Apparatus for measuring gain on 335-nm Hg₂ band in discharge-excited mercury vapor.

tion. Initially, we thought we needed a monochromator in front of the detector to reject the spontaneous emission, but any refractive effects could then cause a large signal change as the beam was swept across the slits. Later, however, the experiment was reproduced with a narrow-band interference filter and diffuser in front of the detector. Under these conditions, the data are essentially those shown in Fig. 43. Furthermore, the experiment was repeated with a He-Ne laser at 632.8 nm as the probe beam in place of the He-Cd laser. A signal change of less than 0.2% was observed during the discharge pulse. This result seems to rule out strong refractive effects, and the negative gain measurement must now be explained as an absorption process. For an order-of-magnitude calculation, let us assume that the 3_1 u state is responsible for the absorption and that the estimated density of such excimers is, as above, $\sim 2 \times 10^{15}$ cm⁻³, then a lower limit of the absorption cross section would be $\sim 3 \times 10^{-17}$ cm².

Because of the importance of the gain measurement for this prospective laser system, we will repeat this measurement over a wider range of discharge operating parameters. The addition of other gases may be useful to provide clues as to the source of the apparent absorption. Also, the measurement should be repeated at other wavelengths across the 335-nm band; a tunable dye laser will be used for this purpose. Because of the low gain coefficient, the gain measurement will also be re-

peated over a longer gain path length. For this purpose we have fabricated a 50-cm-long electrical discharge system to fit into our present hot cell.

In a related discharge study, we have now completed an apparatus to study the feasibility of using radioactive preionization (tritium) in mercury discharges. This effort was motivated by the recent success⁵ with such a technique applied to CO₂ mixtures and by the fact that mercury, having a negligible electron attachment rate and a reasonable recombination coefficient, seems to be ideal for this type of preionization. In mercury, the dominant electron loss process will be dissociative recombination with a maximum rate $k_r \approx 5 \times 10^{-7}$ cm³/s.⁶ The steady-state electron density can then be computed from the equilibrium condition

$$\frac{dn_e}{dt} = k_e - n_e^2 k_r = 0, \quad (6)$$

where k_r is the recombination coefficient, k_e the electron production rate, and n_e the electron number density. Using the value of $k_r \approx 10^{-7}$ cm³/s given above, the electron density is

$$n_e \sim 3 \times 10^6 P^{1/2} \text{ cm}^{-3}, \quad (7)$$

where P is the tritium pressure in millitorr. Thus, a pressure of only ~100 mtorr will produce a steady-state density $n_e \sim 3 \times 10^7$ cm⁻³, which exceeds that produced by uv preionization⁴ under typical conditions⁷ and is uniformly distributed automatically throughout the volume. Data will be obtained in the very near future, and, if successful, will lead to a considerable simplification of the discharge apparatus because no high-temperature feedthroughs and no auxiliary circuitry will be required for the preionization.

To complete this study, we have also investigated α -emitter sources for preionization of electrical discharges. The studies were carried out in He-N₂ mixtures using an americium-241 α -emitter. The results were encouraging, but the technique seemed to be of limited use and has been discontinued.

Heat Pipe Experiments

Experiments have been performed to investigate the operation and characteristics of heat pipes as containment vessels for corrosive metal vapors in laser applications. Test devices have been constructed that range in diameter from 1.9 to 9.8 cm and have been operated with water, mercury, and sodium as working fluids. A considerable amount of data has been collected about various aspects of heat pipe performance applicable to laser operation including interface behavior, scalability, and optical homogeneity.

We derived the following basic conclusions. We are able to produce reasonably uniform gas volumes at pressures up to 1 atm in a small (1.7-cm-diam) device. Some optical aberration, apparently at the interface zones, was static and therefore correctable. Above 1 atm there was some temporal disturbance of the optical homogeneity. When the aperture of the device was increased to a diameter of 3 cm, the quality of the medium degraded enormously, even at relatively low pressures. If water was used as the working fluid, vertical interfaces (see LA-6510-PR) could be obtained only for narrow ranges of buffer-gas density, and even when a vertical interface was obtained there were signs of turbulence and cloud formation; a strong tendency toward instability and stratification of the gases was also noted. With the large-diameter device, vertical interfaces could not be obtained under any circumstances with mercury as the working fluid, primarily because no inert gas is heavy enough to match the density of the mercury. It thus appears that an upper diameter limit of ~3 cm exists for heat pipes that will be capable of producing optically uniform vapors. Large-aperture devices may require systems with arrays of small-diameter heat pipe arms. This possibility is being investigated, together with further experiments to quantify the vapor behavior at the interface zone.

The initial 9.8-cm-diam sodium heat pipe was tested, but had a very short life due to the presence of some low-purity alumina in the central discharge section. The impurities, mainly silicas, resulted in very fast attack by the sodium on the high-temperature feedthroughs and discharge structure, which led to the failure of the cell. However, some preliminary information suggested that

at low pressures (<10 torr) the heat pipe functioned properly and produced a reasonably uniform vapor zone. However, at high buffer-gas (argon) pressures, the vapor exhibited an unusual absorptive character. A white light source, when viewed through the cell, appeared green. As the sodium vapor pressure was increased to ~4 torr, the light changed to a blue tint. When buffer gas was added to ~350 torr, the cell became totally opaque and remained so at higher pressures. This behavior has been observed previously,⁸ but has yet to be explained; it has obvious ominous implications for laser application of sodium vapor. We are attempting to analyze this mechanism by constructing an improved version of the sodium heat pipe in which the discharge inputs will be brought in from the ends of the tube and the temperature of the central portion of the cell will be controlled by a separate concentric heat pipe oven, which will produce a very uniform isothermal zone.

OPTICAL DAMAGE STUDIES

Introduction

The damage resistance of optical thin-film components has proven to be a major limitation on the peak intensity attainable for laser-fusion experiments at 1.064 μm . It is expected that damage to optical components will be even more severe at shorter wavelengths, due to the probable onset of multiphoton absorption as a damage mechanism at high intensity.

Previous laser damage experiments at 1.06 and 0.694 μm have provided a useful, though incomplete, characterization of various thin-film materials. However, no reports of controlled tests below 0.694 μm have been found. We have carried out experiments at 0.355, 0.532, and 1.064 μm to measure damage thresholds in three refractory oxide coatings. These results are summarized below; more details are contained in Ref. 9.

The refractory oxides TiO_2 , ZrO_2 , and HfO_2 were chosen for evaluation because they have been successfully used as the hard, high-refractive-index components of multilayer stacks for use at 0.694 and 1.064 μm . Silica (SiO_2) films, often used as hard, low-refractive-index components, were

also selected for evaluation. Single-layer films of TiO_2 , ZrO_2 , and SiO_2 were evaporated onto fused silica substrates (Optosil I) by two commercial vendors who represented the state of the art of electron gun technology. The HfO_2 films were deposited on Ultrasil substrates by electron gun evaporation at the University of Rochester. Film thicknesses of one quarter-wave ($\lambda/4$) at 0.355, 0.532, and 1.064 μm were obtained. Spectral transmission curves for these films are shown in Fig. 44.

Hafnia (HfO_2) was of special interest because of its short-wavelength cutoff at 0.230 μm . Although the HfO_2 films showed absorption at 0.250 μm (unbaked), heating to 673 K in air would have shifted the edge to 0.230 μm .¹⁰ There are a few reports of rf sputtering and electron gun deposition of this material, but its damage resistance has not been published previously.

Experimental Procedure

The experimental apparatus and techniques used in our studies were similar to those described previously;¹¹ the experimental parameters are listed below:

- wavelength: 1.064, 0.532, and 0.355 μm
- pulsewidth: 30, 20, and 17 ps
- spot-size radius (W): 0.12 to 0.22 mm
- single shot per irradiated site
- shots per threshold measurement: 40 (av)
- normal incidence.

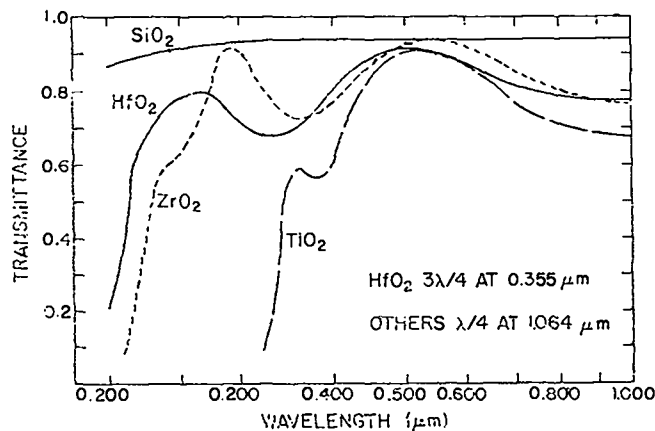


Fig. 44. Spectral transmission curves for test samples. The peak values for HfO_2 and TiO_2 are low due to a wedge in the samples.

The damage thresholds measured in this study are listed in Table IV. The results for 1.064 μm are typical of commercial coatings, with the exception of the low value for one of the TiO_2 samples. The threshold energy densities for each film material for a selected manufacturer are plotted versus wavelength in Fig. 45. Between 1.064 and 0.532 μm , the damage thresholds of TiO_2 and ZrO_2 increase, whereas the threshold of HfO_2 is rather constant and that of SiO_2 decreases. The thresholds for all four materials decrease rapidly between 0.532 and 0.355 μm .

Characterizing these results in terms of incident energy density does not describe the films completely. It has been established that the standing-wave (SW) electric field must be taken into account when evaluating damage resistance.^{11,12} In particular, the fields in a quarter-wave-thick film of HfO_2 at 0.355 μm are quite different for 0.532- and 1.064- μm irradiation (see Fig. 46). The same is true for TiO_2 and ZrO_2 . Of course, minimal electric-field variations occur in SiO_2 films on fused silica substrates. Moreover, the damage resistance may be dependent on the pulsedwidths, which were different for each laser wavelength.

A more quantitative measure of damage resistance is the rms electric field, \bar{E} , at breakdown which most likely occurs at the location of the standing-wave maximum in the film.¹³ The rms field in a thin film is computed by using the relation

$$\bar{E} = (377 I_0)^{1/2} \left| \frac{E}{E_0^+} \right|_p, \quad (8)$$

where 377 Ω is the free-space impedance, I_0 is the incident peak intensity (GW/cm^2), and $|E/E_0^+|_p$ is the peak electric field normalized to the incident field.

Figure 47 shows the spectral dependence of the threshold electric field in MV/cm. For each material the rms field increases from 1.064 to 0.532 μm , then falls from 0.532 to 0.355 μm .

The increase of the rms field from the near infrared through the visible region would be unexpected if absorption processes initiated laser damage. However, for an electron avalanche, the qualitative expression for the frequency dependence of the breakdown field is¹⁴

$$\bar{E}(\omega) = (1 + \omega^2 \tau_r^2)^{1/2} E_{dc}, \quad (9)$$

TABLE IV
DAMAGE THRESHOLDS OF SINGLE-LAYER REFRACTORY OXIDE COATINGS

Film Material	Manufacturer	Film Thickness: Quarter Wavelength for the following Wavelength (μm)	Laser Wavelength (μm)	Damage Threshold	
				Peak Energy Density (J/cm^2)	Peak Intensity (GW/cm^2)
TiO_2	A	0.532	0.355	0.14 - 0.26	7.6 - 14.1
	A	0.532	0.532	3.0 - 4.4	134 - 196
	A	0.532	1.064	1.8 - 2.6	56 - 81
	B	0.532	0.532	2.4 - 3.4	107 - 151
	B	1.064	1.064	3.5 - 5.5	110 - 172
ZrO_2	A	0.355	0.355	1.7 - 2.7	92 - 147
	A	0.532	0.532	4.1 - 5.0	182 - 220
	A	1.064	1.064	3.6 - 4.2	113 - 132
	B	0.355	0.355	1.4 - 2.2	76 - 119
	B	0.532	0.532	3.1 - 4.7	138 - 210
HfO_2	U.R.	0.355	0.355	2.1 - 3.0	114 - 163
	U.R.	0.355	0.532	3.0 - 4.2	133 - 187
	U.R.	0.355	1.064	3.6 - 4.2	113 - 131
	U.R.	1.064	0.355	1.5 - 1.6	81 - 87
SiO_2	B	0.532	0.355	2.3 - 3.2	125 - 174
	B	0.532	0.532	3.7 - 4.9	165 - 220
	B	0.532	1.064	5.5 - 6.0	172 - 188
	A	0.532	0.532	6.2 - 7.0	280 - 310

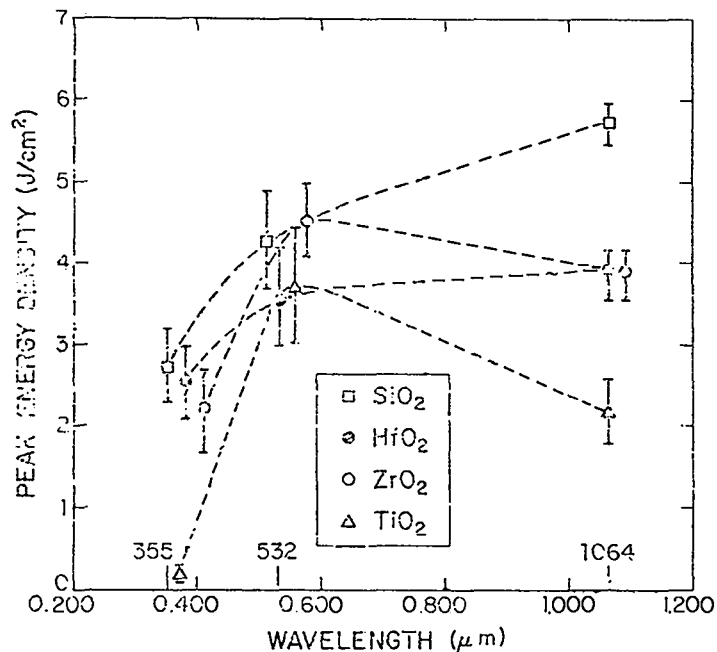


Fig. 45. Threshold energy densities versus wavelength for each of the film materials tested.

where τ_r is a characteristic relaxation time of each material determined principally by phonon collisions. When ω is comparable to $1/\tau_r$, then frequency dispersion should be noticed. This is seen in Fig. 47. For wavelengths longer than $0.532 \mu\text{m}$, it is not now possible to conclude at what wavelength the maxima of the rms electric fields are reached. However, it is apparent that linear and multiphoton absorption are not the dominant processes in the region from 1.064 to $0.532 \mu\text{m}$. The rapid decrease that was measured below $0.532 \mu\text{m}$ does suggest that multiphoton absorption is dominant in the uv region. A comparison of the absorption edge energies of the films with the multiphoton laser energies suggests that resonant absorption by a single photon at $0.355 \mu\text{m}$ is the damaging mechanism in TiO_2 , and that two-photon absorption is very possible at that wavelength for ZrO_2 , HfO_2 , and SiO_2 for these short (~ 17 -ps) pulses.

The threshold fields for 0.532 and $0.355 \mu\text{m}$ plotted in Fig. 47 were measured with shorter laser pulsewidths (~ 21 and ~ 17 ps, respectively) than the nominal 30 ps of the $1.064\text{-}\mu\text{m}$ fundamental wavelength. The possible effect of pulsewidth on the results should also be considered. A $\tau^{-1/4}$ dependence of the threshold electric field has been re-

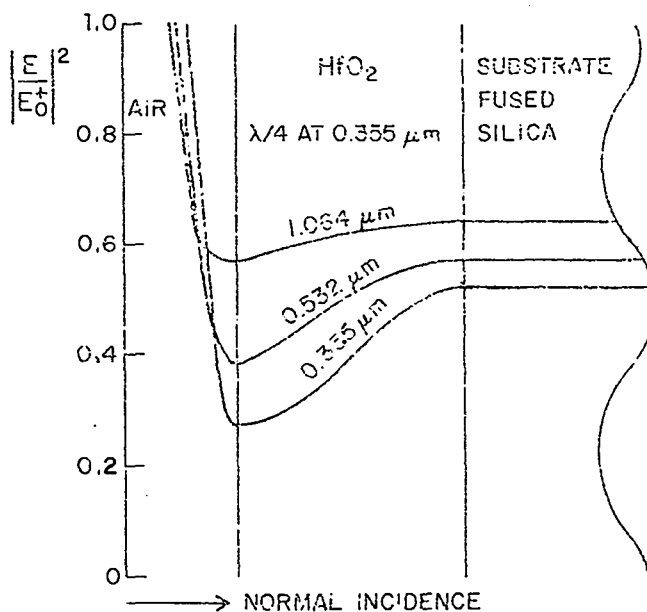


Fig. 46. Standing-wave electric field pattern in a single layer of HfO_2 , $\lambda/4$ thick, at $0.355 \mu\text{m}$, used at three different wavelengths: 0.355 , 0.532 , and $1.064 \mu\text{m}$.

cognized¹⁵ in the data reported by several researchers in crystals and glasses. This dependence is consistent with the avalanche breakdown mechanism, and is the same for metal surfaces.

A pulsewidth effect on the damage threshold of thin films has also been reported. The spark thresholds of a ZrO_2 film measured between 10 and 35 ns at $0.694 \mu\text{m}$ ¹⁶ fit the $\tau^{-1/4}$ dependence, but the lower thresholds for laser-induced scattering, measured simultaneously, showed a much weaker pulsewidth dependence. The thresholds at $0.694 \mu\text{m}$ for several multilayer reflectors¹⁷ also exhibited a pulsewidth dependence roughly comparable to $\tau^{-1/4}$.

To normalize the present results to 30 ps, using a $\tau^{-1/4}$ law, the data in Fig. 47 would be multiplied by 0.95 and 0.87 at 0.532 and $0.355 \mu\text{m}$, respectively. However, the presence of film defects may well override any pulsewidth dependence, especially for subnanosecond pulses. Obviously, further experiments at different pulsewidths are needed to clarify this matter.

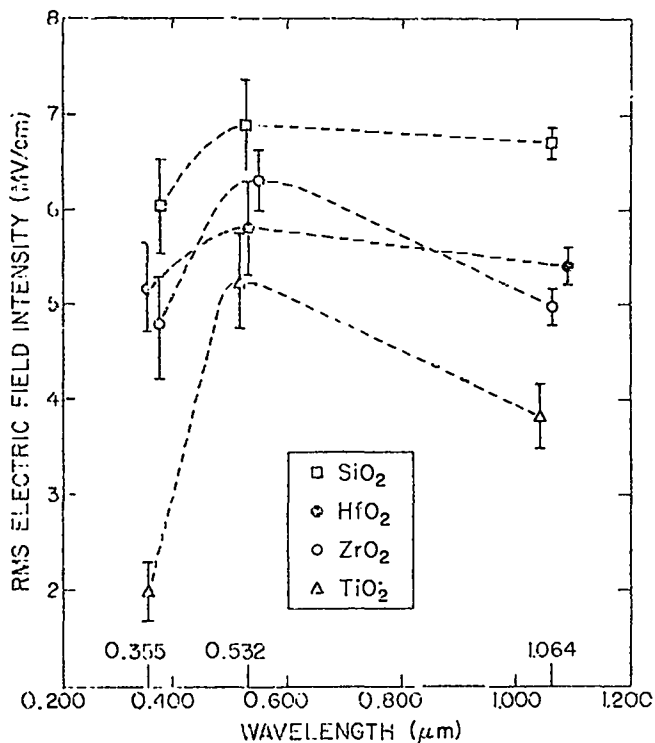


Fig. 47. Threshold electric fields versus wavelength for each of the film materials tested.

REFERENCES

1. A. Gedanken, J. Jortner, B. Raz, and A. Szoke, *J. Comput. Phys.* 57, 3456 (1972).
2. Stanford Research Institute report MP 75-43 (August, 1975).
3. R. E. Drullinger, M. M. Hessel, and E. W. Smith, NBS Monograph 143 (1975).

4. L. A. Schlie, B. D. Guenther, and R. D. Rathge, *Appl. Phys. Lett.* 28, 393 (1976).
5. F. Skoberne, Los Alamos Scientific Laboratory report LA-6245-PR, Sec. I, pp. 39, 40 (July 1976).
6. M. A. Biondi, *Phys. Rev.* 90, 730 (1953).
7. O. P. Judd and J. Y. Wada, *IEEE J. Quantum Elect.* QE-10, 12 (1974).
8. M. Bader, Proc. 2nd Int'l. Heat Pipe Conf., Bologna, Italy (Mar.-Apr. 1976).
9. B. E. Newnam and D. H. Gill, 1976 Symposium on Optical Materials for High-Power Lasers, Boulder, CO (July 1976).
10. P. Baumeister, Univ. of Rochester, private communication (1976).
11. B. E. Newnam, D. H. Gill, and G. E. Faulkner, *Laser Induced Damage in Optical Materials: 1975*, NBS Spec. Pub. 435, 254 (1975).
12. N. L. Boling, M. D. Crisp, and G. Dube, *Appl. Opt.* 12, 650 (1973).
13. J. H. Apfel, J. S. Matteucci, B. E. Newnam, and D. H. Gill, 1976 Symposium on Optical Materials for High-Power Lasers, Boulder, CO (July 1976).
14. N. Bloembergen, *IEEE J. Quantum Elect.* QE-10, 375 (1974).
15. J. R. Bettis, R. A. House, and A. H. Guenther, 1976 Symposium on Optical Materials for High-Power Lasers, Boulder, CO (July 1976).
16. B. E. Newnam and L. G. DeShazer, *Laser Induced Damage in Optical Materials: 1972*, NBS Spec. Pub. 372, 123 (1972).
17. E. S. Bliss and D. Milam, *Laser Induced Damage in Optical Materials: 1972*, NBS Spec. Pub. 372, 108 (1972).

III. LASER FUSION -- THEORY, EXPERIMENTS, AND TARGET DESIGN *

In an integrated program of theory, target experiments, and target design, we are establishing a fundamental understanding of laser-target interactions, particularly of the relevant plasma physics and hydrodynamics. Both the experimental and the theoretical efforts have concentrated on studying the wavelength-dependence of laser-plasma interactions. The close coupling of theory and experiment has made it possible to eliminate theories that are not supported by experiment. In general, basic studies of laser-plasma interactions have shown that the design difficulties associated with long wavelengths are less severe than believed earlier, and that breakeven target designs are attainable even in the presence of a hot-electron spectrum. These results have given us new confidence that significant yield can be obtained from more efficient, less expensive CO₂ lasers.

TARGET EXPERIMENTS AT 1.06 AND 10.6 μm

Introduction

Much of our recent effort was spent in preparing experiments and diagnostics for the two-beam CO₂ laser system (TBS), scheduled to begin in October 1976. Experiments conducted on our Nd:glass and single-beam CO₂ system measured the hydrodynamic velocity of the surface of critical density, determined the origin of K_α radiation in layered targets, and studied the hot-electron current ejected from laser-produced plasmas.

Laser Transmission Experiments -- Velocity of Critical-Density Surface

We used our Nd:glass and single-beam CO₂ systems, at 1.06 and 10.6 μm, respectively, to irradiate thin foils of various materials at peak intensities of ~10¹⁵ W/cm². The transmission of laser light through the foil was measured as a function of foil thickness. These data were used to estimate the hydrodynamic velocities of the critical-density surfaces. The estimates will be valuable in analyzing the behavior of structured targets during irradiation by a laser pulse. We found that the velocities were wavelength-independent.

The transmission data for both wavelengths and for several pulse lengths obeyed the formula

$$T \approx \exp - \left(\frac{d}{1.5 \pm 0.5} \frac{\lambda^2}{\tau_L} \right) \quad (1)$$

in the range of transmissions 0.04 < T < 0.95, where d is the initial foil thickness in micro-

meters, λ is the incident wavelength in micrometers, and τ_L is the laser pulse width (FWHM) in nanoseconds.

From this empirical formula, we see that the foil thickness required for a given transmission is

$$d \approx - \frac{1.5 \tau_L}{\lambda^2} \ln T \quad (2)$$

A value may be obtained for the maximum velocity of the critical-density surface by considering the following one-dimensional model: The initial foil is assumed to be a plasma with a rectangular spatial electron profile at density n_{sol}. This profile extends initially from x = -d/2 to x = +d/2. When the laser light irradiates the foil, at time t=0, the plasma begins to expand, maintaining a rectangular shape. The laser light is either reflected or absorbed until the expansion lowers the electron density to the laser critical density. From this time on, we assume that the foil transmits the incident laser light.

At t_c, the time at which transmission begins, the extent of the critical-density plasma is

$$x_c = \frac{d}{2} \left(\frac{n_{sol}}{n_{cr}} \right) = \frac{d}{2} \left(\frac{n_{sol}}{n_0} \right) \lambda^2, \quad (3)$$

where n₀ = 10²¹/cm³. From the transmission data [Eqs. (2) and (3)], we obtain

$$x_c = \frac{d}{2} \left(\frac{n_{sol}}{n_0} \right) \lambda^2 = - 0.75 \left(\frac{n_{sol}}{n_0} \right) \tau_L \ln T. \quad (4)$$

Thus, for a given transmission and pulse length, the extent of the critical-density surface is independent of incident wavelength. This model gives the maximum extent of the critical-density surface at time t_c for all density profiles that monotonically decrease from the center of the original foil. If the expansion were not one-dimensional, the extent of x_c would again be less than that given in Eq. (3). For two- or three-dimensional plasma expansion, x_c would no longer be independent of wavelength; it would decrease with increasing wavelength.

For the model discussed above, we may find the average velocity of the critical-density surface as follows:

$$\bar{u}_{cr} \text{ (cm/s)} \cong \frac{x_c}{t_c} = 7.5 \times 10^4 \left(\frac{n_{sol}}{n_0} \right) \frac{\tau_L}{t_c} \ln T. \quad (5)$$

For any laser temporal pulse shape, the transmission is a function of t_c/τ_L only.

We assume a Gaussian temporal shape for the incident pulse, with FWHM equal to τ_L , centered at time $t = \tau_L$ and truncated at times $t=0$ and $t=2\tau_L$. Table V gives values of \bar{u}_{cr} for this pulse shape at various times, assuming $n_{sol} = 10^{23}/\text{cm}^3$. We see that, for this case, the velocity of the critical-density surface is less than 10^7 cm/s during most of the laser pulse, and this velocity is independent of laser wavelength. Because this model yields the maximum extent and maximum velocity of the critical-density surface, we expect that experiments, which do not have such idealized density profiles, will show somewhat lower velocities (and extents).

TABLE V

AVERAGE HYDRODYNAMIC VELOCITIES OF CRITICAL-DENSITY SURFACE FOR A ONE-DIMENSIONAL RECTANGULAR EXPANSION OF A THIN FOIL

t_c/τ_L	Transmission	\bar{u}_{cr} (10^7 cm/s)
0.2	0.98	0.88×10^7 cm/s
0.4	0.93	0.14
0.8	0.68	0.36
1.0	0.5	0.52
1.2	0.32	0.72
1.6	0.007	1.24
1.8	0.021	1.61

X-Ray Measurements in Experiments with Layered Targets

We performed some x-ray measurements to determine the source of K_α radiation and the penetration depth of 10.6- μm light (burnthrough thickness) on targets of aluminum film of different thickness deposited on silica (SiO_2). These experiments were conducted with 10- μm laser pulses of up to 14 J focused onto flat targets, at a peak irradiance of 4×10^{13} W/cm². The x-ray intensities of aluminum and silicon lines were recorded with a flat TAP-crystal spectrograph.

We conducted these experiments mainly to determine the source of inner-shell excitation that results in K_α radiation. Silicon K_α radiation from the silica substrate was observed through aluminum layers as thick as 0.5 μm , whereas "helium-like" lines of silicon were completely absent with an aluminum coating as thin as 0.05 μm . Further, the aluminum K_α radiation increased markedly relative to the "helium-like" lines of aluminum as the thickness of the overcoating was increased. These results support the belief that the K_α radiation is generated by electron impact in the surrounding cold material and not in the plasma. Because of the high absorption of 1.74-keV silicon x rays by the aluminum, we were unable to estimate the electron energy from these data.

The laser burnthrough thickness was determined from the intensity of the silicon line at 1.74 keV ($1s\ 2p-1s^2$), normalized to the laser energy for coating thicknesses of 59, 121, and 198 Å. These data on a semilogarithmic plot predict the 1/e intensity point at an aluminum layer thickness of 96 Å. This thickness is consistent with the transmission of laser light through foils proportional to

$$\exp\left(-\frac{d \lambda^2}{ct}\right), \quad (6)$$

as discussed earlier.

Measurement of Electron Current from a Laser Plasma

The total number of high-energy electrons ejected from a laser-produced plasma was measured on a flat brass disk target. The target was connected directly to the center conductor of a coaxial cable leading to a fast oscilloscope. During

the CO₂ laser irradiation of the target (at $\sim 5 \times 10^{13}$ W/cm²), we observed a net flow of 4×10^{12} electrons. The total number of ions emitted from the target at this level of laser irradiance had been measured previously¹ as 3×10^{14} . Charge-neutralizing cold electrons flow away from the target with these ions. The total number of electrons ejected from the target was $\sim 1\%$ of the number of ions. These electrons are presumed highly energetic to be able to escape the high electric field produced by the charge inequality in the plasma created by the loss of electrons. Our result is in reasonable agreement with the observed electron energy spectrum and with the estimated number of electrons above 75 keV.² The number of electrons flowing from the back side of a thin plastic target can also be measured in this experimental setup.³

THEORETICAL STUDIES OF LASER FUSION

Introduction

We have progressed in our efforts to define the hot-electron generation spectrum, obtaining some initial results for simulations at high intensity with self-consistent density profiles. We have also continued to model the nonlinear saturation of the sharp plasma-laser interface instability, finding some polarization dependencies. In studies of the magnetic fields associated with resonant absorption we found good agreement between our theoretical results and our simulations.

Scaling of Hot-Electron Spectrum with Wavelength

The sharp density gradients arising from the balance between the laser ponderomotive force and the plasma pressure has been shown⁴ to reduce the energy of hot electrons produced by resonant absorption from the previously estimated high values.⁵ We have continued to study the dependence of hot-electron energy on wavelength, λ_0 , and on cold background electron temperature, T_c . The hot-electron energy has been shown⁴ to scale as

$$T_H \sim eEL, \quad (7)$$

where E is the local maximum in the longitudinal

electric field and L is the interaction scale length. The fact that heating is occurring in a localized electron plasma wave perhaps suggests, even for a sharp gradient, that the length L should scale as the electron Debye length at the critical density (v_e/ω). This then would yield

$$T_H \sim ET_c^{1/2} \lambda_0, \quad (8)$$

or scaling directly as the wavelength and as the square root of the intensity. However, at high intensity this prediction would disagree with wavelength-scaling experiments and with the scaling of hot-electron temperature at $1 \mu\text{m}$.

Although the calculations are still in progress, we have completed three simulations with wavelengths of 1, 2, and $4 \mu\text{m}$ at an incident flux of 10^{16} W/cm², an initial electron temperature of 2.5 keV, and an angle of incidence of 20° with the electric field polarized in the plane of incidence. The density profiles are initialized close to pressure equilibrium to minimize initial transients. The typical equilibrium structure is shown in Fig. 48. Note the sharp rise in density to ten times the critical density in Fig. 48(a), and the localized plasma-wave amplitude in Fig. 48(b). The x component of the electric field is shown in Fig. 48(c), illustrating the conversion of the incident electromagnetic wave to a short-wavelength electrostatic component.

As a simple way of characterizing the hot-electron energy, we define the hot-electron temperature, T_H , as the electron energy above which 50% of the absorbed energy flux is carried. Results for the three different wavelengths are shown in Fig. 49. The dashed curve of $T_H \propto \lambda$ is shown for comparison and appears to be consistent with the observed data. These data points are being carefully checked with better spatial resolution and improved particle statistics. Note that the internal scaling of variables in the two-dimensional simulation code WAVE is such that changing the wavelength by a factor of 2 is completely equivalent to changing the intensity by a factor of 4. Thus, these data also verify the scaling of T_H with

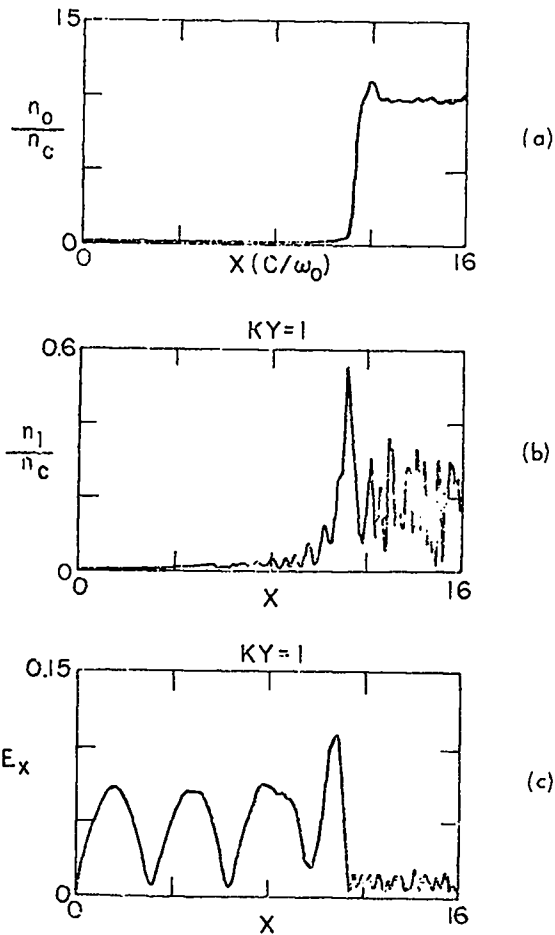


Fig. 48. Simulation at laser wavelength of $1 \mu\text{m}$ and intensity of 10^{16} W/cm^2 with laser electric field polarized in the plane of incidence and wave vector incident at $\theta_0 = 20^\circ$ to the density gradient: (a) the plasma density profile, (b) plasma-wave density fluctuation amplitude as a function of position, and (c) plasma-wave electric field as a function of a position.

the incident intensity. The absorption in all cases exceeds 30%.

The scaling of hot-electron energy with background temperature is shown in Fig. 50 for simulations with 625-eV and 2.5-keV background temperatures. The dashed curve represents the scaling according to $T_H \propto T_C^{1/2}$, which is consistent with these results. By normalizing this scaling to the data points, we would predict for incident intensities of 10^{15} W/cm^2 and a background temperature of 300 eV, a hot-electron energy of 6 keV for a $1\text{-}\mu\text{m}$ wavelength. A scaling of $T_H \propto \lambda$ would predict a hot-

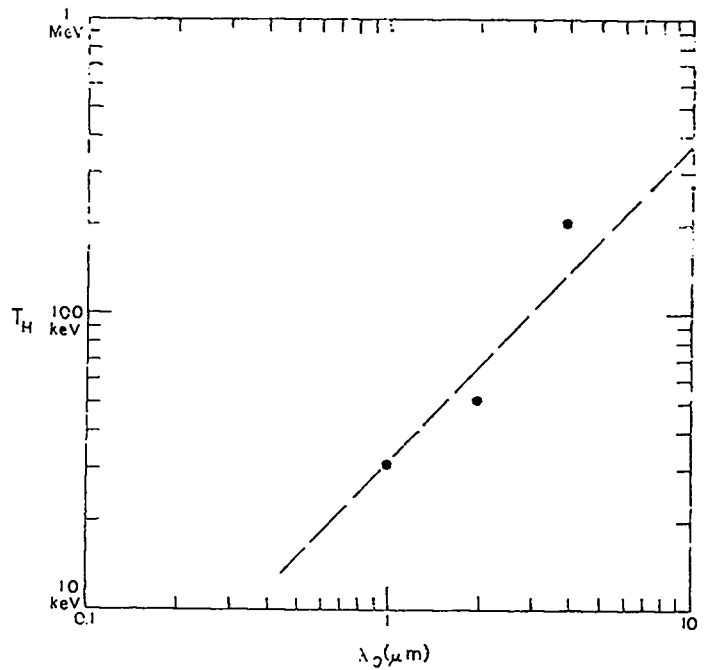


Fig. 49. Hot-electron temperature T_H as a function of laser wavelength for a laser intensity of 10^{16} W/cm^2 and a background temperature of $T_C = 2.5 \text{ keV}$.

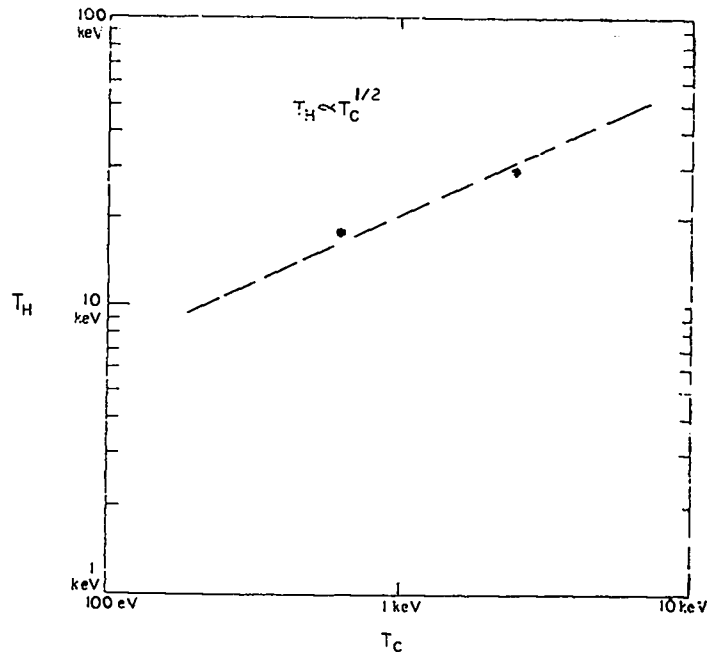


Fig. 50. Hot-electron temperature as a function of a background temperature T_C for a laser intensity of 10^{16} W/cm^2 at a wavelength of $1 \mu\text{m}$.

electron temperature of 60 keV for a 10- μ m wavelength, but this scaling appears to be in disagreement with experimental results. Also, because the 4- μ m simulation encountered some numerical problems, we do not have enough data points to predict the scaling on wavelength and intensity. Within the next three months we hope to obtain more definitive simulation results.

In addition, there are important differences between the experimental conditions and the monochromatic plane-wave approximation made in our simulations. In experiments, the short-focal-length focusing optics (f/l to 2) apparently result in no observable difference between S- and P-polarized light incident on the target with regard to the fast-ion energy and absorption coefficient.⁶ With such optics, the plane-wave approximation is very poor, and the complicated field patterns at the focus may always result in resonance absorption, perhaps just due to the nonplanarity of the equilibrium. The modification of the above-described equilibrium due to a focused laser beam is not yet well understood, and further calculations are needed. We could make better comparisons of experiment with this plane-wave theory if focusing optics of much higher f-number were employed in the experiments.

Stability of Sharp Laser-Plasma Interface

We have continued our studies aimed at understanding the scaling of the instability of the sharp laser-plasma interface and its long-term nonlinear behavior. In the regime where $v_0/v_e = (eE/m\omega v_e)$, the linear stability theory has been analyzed by Fourier-transforming the coupled fluid equations and wave equations both in the transverse spatial dimension and in time, and solving for the eigenfunctions along the density gradient which give rise to unstable temporal (complex ω) growth. We find that the growth appears to scale as the electric field, and find growth rates that are within a factor of 2 of those observed in two-dimensional WAVE simulations. The maximum growth occurs for $k_y c/\omega = 0.5$ to 1.0, with only slightly smaller growth rates for longer wavelengths. For polarization in the plane of incidence, the growth rates appear to be significantly slower; so slow, in fact, that the instability has not been observed

for this polarization in two-dimensional simulations.

The saturation of the growth of surface ripples due to ion heating has already been reported.⁴ At still later times in the nonlinear development of this instability, isolated bubbles of radiation surrounded by overdense plasma seem to form, as illustrated in the density contour plot in Fig. 51 for $v_0/c = 0.5$, $v_e/c = 0.2$, $m_i/m_e = 25$, and $T_e/T_i = 400$. The scattered radiation remains very high, and the bubbles appear to dissipate by trapping the ions and adiabatically compressing the electrons. However, the dissipation time is probably abnormally long, because no electric-field component exists along the local density gradients in this spatial geometry. Consequently, dissipation by resonance absorption, which is much faster, cannot occur.

We have also performed a simulation with polarization at 45° to the plane of the computation. In this case the ripples generated by the component of field out of the plane give rise to resonance absorption of the component in the plane. Thus, even for normal incidence, we obtain absorption as high as 20%. The ultimate nonlinear state of the

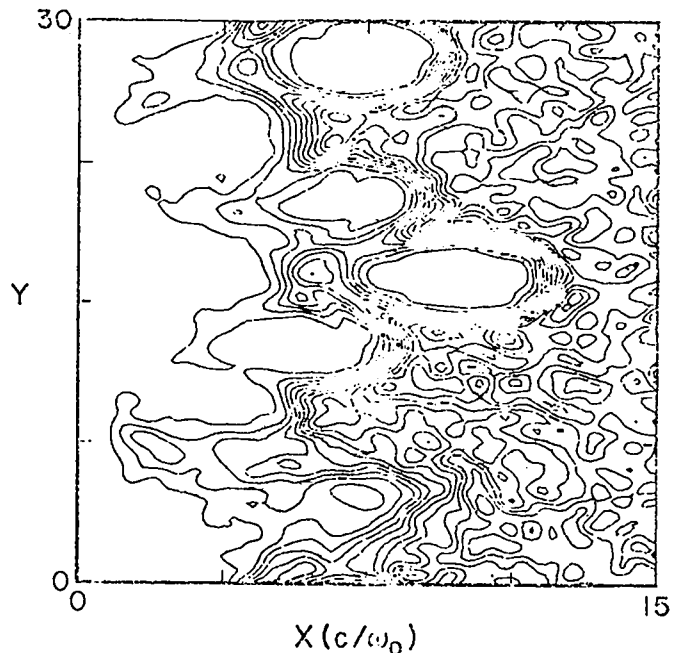


Fig. 51. Ion density contours in x-y space.

ripples in this geometry is being investigated. We suspect that bubble formation will be much less severe, due to the enhanced resonance dissipation.

All our results suggest that a three-dimensional calculation of the laser-plasma interface may be required to determine the nonlinear behavior correctly. This is certainly true for linearly polarized laser pulses.

Self-Generated Magnetic Fields

Computer calculations and experiments suggest that megagauss quasi-dc magnetic fields are generated by the absorption of intense laser light in laser-fusion plasmas.⁷ The original work on this subject concentrated on thermoelectric sources for the magnetic field. Another mechanism stems from the momentum transferred to the plasma due to the absorption of the incident light. In the case of absorption due to linear conversion of light polarized in the plane of incidence, the mechanism of absorption is collisionless for the regime of interest in laser fusion. Therefore, to understand the low-frequency currents generated by the momentum transfer to the plasma, one must employ a self-consistent collisionless kinetic theory to properly account for the electron particle stress resulting from the radiation field. We have developed such a theory to describe the highly inhomogeneous distribution function in the region of the resonant fields.⁸ This theory has been applied to the B-field generation problem to show that saturation of the growth of B occurs when

$$\frac{\partial}{\partial x} (T_{xy}^e + T_{xy}^{em}) = 0, \quad (9)$$

where T^e is the electron stress tensor and T^{em} is the familiar electromagnetic stress tensor.

In earlier calculations⁹ of \dot{B} , only the "quiver" contribution to T^e was included, with the result that it was not clear how $\dot{B} = 0$ was achieved. On the other hand, the above condition is satisfied exactly by the steady-state high-frequency fields E_H . Thus, the growth of B saturates simultaneously with the E_H fields reaching their steady-state values at least to within a particle transit time l/v , where l is a measure of the

spatial scale of the E_H . We should therefore expect

$$\dot{B}/B = (v_e/ck_0L)^{2/3} \omega_0, \quad (10)$$

when plasma-wave convection out of the critical region is the dominant absorption mechanism. This scaling is confirmed by our simulation results. Therefore, the time scale associated with the growth of B is easy to calculate once the growth rate of E_H is known. However, the determination of the final steady-state value of B requires that the quasi-dc current generated in the plasma be known. We have obtained the low-frequency distribution function F_L , giving $\delta J_{yL} = -e \int d^3v v_y F_L$. The term δJ_{yL} , along with the beat current $-e(n_H u_{Hy})$, where n_H is the high-frequency density response and u_{Hy} is the oscillating velocity, gives the total current source for the magnetic field. The resulting expression for the saturated value of B, valid near the critical density, is

$$B(x) = \omega_p^2/\omega^2 (E_x u_{Hy})/c. \quad (11)$$

This expression agrees in structure extremely well with the two-dimensional simulations, and agrees in magnitude to within 30%.

Relationship Between Suprathermal Electron Temperature and Number Using Pair Production

A recent study has shown that the detection of 511-keV photons may provide a simple and direct method for relating the total number of suprathermal electrons in a laser-heated plasma to the temperature of the suprathermal electrons. This method clearly differentiates between the thermal and suprathermal electron populations (in contrast to x-ray methods). Calculations for past CO₂ experiments indicate that between 2×10^2 and 2×10^7 511-keV photons are produced when 10^{20} to 10^{25} suprathermal electrons are generated in a laser-heated plasma. This quantity of photons is well within the detection capabilities of NaI detectors, and it therefore appears that the use of such de-

tectors for measuring suprathemal electron properties is feasible.

The mechanism for the production of these 511-keV photons is as follows. First, collisions between suprathemal electrons and thermal electrons produce photons with energies close to that of the suprathemal electrons; second, the high-energy photons have some probability of undergoing pair production; and finally, the positrons produced by pair production thermalize and annihilate with background electrons to produce 511-keV photons.

A detailed calculation of the chain process described above shows that the number of 511-keV photons, N_p , is related to the number of suprathemal electrons, N_s , and to the suprathemal electron temperature, T_s , by

$$\frac{N_p}{N_s} \propto \left(\frac{T_s}{2mc^2} \right)^5 e^{-2mc^2/T_s}, \quad (12)$$

when $T_s \ll 2mc^2$.

This result suggests that measurement of the 511-keV photons emitted in the experiments referred to above provides a simple connection between the number of suprathemal electrons and their temperature. Furthermore, the derivation of this result makes it clear that only the suprathemal population contributes to the production of 511-keV photons; thus, a clear and natural distinction arises between the thermal and suprathemal populations. The most striking feature of the above result is the pronounced dependence on T_s . Indeed, knowing N_p/N_s to within only a factor of 10 puts very severe restrictions on the uncertainty in T_s . This observation naturally suggests that the most important application of Eq. (12) is in determining T_s from measured values of N_p and N_s .

TARGET DESIGN

Introduction

Although most of our target design work is classified, we can mention some of our developmental efforts. The codes being used and being improved are LASNEX, a two-dimensional Lagrangian code acquired

from Lawrence Livermore Laboratory; MCRAD, a LASL-developed two-dimensional Lagrangian code; and CERES, a LASL-developed one-dimensional Lagrangian code.

We have made our first substantive improvement to the LASNEX code obtained from Lawrence Livermore Laboratory by including the ponderomotive force from the laser electromagnetic field. We also continued our development of LASL's MCRAD code for use in laser fusion.

Code Development

As explained in the previous progress report (LA-6510-PR), the scale length for laser light absorption is critical to the question of wavelength scaling; we also pointed out that the ponderomotive force is an important, neglected factor in determining the plasma density gradient in the region of the critical density, and, hence, on wavelength scaling. We have therefore incorporated the ponderomotive force into LASNEX. Attempts to use an approximate, easy-to-code form for the ponderomotive force were unsuccessful, because of serious errors. Thus, we coded the exact force

$$F = - \left(\frac{\omega_p}{\omega} \right)^2 \nabla \left(\frac{E^2}{8\pi} \right). \quad (13)$$

The actual force on the target core will be greater than the free-space ponderomotive force, as can be understood from the following argument.

The dielectric enhancement in E causes this ponderomotive force to act in the outward direction on the outer material and inward on the inner material. The net momentum transfer is equal to the free-space values, both for the reflected and the absorbed light. But, because of this force-direction reversal, the actual force on the inner material is greater than the free-space value.

We incorporated modifications to account for the group velocity in computing geometric path lengths. We also verified that LASNEX already considered the proper dielectric enhancement in the inverse-bremsstrahlung absorption coefficients.

Our latest improvements to MCRAD included a generalization to handle burn with arbitrary deuterium and tritium fractions at various impurity levels. We also simplified the definitions of

other than axial symmetries. The treatment of conduction bremsstrahlung and inverse bremsstrahlung under conditions of partial ionization has been improved. All these modifications are of importance to both target design and to the interpretation of current experiments.

REFERENCES

1. A. W. Ehler, J. Appl. Phys. 46, 2464 (1975).
2. D. V. Giovanielli, J. F. Kephart, and A. H. Williams, J. Appl. Phys. 47, 2907 (1976).
3. G. H. McCall, LASL, private communication.
4. E. Stark, Los Alamos Scientific Laboratory report, LA-6510-PR (1976).
5. D. W. Forslund, J. M. Kindel, K. Lee, E. L. Lindman, and R. L. Morse, Phys. Rev. A11, 679 (1975).
6. D. Giovanielli, LASL, private communication.
7. J. A. Stamper, K. Papadopoulos, S. O. Dean, E. A. McClean, and J. M. Dawson, Phys. Rev. Lett. 26, 1012 (1972).
8. B. Bezzerides and D. F. DuBois, Phys. Rev. Lett. 34, 1381 (1975).
9. J. J. Thomson, C. E. Max, and K. Estabrook, Phys. Rev. Lett. 35, 663 (1975).

IV. LASER-FUSION TARGET FABRICATION



Our pellet fabrication effort, supported by extensive theoretical investigations, supplies the thermonuclear fuel in packaged form suitable for laser-driven compressional heating experiments. These targets range from simple deuterated-tritiated plastic films to frozen DT pellets to complex DT gas-filled hollow microballoons, mounted on ultrathin supports and coated with various metals and/or plastics. Numerous quality control and nondestructive testing techniques for characterizing the finished pellets are being developed.

INTRODUCTION

In our target fabrication effort, we are developing techniques and methods to fabricate spherical targets containing DT fuel in a variety of chemical and physical forms. High-pressure DT gas has been used extensively as the fuel because it can be conveniently packaged in glass or metal microballoons for use as laser fusion targets. However, the designers and experimentalists would prefer a higher density of DT fuel than can be obtained conveniently in gaseous form. In addition, significantly better yields are predicted if the fuel can be formed as a high-density shell surrounding either a vacuum or a low-pressure spherical core because it is then unnecessary to work against the high pressure of the inner fuel core during the compression of the spherical fuel shell. These considerations have led to our development of methods to condense layers of cryogenic DT, either liquid or solid, on the inside surfaces of microballoons. In addition, we are developing techniques to prepare room-temperature solids containing fuel atoms at high density (e.g., polyethylene, lithium hydride, and ammonia borane, in each of which the hydrogen has been replaced by an equiatomic mixture of deuterium and tritium) and to form these into microspheres and/or microballoons. The non-fuel atoms in these room-temperature solids (carbon, lithium, nitrogen, and boron) must also be compressed and heated to fusion conditions along with the deuterium and the tritium, but because they do not participate in the fusion reaction, they act as diluents of the fuel. As a result, targets fueled with these room-temperature solids are not expected to perform as well as those with cryogenic DT fuel shells. However, the fuels that are solid at room temperature are considerably eas-

ier to work with both in target fabrication and in laser-target interaction experiments, and they also enlarge the parameter space available for exploration in our interaction experiments.

Along with the development of techniques to fabricate the fuel pellets, we also are developing methods to apply a wide variety of coatings to the fuel pellet and to support the pellets for irradiation by the laser beam, using thin plastic films or glass fibers, so as to introduce a minimum of extraneous material into the system. Finally, we are continuously developing techniques to select, characterize, and measure the various pieces of the target both prior to and after assembly.

HIGH-PRESSURE DT GAS-FILLED TARGETS

General

We have continued the development of techniques and methods to fabricate hollow, multilayered spherical targets to be filled with high-pressure DT fuel gas. These generally consist of a high-Z, high-density, metal pusher shell overcoated with a low-Z, low-density absorber-ablator layer. This outer layer absorbs energy from the incident laser, heats, vaporizes, and streams away from the pusher shell causing the pusher shell to implode via the rocket reaction forces. The pusher shell can be deposited onto a nonremovable mandrel (e.g., a glass or metal microballoon), but improved performance might be obtained if the pusher shell is fabricated directly as a freestanding metal microballoon. In either case, high-strength pusher shells are desired so that a high DT pressure can be used, minimizing the additional compression required to attain a fusion burn.

Nonremovable Mandrels

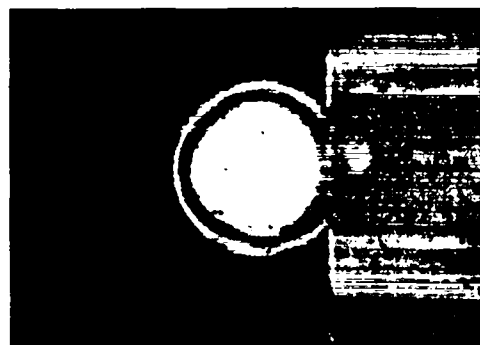
Many of our current targets use bare glass microballoons as pusher shells, filled with high-pressure DT gas to serve as the fuel. Therefore, we continued our development of methods for quality selection and characterization of these bare glass microballoons. Many of these techniques should also be applicable to metal microballoon targets and should be useful in selecting and characterizing microballoons for use as mandrels for structured, multilayered targets.

Measurement of Microballoons by Interferometry

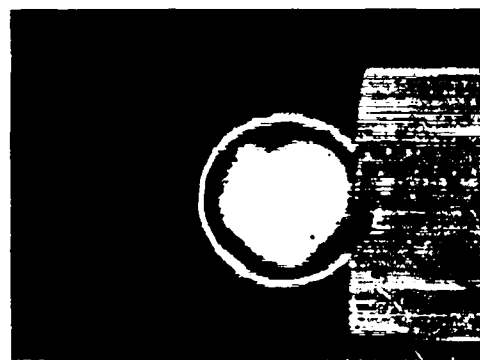
We continued our development of optical interferometry techniques for quality selection and wall-thickness measurement of glass microballoons (GMBs). The GMBs are selected for quality by observing the circularity of the interference fringes and their concentricity with the outside surface of the GMB. For a complete assessment of quality, the GMBs must be viewed in several orientations. In our last progress report,¹ we described a tilting microscope stage that was developed to facilitate this multiple-orientation examination. For extremely critical work, we have developed a new device that allows interferometric examination of the entire surface of a GMB. This apparatus consists essentially of two horizontal vacuum chucks, each rotatable about its own axis, arranged at right angles to each other and located so that the GMB can be transferred from one chuck to the other. A sequence of photomicrographs of a defective GMB that appears to be of high quality in one orientation is shown in Fig. 52 to illustrate the utility of this device; the ends of the vacuum chucks are also visible.

Measurement of Microballoons by Radiography-In addition to our work with optical interferometry, we have continued to develop x-ray microradiography for measuring and characterizing opaque microballoons. Our goal is a rapid and easy-to-use technique that has a resolution of at least $0.05 \mu\text{m}$ for detecting nonconcentric wall-thickness nonuniformities. Glass microballoons are being used in this development work so that we are able to measure nonuniformities also by optical interferometry.

A gold-on-Mylar x-ray resolution target has been obtained, having lines with a width and separation of $0.4 \mu\text{m}$. Microradiographs of this target



(a)



(b)



(c)

Fig. 52. Several views of a single glass microballoon (GMB) in various orientations in the Jamin-Lebedev Interferometer. (a) Orientation in which GMB appears to be of good quality. (b) Rotated 90° from (a); defect apparent. (c) Transferred to second vacuum chuck; quality appears to be intermediate between (a) and (b).

have demonstrated that our geometric resolution is better than $0.4 \mu\text{m}$ for objects $150 \mu\text{m}$ or less above the film plane. Another type of target made from $0.25\text{-}\mu\text{m}$ -diam platinum:rhodium (90:10) wire is now being evaluated. In addition, we hope to obtain a line pair-type resolution target with line-pair dimensions ranging from ~ 1.0 to as small as $0.1 \mu\text{m}$.

We are continuing our development of photometric techniques of obtaining wall thickness non-uniformity and average wall thickness data from the microradiographs, and we are evaluating both our image-analysis system that uses a TV vidicon as the primary sensor and a more conventional scanning microdensitometer. Calculations based on the response of the Kodak HRP glass film plates that we use for our microradiography indicate that monochromatic x rays of $\sim 3 \text{ keV}$ would provide optimum images of glass microballoons if we examine optical density variations on the circumference of the microballoon with our TV image-analysis system to determine wall thickness nonuniformities. However, if we examine the isodensity contours near the center of the microballoon to determine wall thickness variations, or to measure average wall thickness at the center of the radiograph, x rays of 900 eV are optimal. These optimal energies are a function of the atomic number of the microballoon wall material.

As noted in our last progress report,¹ our TV image-analysis system, operating in its present mode, is 50 to 67% less sensitive to wall thickness variations than a scanning microdensitometer (as reported by KMS Fusion).² In an attempt to verify this difference and to understand its origin, we have obtained scanning microdensitometer data over the entire areas of radiographs of two glass microballoons (one good and one bad) and then used a digital computer to generate three-dimensional output data similar to those obtained from our vidicon image-analysis system. Around the circumference of the images (corresponding to the wall at the equator of the GMB), the microdensitometer output variations were two to three times larger than those from our vidicon system. We are now investigating several possible modifications of the vidicon system in an attempt to increase its sensitivity.

For the computer-analyzed microdensitometer data, we also found that several calculated parameters are sensitive indicators of microballoon quality, namely, the calculated image radius and the height of the optical transmission peak. A computer-generated plot of microdensitometer data for the good GMB is shown in Fig. 53, with x and y being the radiograph position coordinates and z the optical transmission of the image. The general crater shape is clearly evident. The computer program calculates the centroid of the approximately doughnut-shaped area defined by all the points in the scan that have a transmission one standard deviation above the average transmission of the scanned area. This calculated center is plotted on a normal view of the images of the good and bad GMBs in Fig. 54(a) and 54(b), respectively. The calculated center lies near the geometric center of the image for the good GMB and is obviously displaced from the geometric center for the bad GMB. (Note that in the actual computer output the images are circular; the pictures in Figs. 54(a) and 54(b) were distorted in the reproduction process from TV screen to film.)

Two other techniques of analyzing the data are shown in Figs. 55 and 56, where data for the good and bad GMBs are again compared. In Fig. 55 we plot the apparent radius, calculated as the distance between the center of mass, as computed above, and the maximum in transmission around the image circumference. In Fig. 56 we plot maximum transmission peak height around the circumference of the GMBs. In both

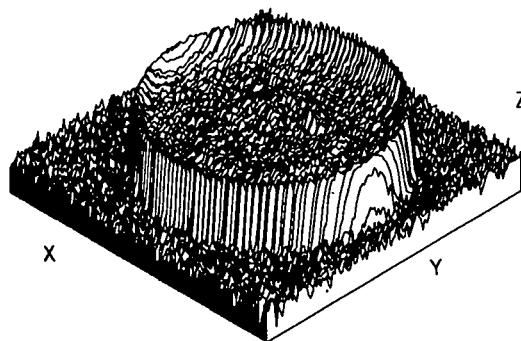
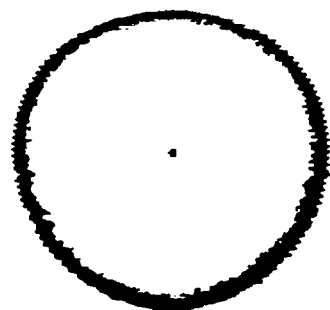
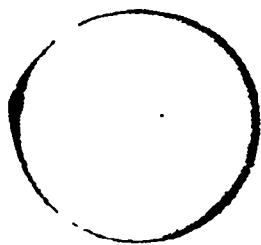


Fig. 53. Three-dimensional representation of the optical transmission of a microradiograph calculated from data obtained with a scanning microdensitometer.



(a)



(b)

Fig. 54. Calculated centers of mass of radiographs of glass microballoons plotted on a computer-generated reconstruction of the radiograph. (a) High-quality GMB; center of mass near geometric center of image. (b) Defective GMB; center of mass obviously displaced from center of image.

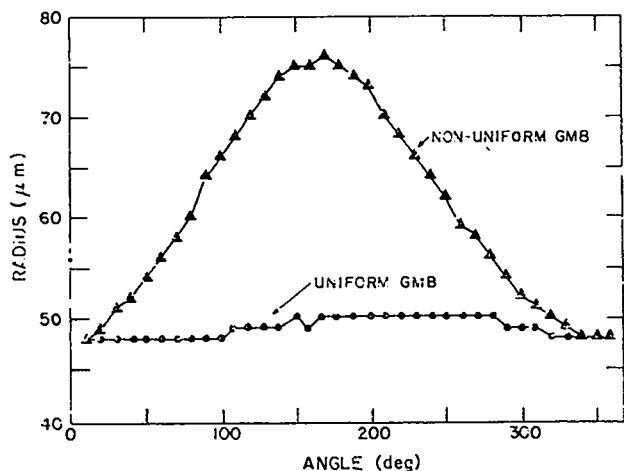


Fig. 55. Radiograph radius calculated from microdensitometer scans of radiographs of good and bad GMBs as a function of position around the circumference of the image. (The radius is taken as the distance between the center of mass and the circle of maximum optical transmission around the circumference of the image.)

cases, the differences between the good and bad GMBs are quite apparent.

Plastic Film Fabrication

We have continued development of our technique for preparing thin films of polyethylene described in the last progress report.¹ The uniformity of the films has been improved by better temperature control of the process. Films can now be prepared easily with less than 10% thickness variation over a 5-cm² area. In addition, we have found that up to 375 K, higher solution temperatures result in somewhat thicker films (20% thicker at 375 K than at 360 K, as used previously). Very thick films (up to several micrometers) can be made by heating the glass slide to be coated. Rapid solvent evaporation from the hot slide results in very thick films, but reproducibility is still rather poor.

Fabrication of Freestanding Plastic Spheres and Cylinders

We have improved our techniques to fabricate freestanding plastic spheres and cylinders by depositing polymerized paraxylene onto metal mandrels (via our glow-discharge polymerization, GDP, process)³ followed by removal of the mandrels by acid etching/dissolution. The spheres are fabricated as

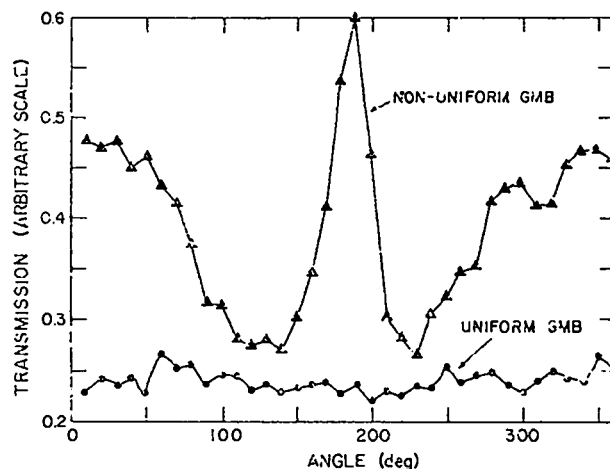


Fig. 56. Optical transmission maxima calculated from microdensitometer scans of radiographs of good and bad GMBs as a function of angular position around the circumference of the image.

hemispherical shells that are subsequently glued together to form a plastic microballoon and usually include a GMB target so that the assembly can be used in evaluating our vacuum-insulation concept for preventing fast-electron preheat.⁴ The cylinders are irradiated on their outside surfaces by two or four laser beams, with diagnostic measurements performed by observing the inside of the cylinders through their open ends to study, e.g., such phenomena as ablation-driven compression.

Our major efforts centered on improving the surface finish of the metal mandrels. (The GDP process results in plastic coatings that accurately replicate defects in the mandrels. Therefore, very smooth mandrels are required if uniform plastic shells are desired.) Some experiments were conducted in which machined copper mandrels were chemically etched and plated with bright copper, followed by electrolytic nickel. Examples of a mandrel surface as machined, as etched, and as plated are shown in Fig. 57. Although the surface finish was improved considerably, the desired surface quality over the entire mandrel surface has not yet been obtained with this technique.

In a parallel approach, we are using some special, micropolished diamond tool bits, along with improved vibration isolation for the lathe, to obtain better machined surface finishes on the mandrels. Here again, considerable improvement was attained, but still higher quality is desired. In a next step, we will combine the improved machining techniques with the electrochemical etching/plating step.

An example of a target fabricated for vacuum-insulation experiments is shown in Fig. 58. The specimen consists of a $\sim 100\text{-}\mu\text{m}$ -diam, DT-gas-filled GMB mounted centrally in a plastic microballoon about $500\ \mu\text{m}$ in diameter having a $3\text{-}\mu\text{m}$ -thick wall. The entire assembly is supported by two small glass fibers stretched across the aperture in our standard molybdenum-foil target holder.

Pusher Shell Deposition

We have continued the development of methods to deposit uniform layers of high-Z metals onto various types of mandrels for use as pusher shells. Our primary objectives are high-strength coatings with useful deuterium-tritium permeability. As de-

scribed previously, we have developed electroless and electroplating techniques for depositing a wide range of metals and alloys onto microsphere substrates.⁵ In addition, we are developing chemical vapor deposition (CVD), physical vapor deposition (PVD), and sputtering to offer us the widest possible choice of metals and alloys for use in coating target microspheres. Emphasis during this reporting period was on CVD and sputtering.

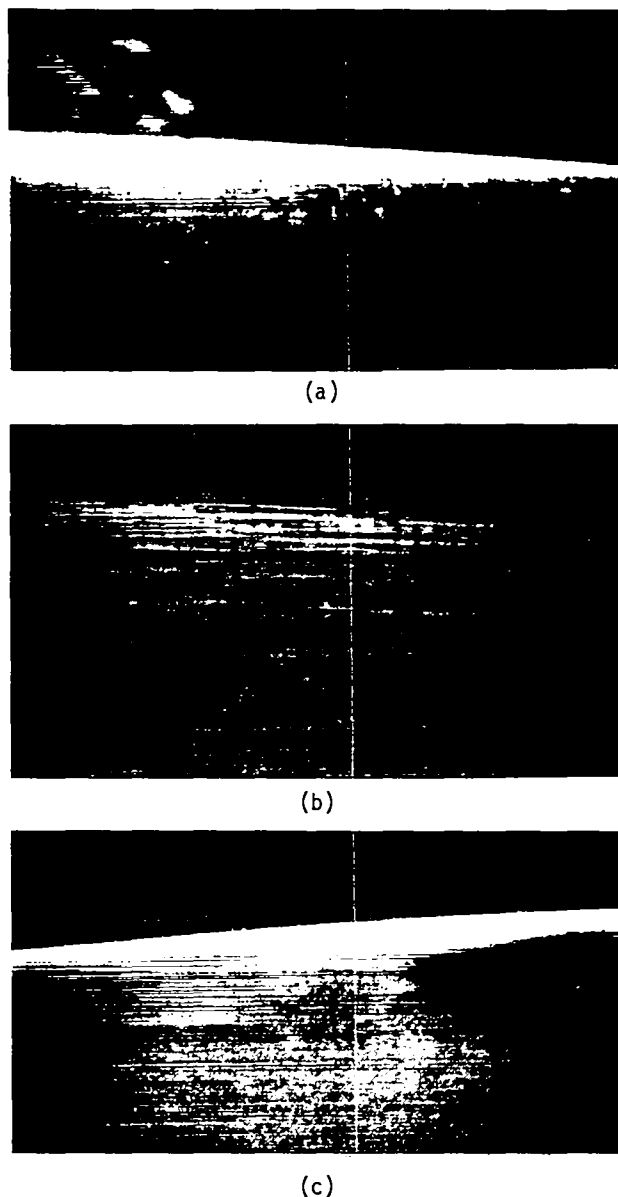


Fig. 57. Scanning-electron micrographs of the surface of a cylindrical mandrel: (a) as-machined (500x); (b) chemically polished, (500x), and (c) chemically polished and electroplated with bright copper and nickel (1500x).

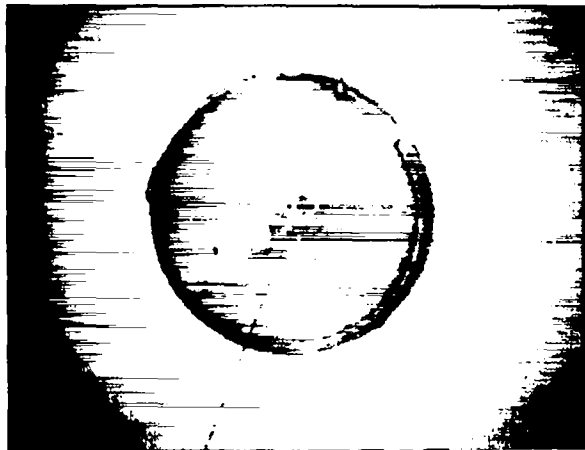


Fig. 58. Multiple-shell target with DT-gas-filled glass microballoon mounted in the center of a larger plastic microballoon.

Chemical Vapor Deposition -- The CVD process involves the chemical or thermal reduction of a metal-containing compound at the surface of a substrate. The method has been useful for coating microsphere substrates in a gas-fluidized-bed coating apparatus, which mixes the substrates well and allows us to apply useful metal coatings to these otherwise difficult-to-handle structures.

Molybdenum from Molybdenum Carbonyl: Very strong tungsten/rhenium alloys have been deposited by CVD.⁶ This result has suggested that molybdenum:rhenium alloys might also form strong CVD coatings, but at a better strength-to-mass ratio because molybdenum has a density half that of tungsten (~10 vs ~20 g/cm³). Therefore, we have been developing techniques to deposit molybdenum and molybdenum:rhenium alloys by CVD techniques.

Initially, we tried to deposit molybdenum metal from molybdenum carbonyl, Mo(CO)₆. However, chemical analyses and x-ray diffraction measurements indicated that the coatings consist of dimolybdenum carbonyl (Mo₂C), regardless of experimental conditions.¹ Because this Mo₂C could also be a useful coating material for laser target applications, we have continued the Mo(CO)₆ work. However, our previous CVD experience with Mo(CO)₆ has shown that our coatings are either cracked because of residual stresses or have rough surfaces because of gas-phase nucleation problems. Because the coatings of laser targets must be both stress-

free and smooth, we have continued coater development and improved our control of process variables. Primary emphasis was placed on reactant and carrier-gas feed-rate control and on improving the action and reproducibility of the gas-fluidized bed.

The situation we face is illustrated in Fig. 59, which plots coating smoothness and stress conditions versus process variables, indicating a narrow range of parameters that will optimize both the stress factor and the surface smoothness. Recent experiments are summarized in Tables VI and VII.

To assist in our judgments of surface smoothness we have established standards for surface morphology, which are shown in Fig. 60. All the standards are CVD Mo₂C deposits. Experiment 2 resulted in the best surfaces obtained so far, and Standard 1 is a scanning electron micrograph (SEM) of an example from this experiment.

The stress factor is more difficult to describe accurately. Peeling resulting from stress buildup during deposition is an obvious phenomenon, and is referred to as a large stress in the 'Stress' column of Table VI. The none, small, and medium terms refer to the size of cracks seen in the metallographic cross sections, but no such cracks have shown up in the SEMs. The cracks seen in the cross sections probably result from shrinkage of the curing epoxy in the metallographic samples at the time of mounting, and a variation in

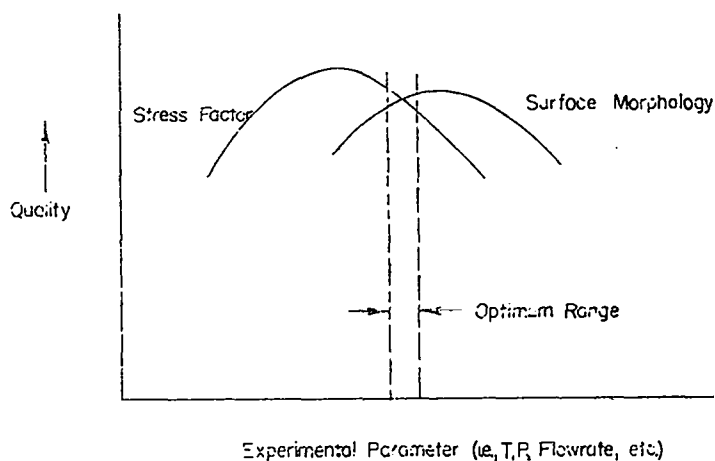
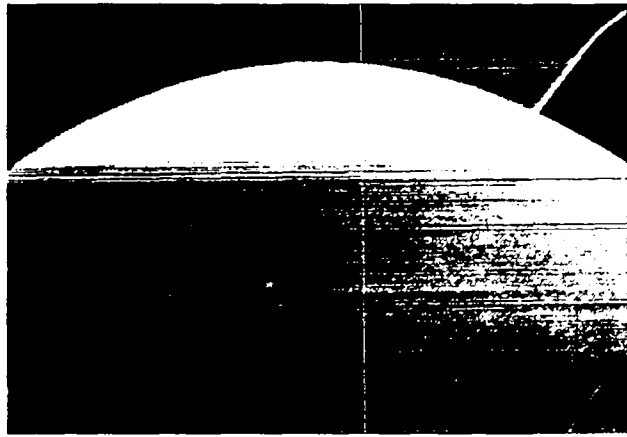
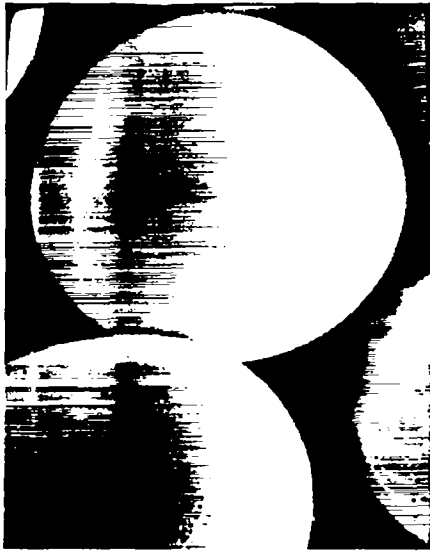


Fig. 59. Schematic of coating-quality parameters versus experimental variables (e.g., temperature, pressure, flow rate) for the chemical-vapor-deposition (CVD) process.



(a)



(b)



(c)

Fig. 60. Standard surfaces used to compare surface quality of CVD coatings. (a) Standard 1 - No. 2, Table VI, 750x; (b) Standard 2 - No. 4, Table VI, 300x; (c) Standard 3 - No. 3 Table VII, 300x. All standards are dimolybdenum carbide coatings deposited by CVD.

the epoxy cure could conceivably change the situation -- all the way from no cracking (none) to rather dominant cracks (medium).

As seen from Tables VI and VII, the better deposits are achieved at 625 K. At 775 K, and at carbonyl partial pressures of ~0.8 torr or higher, gas-phase nucleation occurs. The four experiments performed at 775 K appear to be reasonably consistent. Some inconsistencies with the data at 625 K resulted from experimental fluctuations. The optimum range of coating parameters that will produce stress-free deposits with a near-perfect surface morphology (Experiment 2, Table VI) appears to be very small. This conclusion is supported by the

fact that Experiments 10 through 13 and 15 through 18 were near optimum as far as stress is concerned, but were lacking in surface quality. On the other hand, Experiments 5 through 9 were optimum from the surface-quality point of view but were very highly stressed. Experiments 2, 3, 15, 16, and 19 were optimum from both considerations.

We feel we have demonstrated that Mo_2C shells meeting the tolerance requirements for laser fusion targets can be achieved by CVD. It is now a matter of obtaining reproducibility. Several factors could affect this capability. First, the true temperature and the temperature profile of the fluid bed are not known; the reported temperature is that

TABLE VI
CVD Mo₂C DEPOSITED AT 625 K

No.	Run ^a	Flow Rate ^b (cm ³ /min)	Total Pressure (torr)	Temp of Mo(CO) ₆ (K)	Partial Pressure Mo(CO) ₆ (torr)	Coating			
						Thickness (μm)	Rate (μm/min)	Stress ^c	Surface ^d
1	7-12-76	510	180	315	0.35	10.0	0.005	large	--
2	8-25-76	260	180	325	1.17	3.0	0.0083	small	1
3	8-27-76(A)	510	180	325	1.01	3.0	0.0098	none	1
4	8-27-76(B)	510	180	325	0.95	--	--	small	2
5	7-19-76	510	180	325	0.98	7.0	0.017	large	1
6	7-20-76	510	180	325	0.87	6.9	0.023	large	1
7	7-22-76	510	180	325	0.77	3.9	0.011	medium	1
8	7-22-76(A)	510	180	325	0.77	7.7	0.021	large	1
9	8-24-76	510	180	325	0.95	5.1	0.014	large	1
10	6-16-76(A)	480	180	325	0.81	3.2	0.0086	none	2
11	6-16-76(B)	510	180	325	0.83	5.6	0.0079	none	2
12	6-16-76(C)	440	170	325	--	8.2	0.001	small	2
13	6-16-76(D)	330	150	325	1.13	11.4	0.012	none	2
14	7-14-76	510	180	325	0.85	12.5	0.0086	large	--
15	6-28-76(A)	510	180	335	2.34	3.7	0.031	none	1
16	6-28-76(B)	510	180	335	2.16	6.9	0.023	none	1
17	6-28-76(C)	510	170	335	--	10.4	--	none	2
18	6-28-76(D)	510	160	335	1.60	13.4	0.007	small	2
19	6-24-76(A)	490	180	335	1.93	4.0	0.025	small	1
20	6-24-76(B)	510	180	335	3.68	7.1	0.041	medium	2
21	6-23-76	490	180	335	1.99	4.8	0.027	large	2
22	7-2-76	510	170	345	4.65	4.6	0.081	large	2
23	7-6-76	510	180	355	13.80	3.2	0.083	large	2

^aRuns followed by (A), (B), (C)... are series, in which the deposits are built by interrupted coating runs. The coating apparatus is dismantled and cleaned between runs.

^bFlow rate is based upon standard temperature and pressure conditions.

^cLarge stress refers to runs in which pieces of deposit peeled off the substrates are clearly observed by optical microscope. Medium and small stresses refer to runs in which no loose pieces of shell are seen visually or by SEM, but cracks are observed in the walls of the metallographic cross section.

^dSurface factor is defined in Fig. 60.

TABLE VII
CVD Mo₂C DEPOSITED AT 775 K

No.	Run	Flow Rate ^a (cm ³ /min)	Total Pressure (torr)	Temp of Mo(CO) ₆ (K)	Partial Pressure Mo(CO) ₆ (torr)	Coating			
						Thickness (μm)	Rate (μm/min)	Stress ^b	Surface ^d
1	7-29-76	510	180	305	0.16	2.1	0.0014	none	2
2	8-2-76	510	180	315	0.38	1.8	0.0027	none	2
3 ^c	8-4-76	510	180	325	0.85	14.0	0.012	medium	3
4 ^c	8-10-76	510	180	335	1.77	10.0	0.024	large	3

^aFlow rate is based upon standard temperature and pressure conditions.

^bLarge stress refers to runs in which pieces of deposit peeled off the substrates are clearly observed by optical microscope. Medium and small stresses refer to runs in which no loose pieces of shell are seen visually or by SEM, but cracks are observed in the walls of the metallographic cross section.

^cThese deposits have particles generated by gas-phase nucleation attached to their surfaces (see Fig. 60).

^dSurface factor is defined in Fig. 60.

of the furnace surrounding the chamber. Because the temperature profile of the fluid bed is unknown, we do not know how pronounced the temperature gradient is or to what extent it affects the deposition. Second, although we attempted to maintain a constant dwell time by holding the total pressure and the flow rate of the gas constant, there were deviations from the desired conditions.

To clarify these issues, we intend to determine both the relationship of the true temperature of the fluid bed to the furnace temperature as well as the temperature profile of the fluid bed. We also intend to insert more accurate transducers into the systems and to use strip-chart recorders to monitor the temperature, pressure, and flow rate throughout an experiment. After the system has been temperature-calibrated and the recorders added, we will determine the effect of substrate temperature, total system pressure, and substrate on coating reproducibility by depositing onto glass microballoons rather than Solacels.

Molybdenum Deposition from MoF₆: As discussed previously, we are evaluating CVD of molybdenum via hydrogen reduction of MoF₆ to obtain coatings of molybdenum metal rather than of Mo₂C, as described above.

A new coater was designed, built, and used for these MoF₆ experiments. It consists of an induction-heated graphite coater tube mounted inside a water-cooled stainless steel vessel. A Lexan window on the top of the assembly allows continuous observation of the fluid bed from above. This entire apparatus is now hydrogen-fluoride resistant, and considerable improvement in coatings has resulted. However, we do not yet obtain reproducible results, and surface smoothness has been no better than Class 2 (see Fig. 60). We are continuing our efforts to improve our control of process variables (especially carrier-gas and coating-gas flow rates) and to obtain smoother surfaces.

Sputtering -- We have resumed our development of a technique to coat microspheres by sputtering. This requires some method of agitating and/or bouncing the microspheres so as to coat the entire surface of the microsphere to a uniform thickness. We have therefore mounted an electromechanically vibrated table in our rf sputtering apparatus. (Special shielding and grounding were necessary to

isolate the vibrator from the rf glow discharge.) Initial experiments indicated that the plasma glow discharge alone is sufficient to cause the microspheres to bounce at the start of a run (similar to the behavior observed in our glow-discharge polymerization process that was developed to coat microspheres with polymerized paraxylene).³ However, as the coating thickness increases, additional agitation by the vibratory support is needed to keep the microspheres bouncing.

Initial experiments included the deposition of titanium onto GMB and Solacel substrates and of gold coatings onto GMBs. The titanium coatings were ~1 μm thick and showed good adhesion to the substrates. Goldcoated microspheres exhibited a proclivity to stick to the gold-plated support table as the coating thickness increased; however, we could prevent this tendency by increasing the amplitude of the vibratory motion. The gold coatings were ~1.5 μm thick. Further characterization of all these coatings, particularly with respect to thickness uniformity, is in progress. This technique is expected to be particularly useful in applying thin layers of metals onto target microspheres for various diagnostic purposes, such as measurement of temperature by observation of characteristic x-ray emission from the coating.

CRYOGENIC TARGETS

Laser fusion targets fueled with cryogenic liquid or solid DT offer the advantage of high initial fuel density without the disadvantage of diluent atoms that are present in room-temperature solids having a high hydrogen density [such as, lithium in Li(D,T) or carbon in (-CDT)_n]. Theoretical calculations indicate that the yields from targets fueled with liquid or solid-density DT can be considerably higher than those from targets of the same design but fueled with high-pressure DT gas. As a result, we are actively pursuing the development of cryogenic targets despite the significant experimental complications encountered in the fabrication of such targets and in their use in laser-target interaction experiments.

Spherical Geometries

The geometry of cryogenic targets receiving the most emphasis is a uniform, hollow shell of solid or liquid DT condensed onto the inside surface of a glass or metal microballoon container that serves as the pusher shell. We are concentrating our efforts on glass microballoons, simultaneously developing the techniques (a) to condense the DT into a uniformly thick layer on the inside surface of the glass and (b) to measure the thickness uniformity of the DT shell. Two general approaches are being examined. In one case, we impose a temperature gradient deliberately by blowing a jet of cold helium onto the top of the target in an attempt to counteract the effect of gravitational forces; in the other, we surround the target with an isothermal environment and try to freeze the DT uniformly onto the surface.

Temperature Gradient-Technique -- We have previously obtained liquid DT films with good thickness uniformity via the temperature-gradient technique.¹ During the past quarter, these experiments were extended to determine conditions necessary for utilization of this type of cryogenic liquid target in laser-target interaction experiments in our two-beam, CO₂ laser system. With a revised target-viewing system, utilizing a TV camera looking through a 1-m-f.l. Questar telescope provided with multiple Barlow lenses, we could obtain useful images of the cryogenic target at viewing distances we will encounter in our experiments. All components of this viewing system can be located outside the target chamber.

Installation of the target and its cooling system in the target chamber will require at least large holes in the helium-cooled radiation shield for entry of the laser beam and at most the elimination of the entire shield. Therefore, cooling of a DT-filled target in the present "laboratory" apparatus was carried out with various hole sizes in the 4-K radiation shield surrounding the target and with the shield completely removed. With a single jet of cold helium directed at the top of the target, we obtained potentially useful layers of liquid DT, although their thickness was not as uniform as reported previously. We are considering adding more jets, as well as somewhat revising target and

target-chamber geometries, to improve layer-thickness uniformity.

Fast Isothermal Freezing (FIF) Technique-- Our second-generation isothermal target-freezing apparatus became operational, which has advanced considerably our ability to condense uniform, transparent, solid DT layers onto the inside surface of glass microballoon (GMB) targets. In this new method, termed fast isothermal freezing (FIF), the GMB target is supported on a thin glass stalk in the center of a spherical cavity in a copper block that can be cooled to 4 K. The cavity is filled with low-pressure helium gas -- up to 7.3 Pa (55 mtorr) in present experiments -- to serve as a heat-transfer fluid and to provide the primary target-cooling mechanism.

In this technique, we heat the target first with a focused laser beam to melt and vaporize all the DT fuel (which has usually condensed into a very nonuniform film or a solid blob when the chamber is first cooled to 4 K). We then turn the heat source off (i.e., shutter the laser beam), whereupon the very high cooling rate provided by the cold helium heat-exchange gas causes the DT to condense and to freeze onto the inside surface of the GMB target. Solid formation is so rapid that gravitationally driven motion of the liquid DT is negligible. Because the target is cooled isothermally, condensation and freezing occur uniformly over the entire surface of the sphere, providing a solid DT layer of uniform thickness. In addition, the vapor pressure of the DT at 4 to 5 K is low enough to prevent the solid DT layer, once formed, from migrating via vapor-phase transport.

A schematic of the apparatus is shown in Fig. 61. The cell is equipped with four large sapphire windows to allow laser heating, illumination, and observation of the target. These windows allow continuous observation of the melting/vaporization and condensation/freezing processes. A schematic of the viewing system and of the laser heating system is shown in Fig. 62. For viewing purposes, light from the target is collected by a two-lens optical system, imaged onto a silicon-diode matrix vidicon, and displayed on a TV screen. This allows us to use illumination of very low intensity (<8 nW), minimizing perturbations of the frozen target

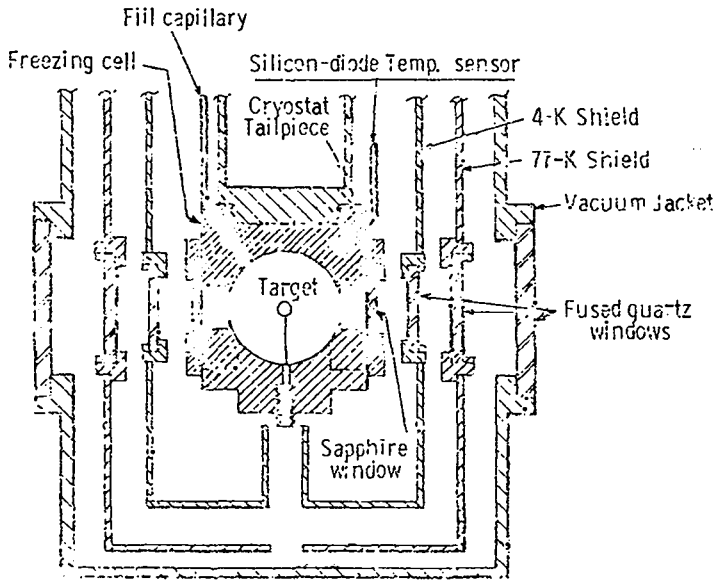


Fig. 61. Schematic of apparatus used in the fast isothermal freezing (FIF) technique to prepare cryogenic targets having a uniform layer of solid DT deposited on the inside surface of a glass microballoon.

from this source. Permanent records of experiments are kept on videotape for future photographic re-

production and analysis. (We have also obtained some direct-view motion pictures for timing analysis of events that are too fast to be resolved on the TV screen.)

A wedge interferometer, shown schematically in Fig. 63, can be inserted into the target observation system to allow high-resolution analysis of DT-layer thickness uniformity. The interferometer wedge angle of 1 min and the surface reflectivity of 50% cause the directly transmitted light to interfere with the reference field of the twice-reflected light. A laser coherence-length constraint of twice the wedge thickness is readily met with a laser of 4880-Å wavelength. The wedge is oriented so that the reference beam has a constant phase over the target image so as to produce clear interference fringes. Here again, the required laser illumination intensity is extremely low, owing to the high sensitivity of the TV vidicon. For lower-resolution examination of the target and the frozen DT layers, we use the Reedy refraction technique.⁷ In this technique, we focus the observation system onto the back surface of the target and obtain a measure of the lensing effect of the target, which can then be related to the detailed

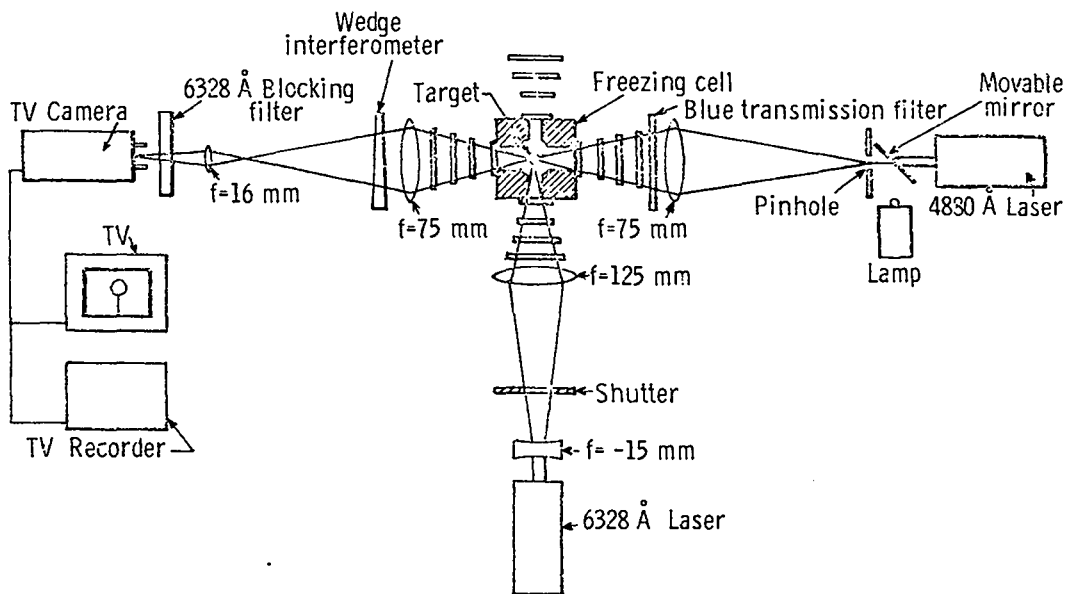


Fig. 62. Schematic of observation, laser-heating, and wedge-interferometer optical layout used in the FIF technique.

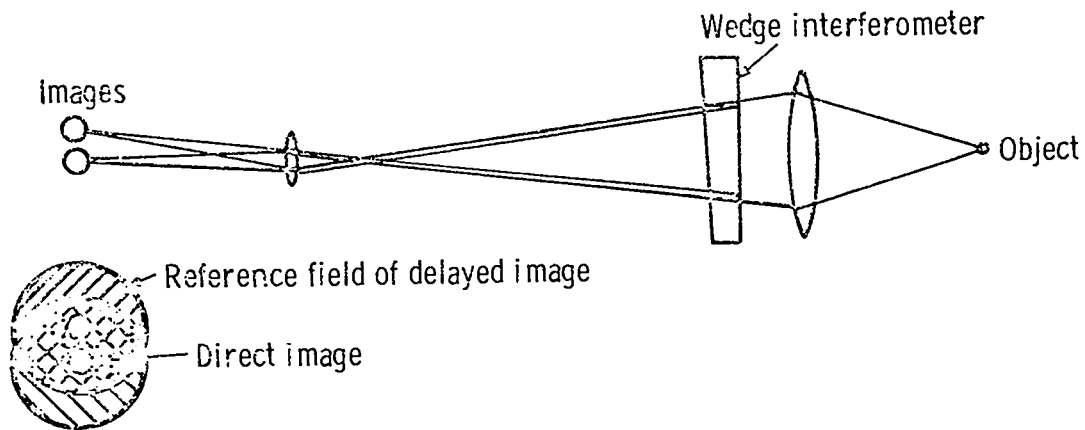


Fig. 63. Detailed schematic of wedge interferometer used for high-resolution examination of the DT layers frozen onto the inner surface of a glass microballoon.

geometry of the target. This, of course, requires only the use of our normal viewing optics. Figure 64 shows the appearance of DT-gas-filled and DT-

solid-shell targets on the TV system in normal observation (i.e., focused on the equator of the target) and in the Reedy method.

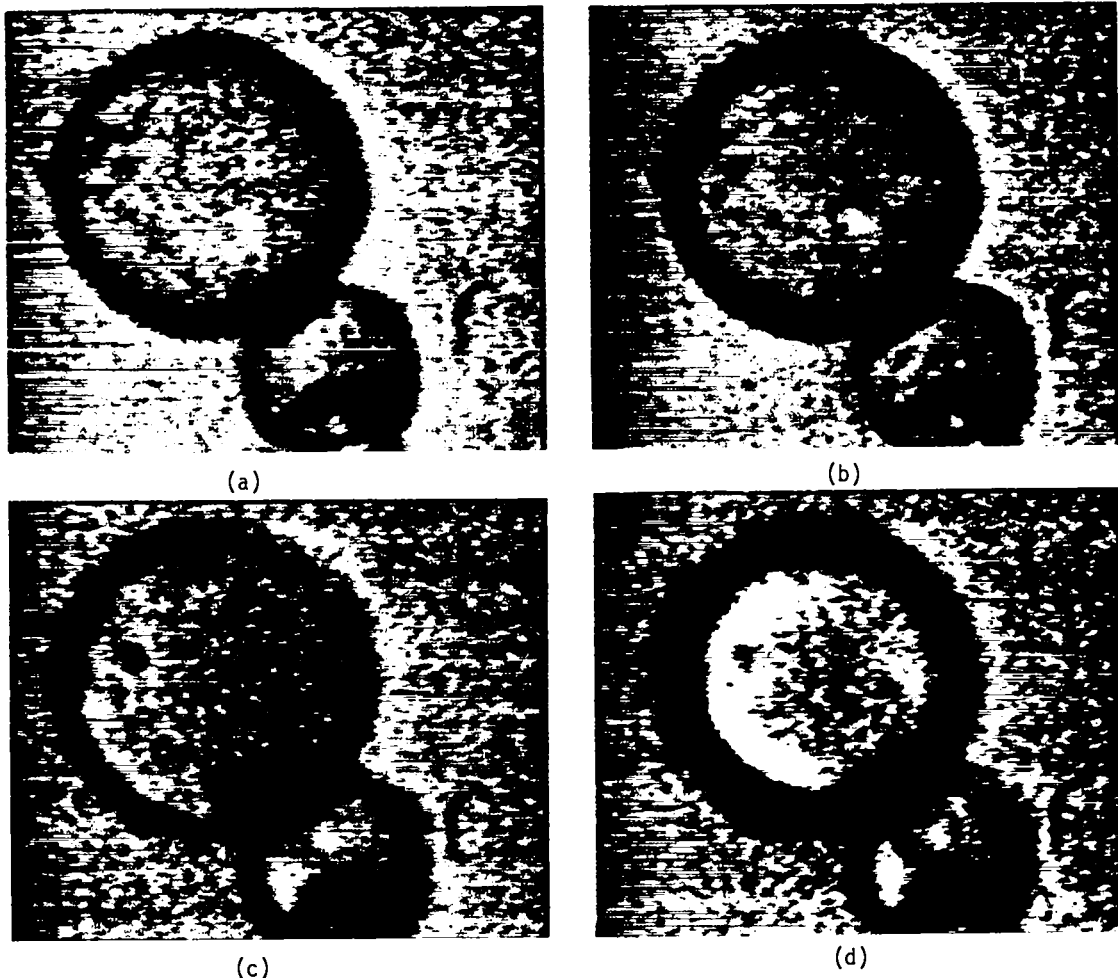


Fig. 64. Typical TV screen views of a cryogenic DT-fueled glass microballoon (GMB) target. In views (a) and (c), all the DT is present as gas; in views (b) and (d), DT is present as a uniform solid shell. In views (a) and (b), we are focused on the equator of the GMB to directly observe the DT shell. In views (c) and (d), we are focused behind the GMB to generate the Reedy refraction-type dark rings.

For heating and vaporizing the DT, we are now using a 2-mW helium-neon laser focused to about the target diameter and introduced perpendicularly to the viewing axis. The laser is aligned by observing the projected diffraction pattern. A blocking filter in the viewing system prevents saturation of the vidicon by scattered and reflected light from this laser so that the target can be observed while being heated. With 2 mW of laser power available to heat the target, we can vaporize the DT in a target completely, provided that the pressure of the helium heat-transfer gas is 7.3 Pa (55 mtorr) or less. The solid DT layers of highest quality are obtained at the 7.3-Pa exchange-gas pressure. At lower pressures, the condensation/freezing process is slower, and nonuniform layers may be obtained because of gravitational flow of the liquid DT.

With our maximum cooling rate, the time lapse between closing the shutter of the heating laser and formation of solid DT is ~300 ms for a typical 100- μ m-diam GMB filled with 10 ng of DT fuel. The sequence of photographs in Fig. 65 shows a freezing cycle from gas to solid at intervals of 16 ms in a direct view taken with a 16-mm motion-picture camera. This sequence begins 12 frames after the laser shutter is closed.

A significant advantage of the FIF technique is its excellent reproducibility, at least under fast-cooling-rate conditions. The thickness uniformity of the frozen DT layer does not depend critically on the alignment of the heating laser, provided that all the DT fuel is vaporized. If this criterion is met, uniform solid DT layers are obtained reproducibly through an arbitrary number of multiple melting/vaporization-condensation/freezing cycles.

Work in progress includes the design of a FIF system for use in the two-beam CO₂ laser system. This effort will require a mechanism to rapidly withdraw the cell immediately before the laser shot, allowing full laser irradiation of the target and complete diagnostics. We also plan to obtain a more powerful laser for heating the target so that still faster condensation/freezing rates can be evaluated. In addition, our computer code that calculates interferograms¹ is being modified to accommodate shells with multiple layers of differ-

ing refractive indices. This will allow us to calculate predicted interferograms for various GMB and DT layer geometries.

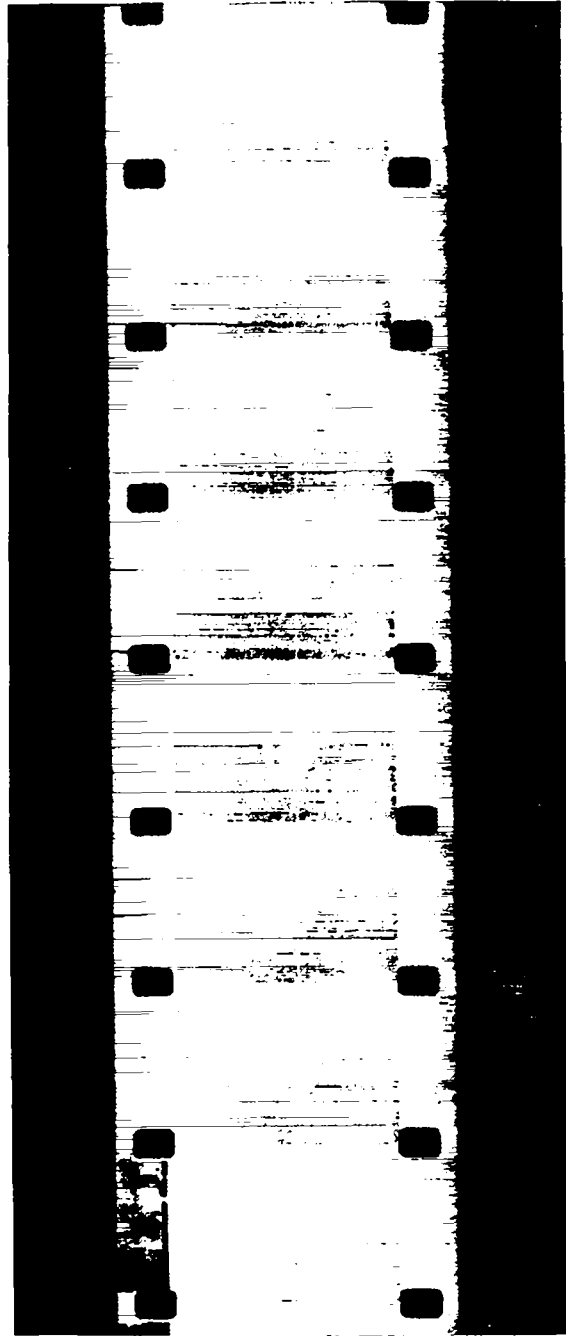


Fig. 65. Sequence of photographs of the freezing process obtained by viewing the target directly with a 16-mm motion-picture camera. Framing rate is 64 f/s; adjacent frames are thus 16 ms apart. This sequence (which begins 12 frames after the laser shutter is closed) shows the entire freezing process from gas-phase DT on the top to a solid shell on the bottom.

REFERENCES

1. E. Stark and F. Skoberne, Los Alamos Scientific Laboratory report LA-6510-PR (November 1976), Sec. IV.
 2. T. M. Henderson, KMS Fusion, Ann Arbor, Michigan, private communication (March 1976).
 3. F. Skoberne, Los Alamos Scientific Laboratory report LA-6050-PR (January 1976), p. 76.
 4. F. Skoberne, Los Alamos Scientific Laboratory report LA-6050-PR (January 1976), Sec. V.
 5. F. Skoberne, Los Alamos Scientific Laboratory report LA-6245-PR (July 1976), p. 80.
 6. W. R. Holman and F. J. Huegel, Proc. 2nd Conf. on Chemical Vapor Deposition, Electrochemical Society (Los Angeles, California, 1970), p. 171.
 7. R. P. Reedy, Lawrence Livermore Laboratory report UCRL-76903 (1975).
-

V. TARGET DIAGNOSTICS



The tiny volume and brief duration involved in the laser fusion process create needs for new diagnostic techniques having spatial and temporal resolutions in the submicrometer and 1- to 100-ps regime, respectively. These needs are being met with a vigorous program of diagnostics in such areas as laser calorimetry, charged particle and neutron detection, x-ray spectrometry, and subnanosecond streak-camera development.

INTRODUCTION

We are striving continuously to improve our ability to examine the fine details of laser-induced plasmas and to record with greater precision the phenomena associated with laser-target interactions. To do this, we need diagnostic instruments that record data faster and with greater resolution than presently possible; they should be as simple and rugged as practicable and must function with a reproducibility that minimizes shot-to-shot variations and uncertainties.

These requirements impose demands that can be met only by continually advancing the state of the art through, e.g., modifications and improvement of conventional techniques and equipment; enhancement of capabilities through invention and new development; and exploration of new concepts and theories. This varied approach to improving our diagnostic capabilities is discussed in the following paragraphs.

Major emphasis was placed on x-ray imaging, spectral analysis and time resolution, optical plasma diagnostics, and charged-particle detection. Work on isolation and imaging of CO₂ lasers is reported in Section I.

X-RAY MICROSCOPE DEVELOPMENT

Tests on ellipsoid-hyperboloid x-ray microscope systems fabricated at UCC's Oak Ridge Y-12 plant (see LA-6510-PR) have shown that the resolution is better than 25 μm . Studies of surface finish and errors indicate that resolution approaching 1 μm should be attainable inexpensively by using the new micromachining techniques.

Microscopes of this type have collection areas 10^3 to 10^4 times larger than a typical 5- μm -

resolution pinhole camera, but as laser energies increase, such sensitivity will not be necessary nor even desirable. Therefore, a ray-tracing study has been performed in an attempt to find simpler geometric shapes that give adequate resolution and sensitivity. We found that, near the intersection of the ellipsoid-hyperboloid pair, the surfaces can be replaced by straight-line approximations which give 1- to 2- μm resolution with a solid angle 20 times that of a 5- μm pinhole camera. The resulting optical system, then, is a pair of intersecting cones whose critical parameter is just the straightness of the sides. These systems are ideally suited for diamond-point turning, and prototypes will be fabricated at Y-12. Also, spherical sections can be used to increase the collecting aperture if necessary. Such systems will be much easier to fabricate and to test than those using ellipsoid-hyperboloid pairs regardless of whether they are produced by diamond-point machining or by conventional methods.

PROXIMITY-FOCUSED X-RAY STREAK CAMERA

The dynamic range of the proximity-focused x-ray streak camera has been tested by using a series of filters across the camera slit to provide energy windows (i.e., channels) at 1, 1.6, 2.8, and 5.0 keV. Figure 66 shows the streak-camera record of x rays emitted when a 200- μm -diam nickel ball was irradiated by our dual-beam Nd:glass laser with an intensity of $\sim 10^{15}$ W/cm². The densitometer traces of these streaks are shown in Fig. 67. It is evident from the traces that radiation in these windows "lingers" after the 70-ps irradiation pulse. The higher the energy channel the more nearly the emission history resembles the irradiation pulse. These data and similar experiments



Fig. 66. Streak-camera record of x rays emitted from 200-mm-diam nickel ball irradiated by dual-beam Nd:glass laser.

imply a dynamic range in excess of 100, independent of camera sweep speed and peak conductance. Because it is difficult to predict x-ray spectra and fluxes from shot to shot, we need an instrument with at least this range to be a useful diagnostic tool. The theoretical dynamic range for the system depends upon the image intensifier. For resolution commensurate with the streak tube, this dynamic range is predicted to be in excess of 10^3 . Pinhole optics with $10\text{-}\mu\text{m}$ spatial resolution have been used to study compressions with the proximity-focused streak tube. This system will yield information on

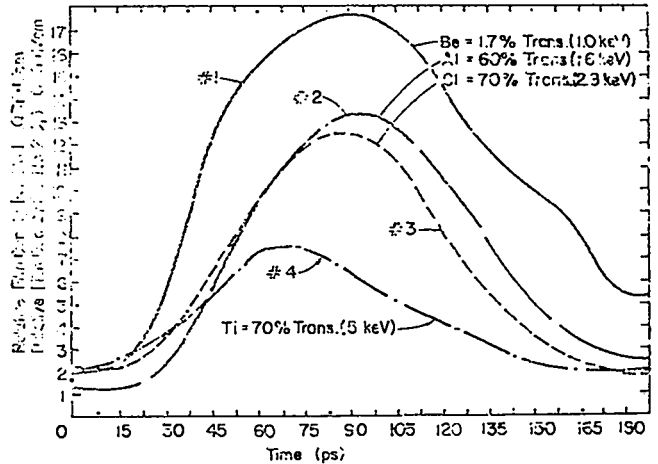


Fig. 67. Densitometer traces of streak-camera record shown in Fig. 66.

the target interiors rather than just the surfaces, as with slits.

OPTICAL DIAGNOSTICS OF TARGET PLASMAS

General

We intend to study the establishment of severe density profiles in plasmas produced by $10.6\text{-}\mu\text{m}$ laser pulses. This and other information on density profiles is best measured with optical diagnostics.

Interferometer

We determined the type of interferometer and the design which would meet the following specifications:

- Field of view, $400\ \mu\text{m}$;
- Resolution for illumination by $0.53\text{-}\mu\text{m}$ light, 1 to $5\ \mu\text{m}$;
- At least two frames per interferometer taken at different times during the CO_2 laser pulse;
- Compatibility with CO_2 focusing optics and other diagnostics for two interferometers;
- Compatibility with illumination of fractional picosecond duration;
- Two interferometers to view the plasma from directions normal to each other;
- Techniques extendable to 4 to 6 frames per

interferometer with adjustable interframe time;

- The possibility of operating one interferometer at $0.53 \mu\text{m}$ and the other at $0.35 \mu\text{m}$, or both at $0.53 \mu\text{m}$.

We evaluated three holographic and four conventional interferometer schemes, involving Fabry-Perot pulse stackers, Jamin beam splitters, Mach-Zehnder-type interferometers, moiré optical tests, and multiple-grating interferometers.

We settled on the scheme illustrated in Fig. 68, a two-frame grating interferometer where $f_2^{-1} = l_1^{-1} + l_2^{-1}$. Two separate interferograms are created in each camera, depending on which order of Grating 1 interferes with the two orders of Grating 2. Because the two optical paths are of equal length, this interferometer is achromatic, and coherence lengths do not pose a problem for pulses of 0.5- to 5-ps duration. By using both directions of polarization, two independent frames can be taken on separate portions of the film. Using a helium-neon laser as a test illumination source, we obtained 1.5- μm resolution over a 1-mm field of view at both cameras. Interferograms of glass microballoons were then taken. They are very similar to those taken with an interference microscope, despite the fact that our initial tests were performed with inexpensive 100-line/in. gratings. We will repeat these tests with high-quality 150- and 300-line/in. gratings. The final system will

be designed around the well-corrected 75-mm f/1.9 lenses used in the original tests.

The Two-Beam CO_2 Laser System was chosen for these experiments because it offers space for diagnostics which will require 10% or more of the total solid angle around the target (without mounting hardware).

We have examined the following method of reducing interferograms to three-dimensional, time-resolved plasma-density profiles. First, the data are taken on film. They are then prepared for digitizing and high-speed disk storage by using a TV viewing system coupled to a single-frame disk recorder. Ordinarily, when the data are available for processing, one uses an Abel inversion scheme, which assumes that the plasma is cylindrically symmetric. However, because we will take two interferograms with probe beams traveling perpendicularly to each other at each probe time, it is not necessary to assume cylindrical symmetry. We plan therefore to develop a more general scheme that will take full advantage of the additional information we expect to have available.

Target Integrity Studies

We are examining the applicability of an Electrophotonics dye laser to target integrity studies and, possibly, to shadowgram production. The laser was carefully diagnosed and found to produce 5-ps pulses at an adjustable interpulse time of 3 to 5 ns with $100 \mu\text{J}/\text{pulse}$. The near field was a time-

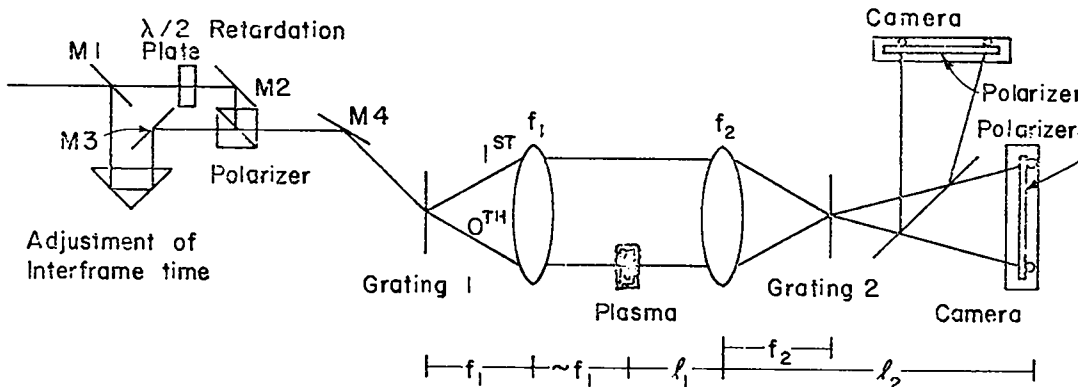


Fig. 68. Two-frame grating interferometers for examining dynamics of plasma-density profiles.

integrated 3- by 6-mm elliptical cross section, but when time-resolved was found to be a 1-mm-diam beam which systematically moved around over the 3- by 6-mm amplifying aperture. The 5-ps pulses of 590-nm wavelength were then used to establish the short-pulse illumination characteristics of a Hadland Model-700 streak camera. A resolution of 3 to 4 line pairs/mm was possible, but 1 nJ per resolution point was now required for good exposure rather than 10 W per resolution point, typical of pulses exceeding 200 ps. We are examining various transfer optical systems that might be employed with this equipment for either laser or target diagnostics.

Analysis of Interferograms

Our previously developed computer code, which performs ray-tracing through media with spatially varying indexes of refraction and calculates simulated interferograms, was used to study various plasma density profiles. Particularly emphasized were profiles containing a narrow region of steep slope to simulate the profile expected when a plasma is irradiated with very intense light. First attempts failed -- the code would not run with a profile containing a steep region. This failure was thought to be due to a discontinuity in the slope at the boundary of the steep region, but was later shown to be due to ray-crossing produced by a region with a large refractive-index gradient. After many trials we concluded that simulated interferograms can be produced only if the gradients are reasonably small everywhere within the region of probe-light penetration.

With respect to real laser-generated plasmas, in which the index gradients are expected to be large near the critical electron density for the heating laser, our experience implies that the interferometric method will produce quantitative data only if the probe-light wavelength is quite short -- about 0.25 μm or even shorter. However, if one needs to determine only the existence and location of a steep slope in the plasma, visible probe light may well be useful.

A numerical example may illustrate the situation. Consider a plasma generated by 10- μm light for which the critical electron density $n_c = 10^{19}/\text{cm}^3$. If we assume that the top of the steep

region is $100 n_c$ and the bottom is near zero, then the top of the steep region is $0.25 n_{cp}$ to half-micron probe light and is $0.0625 n_{cp}$ to quarter-micron light, where n_{cp} is the critical electron density for the particular probe light. Simulated interferograms cannot be obtained with the half-micron probe light if the slope of the "steep region" is much steeper than that of a congruent Gaussian function. The situation improves considerably with quarter-micron probe light because the top of the steep region is only at one-sixteenth critical density. However, the steep region must still be more than a few microns wide. Even when simulated interferograms can be generated, if the slope is steep, the fringe spacing near the angular acceptance limit becomes very crowded, thereby casting doubt on the possibility of deriving quantitative data from experimental interferograms of plasma containing a reasonably steep region of density falloff.

Angular Deviation of Light -- A Potential Plasma Diagnostic

As discussed above, computer simulations indicate that interferometry, particularly in the visible region, suffers severely as a quantitative diagnostic of laser-generated plasmas. While this is true a fortiori for plasmas containing a steep region of electron-density falloff, it is also true to some degree for all dense plasmas because the useful depth of penetration is limited by the angular acceptance of the interferometer and by fringe crowding.

Consideration of these problems in visible and near-ultraviolet interferometry led to the idea of dispensing with the interferograms and measuring only the angular deflection of the light caused by the presence of the plasma. This idea originated from the observation that the computed curves of angle of deviation vs impact parameter exhibit a cusp or kink at an impact-parameter value fairly close to the radius at which the input electron-density profile has a steep region. Thus, if angular deviation vs impact parameter could be unfolded from observed intensity-vs-angle curves, the existence and location of anomalously steep regions could readily be ascertained. Because an imaging optical system is not required, very large angular

deviations could be measured, thereby allowing relatively great penetration depths even in the visible region of probe wavelength.

Moreover, a possibility exists of unfolding the observed intensity-vs-angle data to obtain the electron-density profile in the plasma. First, the angle-vs-impact parameter function would have to be extracted. This requires knowledge of the beam-intensity profile and the offset displacement of the beam from the center (pole) of the plasma. This offset parameter could be obtained if two coaxial laser beams of different wavelength irradiated the plasma simultaneously, and two sets of intensity-vs-angle data were obtained. Second, the derivative of the angle-vs-impact parameter function thus obtained would be used as input to a second unfolding algorithm to obtain the electron density as a function of radial distance in the plasma.

While both the experimental and the data-reduction (unfolding noisy data) procedures involve potential difficulties which should not be ignored, these difficulties may be no greater than the corresponding ones for the interferometric method. However, in any case, the potential payoff of the angular-deviation method is greater in terms of gaining information at relatively large plasma depths without using vacuum-ultraviolet probe light.

Because the Abel inversion is strictly valid only in the absence of angular deviation of the rays, its utility in determining electron-density profiles in dense, laser-generated plasmas is open to question. However, ongoing numerical simulation tests indicate that Abel inversion is reasonably accurate, at least for deviations no larger than the 14° half-angle acceptance of an $f/2$ optical system.

Jamin Interferometer

A compact, modified Jamin interferometer with large acceptance angle is being designed for use on laser-produced plasmas. This interferometer should be easier to align and to use than correctional Jamin interferometers. It should also provide data at higher electron densities. The interferogram of a segment of a $150\text{-}\mu\text{m}$ -diam glass microballoon made with a bread-board version of the interferometer is shown in Fig. 69.



Fig. 69. Interferogram of a glass microballoon segment (diameter, $150\ \mu\text{m}$).

TARGET-PLASMA ION MEASUREMENTS

Experiments are being conducted to study the response characteristics of two types of plasma ion detectors: (1) flat-plate probes and (2) Faraday charge cups, shown in Figs. 70 and 71, respectively. The depth-to-diameter ratio of the Faraday collector cup is 9. The probe and Faraday cup are simply constructed with Berkeley Nuclear Corp. and General Radio Corp. connector components, which are off-the-shelf items.

Polyethylene plasmas were produced with a 30-ps, 1- to 5-J Nd:glass laser pulse. Results show the following features:

- Signals from the ion probe require corrections due to secondary-electron emission effects. Comparative analysis of signals from the probe and the Faraday cup has been used to determine secondary-electron emission coefficients for pulsed ion operation.
- Noise signals observed in the fast-ion region can be eliminated by placing a magnetic field between the plasma and the ion detector to sweep out electrons with energies up to 200 keV. The ions in this velocity region are unaffected by the magnet.
- Both the probe and the Faraday cup show a cutoff level for measuring ion number

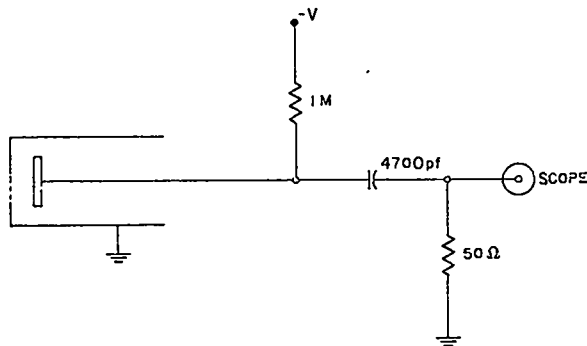


Fig. 70. Schematic of flat-plate probe.

densities. At a grid-to-collector distance of 1.6 mm, an incident ion density of 10^{10} ions/cm³ was sufficient to cause arcing. This cutoff appears only in the low-energy (plasma ions) region. When the grid-to-collector spacing was increased to 6 mm, arcing was no longer observed.

CALIBRATION OF ION CALORIMETERS

We have determined some performance characteristics (risetime and sensitivity) for the low-mass calorimeter used to measure ion absorption in laser-target interaction experiments.

Risetime measurements were made by using a Nd:glass laser pulse (30 ps FWHM) in a vacuum chamber to determine the delta-function input response. These measurements show the risetime to be $10 \pm 1 \mu\text{s}$ and the cooling curve to be an exponential decay with a 12-s time constant in vacuum.

Sensitivity measurements were made in a similar manner, using a calibrated CO₂ light source (pulse duration, 1 ns FWHM) apertured to just fill the 1.6-mm-diam calorimeter surface.

A Hewlett-Packard 7202 high-gain, low-noise strip-chart recorder was used to record the signals of 24 different calorimeters. The average sensitivity was $0.43 \text{ V/J} \pm 1.2\%$.

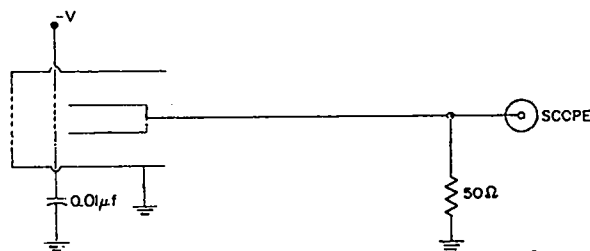


Fig. 71. Schematic of Faraday charge cup.

LASER STABILIZATION AND SYNCHRONIZATION

Some important diagnostics require precise synchronization with the arrival on target of the CO₂ laser pulse. For example, a synchronized laser pulse at $1 \mu\text{m}$ can be a valuable diagnostic in probing steep density gradients.

However, the Nd:glass oscillator is highly sensitive to vibration, acoustical noise, and temperature variations, which makes precise timing difficult. We are therefore beginning to study an Invar steel structure which, we hope, will suggest solutions to the difficult alignment problems that have been a major limitation of this glass system. The Invar steel structure was designed to support a CO₂ smoothing-tube-stabilized oscillator interferometer. This structure should eliminate the CO₂ oscillator fluctuations and the lack of reproducibility related to changes in laser-cavity length. At the same time, it will allow evaluation of this stabilizing concept for its applicability to the Nd:glass oscillator problem.

We have studied all the CO₂ laser timing requirements to determine critical problems related to synchronizing the Nd:glass system with the CO₂ laser facility. A similar study for the glass system will follow.

STEREOSCOPIC POLARIZATION CAMERA

We have designed an imaging system to photograph the second-harmonic light ($0.53 \mu\text{m}$) emitted by a $1.06\text{-}\mu\text{m}$ laser-produced plasma. Four images will be recorded simultaneously to provide stereoscopic views of the plasma in two perpendicular polarizations. These views should allow us to determine and correlate the orientation of flare-like structures, observed previously, with the measured anisotropic emission of fast electrons.¹ Differences between the polarized images may provide some information about density gradients and magnetic fields.

The system, shown schematically in Fig. 72, consists of a biprism and a Wollaston prism in a

relay-lens imaging system. The biprism separates the light rays that pass through two halves of a large lens so that two stereoscopic images are produced on the film plane. The Wollaston prism deflects rays of different polarization, again doubling the number of images.

The stereoscopic photograph of a broken $100\text{-}\mu\text{m}$ -diam glass microballoon, shown in Fig. 73, was made with a laboratory mockup of the camera. The shape of the shard can be easily discerned. The resolution has been measured at 160 line-pairs per millimeter.

The final version of the camera is under construction and will soon be in use.

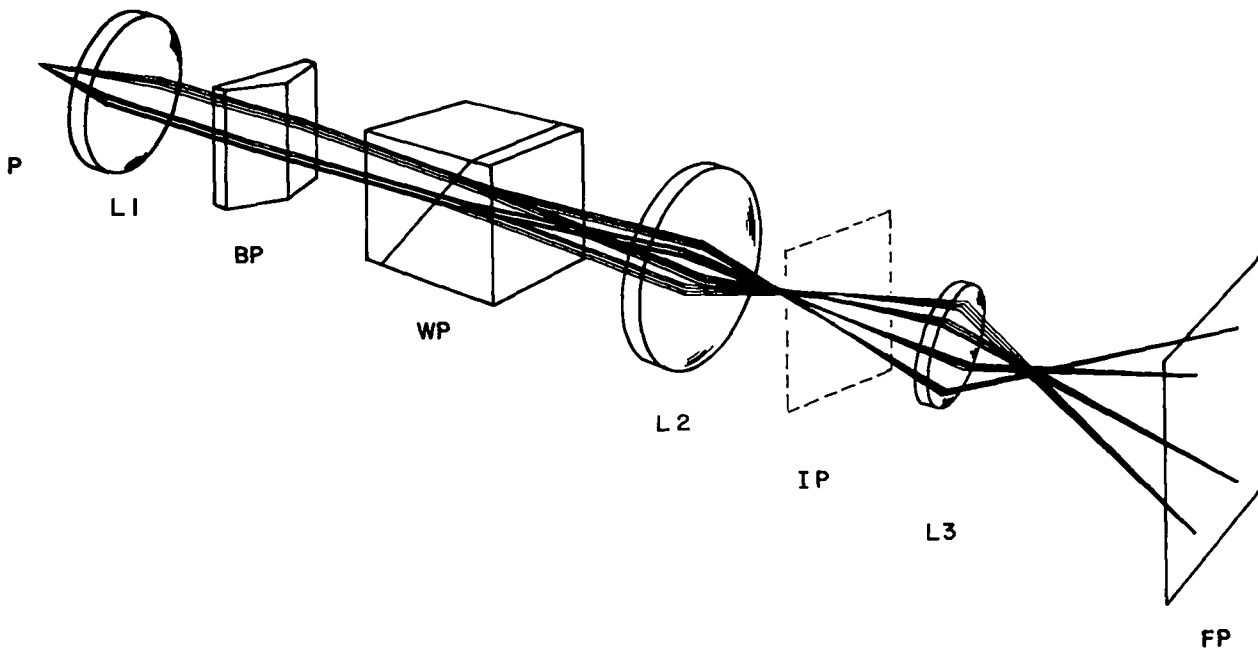


Fig. 72. Schematic of stereoscopic polarization camera: P - plasma; L₁, L₂, and L₃ - lenses, BP - biprism; WP - Wollaston prism; IP - Intermediate Image plane; FP - film plane.

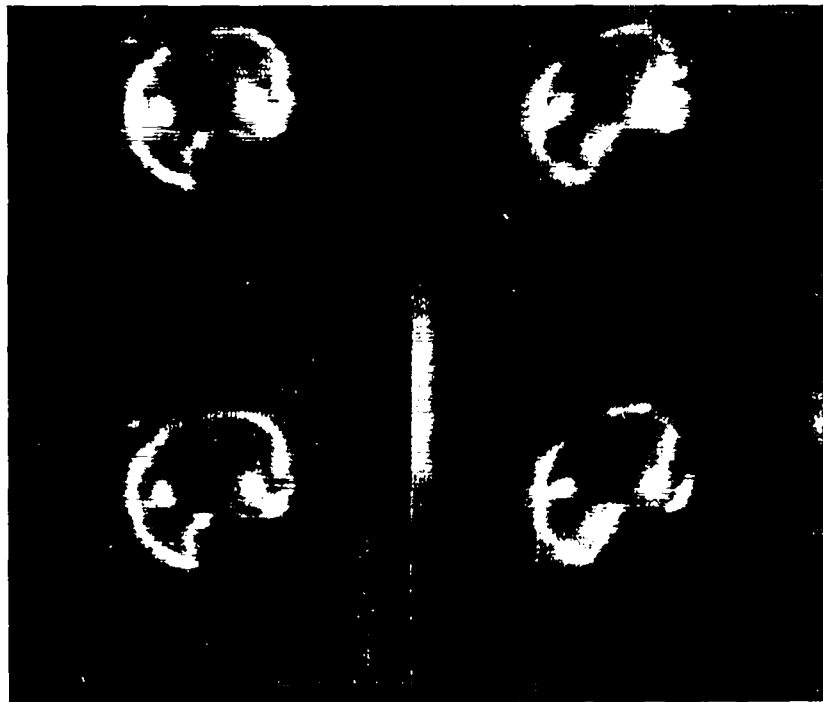


Fig. 73. Image of broken microballoon taken with stereoscopic polarization camera (diameter, 100 μm).

THIN-FILM SCINTILLATOR DETECTORS

Thin-film time-of-flight detectors are routinely used to monitor the laser beams during all our target shots. They give instant feedback of crucial information on the presence of precursors, variation in laser intensity, and target focusing quality. We consistently see a steep rise in the leading edge of the fast-ion spectrum. This enables us to correlate fast-ion measurements with data from other diagnostics to reduce shot-to-shot uncertainties and to enhance the credibility of the data. Fast-ion measurements are now being made with the Two-Beam CO_2 System to gather information on laser wavelength scaling, energy transport, vacuum insulation, and other relevant issues.

SOFT X-RAY DIFFRACTION SPECTROMETER

We have assembled a modular 10-channel, soft x-ray spectrometer incorporating three Bragg cry-

stal channels and two K-edge filter channels. This system was installed on the target chamber of the Two-Beam CO_2 System. Experiments are in progress to determine the signal-to-noise characteristics for both plastic-photoamplifier scintillator and PIN (P-type insulator N-type diode) photodiode detectors.

PLASTIC TRACK DETECTORS

In the study of laser-induced fusion, variations in beam geometry, beam profile in time, and target construction require a reliable technique for measuring plasma configuration and fusion yield from different experimental arrangements. Electronic detectors are hard pressed to satisfy this demand because of "pileup"; heavy ions from the implosion reach the detectors within 100 ns, resulting in a superposition of pulses. Moreover,

such detectors are sensitive to all charged particles arising from primary or secondary causes (i.e., electrons and gamma rays), and these can mask or distort heavy-ion pulses.

Plastic track detectors appear to provide a useful heavy-ion identification technique that does not suffer from these limitations. They are quite insensitive to hydrogen nuclei (except those at low energy) and they do not record electrons. The type of plastic track detector principally used in these studies is Kodak Pathe CA 80-15 cellulose nitrate. We ascertained early in 1976 that ion-produced etch pits start to form at different times, depending on the atomic number and on the energy of the ion that produces them, when such detectors are etched so that track formation can be viewed continuously. This delay, or etch induction time provides a sure and simple method for analyzing heavy ions emitted in a variety of applications. It could be used as an excellent fusion-yield diagnostic tool and would also be sensitive to ions of carbon, oxygen, and silicon emitted from the target. A minimum energy of 0.2 to 1.0 MeV/amu is the requisite energy threshold for all ions.

Measurements were principally directed toward stabilizing the behavior of cellulose-nitrate track detectors for reliable ion identification. Preliminary studies of environmental problems with 2.5-MeV ^4He ions revealed the following:

- Preirradiation storage conditions (with one important exception, temperature, to be discussed later) have no discernible effect on etch induction time, track length, or track etch rates.
- The effects of postirradiation storage conditions are more complex within the wavelength limitation of optical microscopy. Simple storage in one environment (dry air, water, 100% relative humidity) seems to have no effect. However, wetting followed by drying in air nearly doubled the etch induction time, without changing track length, l_p , or any other parameters (see Fig. 74). There is some evidence that storage in a hard vacuum

after irradiation will lead to an increase in etch induction time and to a reduced track etch rate, suggesting that prolonged vacuum storage causes loss of the plasticizers.

- Thermal effects may contribute to deterioration in vacuum. The body of the plastic material appears to deteriorate when subjected to temperatures above 313 to 323 K (40 to 50°C), however briefly. Also, prolonged preirradiation storage at 298 to 303 K (25 to 30°C) can have the same effect. Some valuable cellulose-nitrate calibration data, taken at LASL and mailed to Washington State University during warm weather, showed the characteristic short ranges and reduced etch induction time of thoroughly heat-damaged and partially decomposed cellulose nitrate.

As a result of these studies, the cellulose-nitrate films are now stored at 273 K (0°C) in plastic bags of desiccant, without lights -- cool, dark, and dry -- and shipped only by private conveyance in a refrigerated container. It appears

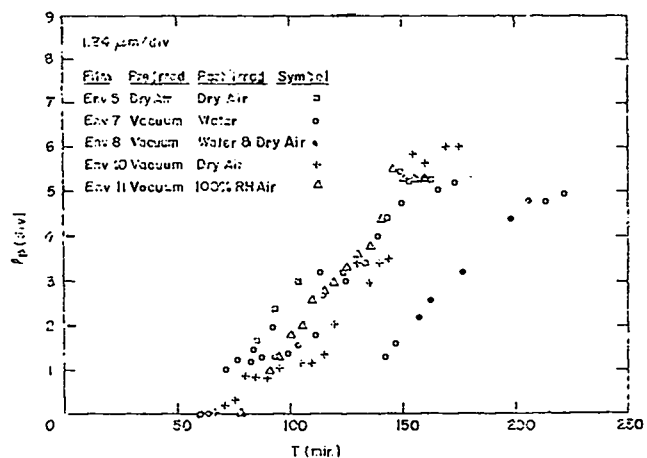


Fig. 74. Influence of environmental conditions on etch induction time.

that careful control of storage conditions and frequent calibration are required if cellulose-nitrate films are to be used for quantitative measurements. Work is in progress on the calibration of etch induction time versus angle of the incident particle. We will try to increase etch induction time (and thus enhance the differential sensitivity to heavy ions of high atomic number) by wetting and drying the films in some pattern suggested by the data in Fig. 74. Measurements are being made of a postulated mass effect on etch induction time with films exposed to ^3He and ^4He ions. The existence

of etch induction time in Lexan polycarbonate is being explored. Lexan is intrinsically less sensitive than cellulose nitrate but presumably more stable under thermal extremes. Lexan can be sensitized to record helium ions by postirradiation treatment with uv light.

REFERENCE

1. D. V. Giovanielli, J. F. Kephart, and A. H. Williams, J. Appl. Phys. 47, 2907 (1976).

VI. APPLICATIONS OF LASER FUSION -- FEASIBILITY AND SYSTEMS STUDIES * *

Our feasibility and systems studies are being performed to analyze the technical feasibility and economic aspects of various commercial and military applications of lasers and laser fusion. The direct production of electricity in electric generating stations is of major concern. The general objectives of these studies are: the conceptualization and preliminary engineering assessment of laser fusion reactors and other generating-station subsystems; the development of computer models of generating-station subsystems for economic and technology tradeoff and comparison studies; and the identification of problems requiring long-term development efforts. Emphasis in military applications studies is placed on relatively near-term weapons-effects simulation sources and facilities.

STUDIES OF MAGNETICALLY PROTECTED LASER FUSION REACTOR CONCEPT

The use of magnetic fields to protect the cavity walls and final optical surfaces in a laser fusion reactor (LFR) from damage by energetic charged particles in the fusion-pellet debris has been discussed previously (see, e.g., Ref. 1). Magnetic fields are used to deflect charged particles from the cavity walls and beam-transport tubes onto energy-sink surfaces where the ions are collected and their energy is recovered.

Although the validity of the magnetically protected wall concept has been established by previous studies, the shapes of the energy-sink surfaces have not been optimized. We are now studying this problem for reactor designs that have cylindrical cavities with energy-sink surfaces in the open ends of the cylinder. We wish to define energy-sink shapes for which sputtering from energetic ions is as nearly uniform over the energy-sink surface as possible. In addition to varying the shapes of the energy-sink surfaces, the shapes of the magnetic fields can also be varied by appropriately designed solenoids.

The energy-sink configurations that we have considered are indicated schematically in Fig. 75. The cavities are axially symmetric, with energy sinks in each end of the cylindrical cavities. The principal investigative tools used in these analyses are the computer program LIFE (Laser-Induced Fusion Explosion) that simulates fusion-pellet microexplosions expanding in magnetic fields and the sputtering codes that have been developed re-

cently.² We have performed calculations for a bare (D+T) fusion-pellet design, with a 100-MJ yield.

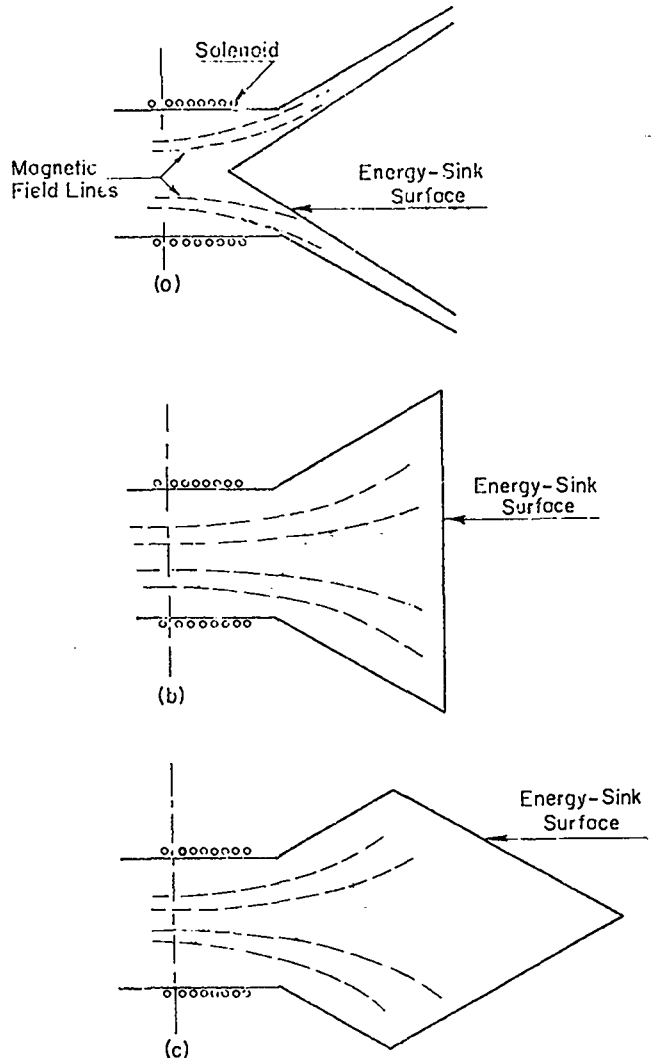


Fig. 75. Energy-sink configurations for magnetically protected reactor concept.

We have also performed sputtering calculations for reactors with minimum permissible cavity radii, as determined by allowable cavity-wall surface heating from x-ray energy deposition. For the bare (D+T) fusion pellet, the cavity-wall and energy-sink surface material was niobium, and the maximum permitted cavity-wall surface temperature increase from a pellet microexplosion was assumed to be 1500 K. For the x-ray yield and spectrum given in Table VIII, this leads to a minimum cavity radius of 2.5 m. The results of sputtering calculations for the bare (D+T) fusion pellet expanding in a 0.2-T magnetic field and the energy-sink configuration shown in Fig. 75a are presented in Fig. 76. As indicated, sputtering near the conical tip is intolerably large, and sputtering over the entire surface is far from uniform. In fact, sputtering occurred over only 25% of the available energy-sink surface. The sputtering distribution indicated in Fig. 76 is as near to uniform sputtering as could be obtained by varying the shape of the magnetic field for this energy-sink configuration.

Sputtering from the bare (D+T) pellet is shown in Fig. 77 as a function of the radius of a niobium flat-plate energy sink (Fig. 75b). The results of calculations for both a 0.1- and a 0.2-T magnetic field are shown. The sputtering distributions are more uniform than for the inward-pointing conical energy sink shown in Fig. 76; however, there is still excessive sputtering near the center line, and the edges of the energy-sink surfaces are not well utilized. The average sputtering for the 0.1-T magnetic field is less than for the 0.2-T field because the 0.1-T field is too weak to completely contain the expanding plasma so that ~16%

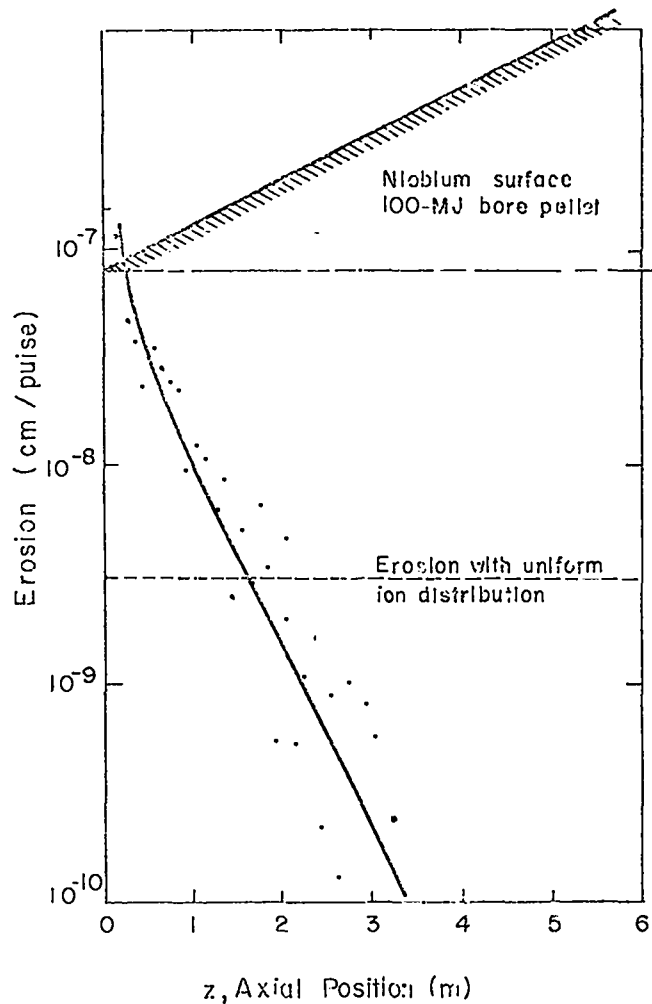


Fig. 76. Sputtering erosion per pellet microexplosion of an inward-pointing conical energy sink.

of the ions impinge on the cylindrical cavity walls. These results indicate that more uniform sputtering can be achieved for the energy-sink configuration shown in Fig. 75c than for the other two.

TABLE VIII

OUTPUT CHARACTERISTICS OF 100-MJ BARE (D+T) FUSION PELLETS

	<u>Fractional Energy Release (%)</u>	<u>Average Energy per Particle</u>
X rays	1.0	~1.4 keV equivalent blackbody spectrum
Pellet debris	22.0	~50 keV
Neutrons	77.0	~14 MeV

STUDIES OF ION-BEAM FUSION CONCEPTS

Introduction

Recently there has been considerable interest in the potential for using energetic ion beams to initiate thermonuclear burn in fusion pellets. The incentives for this interest are the fact that accelerator technology is well advanced and that interactions between energetic charged particles and

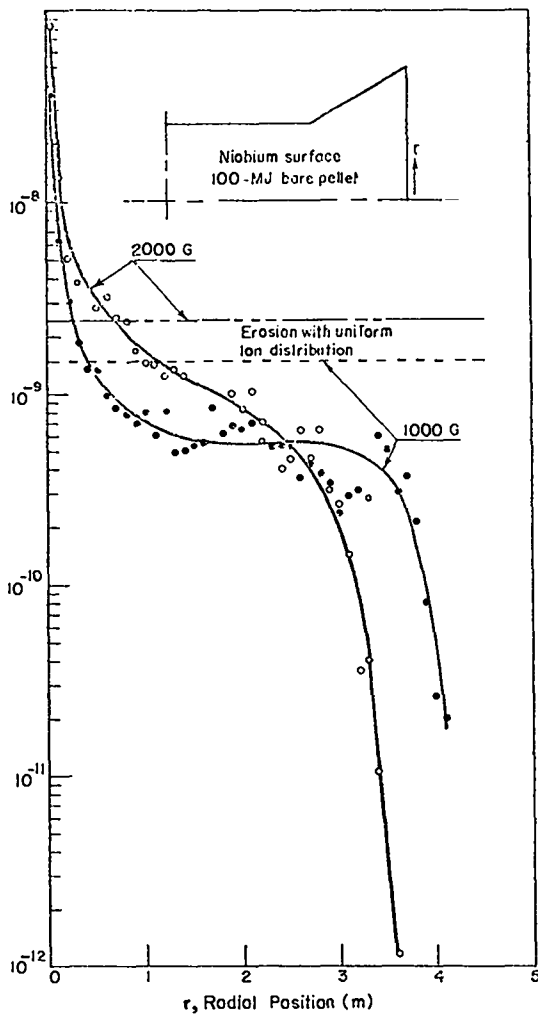


Fig. 77. Sputtering erosion per pellet microexplosion of a flat-plate energy sink.

matter are well understood. The same sophisticated computer codes and other theoretical tools that have been developed for use in laser and electron beam fusion research can also be used to study ion-beam fusion.

Another area of commonality between the various approaches to commercial application of pellet fusion is the necessity for a reaction cavity to contain the pellet microexplosions and to permit recovery of the fusion energy in a form that is convenient for conversion to electricity. Some of our researchers participated in the ERDA-sponsored Ion-Beam Fusion Summer Study (Berkeley, July 19-30, 1976) and contributed to the development of reactor cavity concepts. The concepts that evolved

are adaptations of those that have been studied previously for laser-initiated pellet fusion. One of these concepts has since been analyzed more carefully. The results are discussed below.

Fusion Pellet Output Characterization

One of the disadvantages anticipated in commercial applications of ion-beam fusion is the large capital investment required for the accelerators. It is therefore thought that commercial competitiveness for ion-beam fusion can only be achieved from the use of high-gain fusion pellets. Fusion pellet yields in the range 400 to 4000 MJ were considered at the summer study.

The output characteristics of a 3000-MJ pellet microexplosion were provided to the summer study by the Lawrence Livermore Laboratory for use in analyses of cavity-wall protection schemes.

Cavity-Wall Protection Concept

Several cavity-wall protection schemes have been investigated and found suitable for laser fusion reactors. The most attractive of these employ either a replenishable film of liquid metal to absorb the energy of the x rays and pellet debris (wetted-wall reactor concept) or magnetic fields to divert ionized pellet debris away from cavity walls onto energy-sink surfaces (magnetically protected reactor concept). Neither of these schemes may be suitable for ion-beam fusion.

It may be necessary to maintain a high vacuum in the cavity to efficiently transmit and focus the ion beams onto the fusion pellet, which would prevent the use of a protective liquid-metal film, part of which would be vaporized by each pellet microexplosion. The stability of the ion beam in traversing the cavity may be adversely affected by even very weak magnetic fields, which suggests that it may not be permissible to introduce extraneous magnetic fields to divert the pellet debris from cavity walls. We therefore considered cavity concepts for which interior wall protection is provided by a solid ablative material.

Desirable properties of the ablative material are: low Z (sputtering yields decrease and x-ray penetration depths increase as the atomic number decreases), high thermal conductivity and heat capacity, high temperature capability (to maxi-

mize heat transfer and minimize evaporation during energy deposition), low cost, and ease of fabrication. These properties are satisfied best by carbon, and carbon was therefore assumed as the ablative liner for ion-beam-fusion reactor cavities.

Calculation of Cavity-Wall Surface Evaporation and Sputtering Rates

During the Summer Study, preliminary calculations were made of evaporation rates due to energy deposition by x rays and pellet debris from the 3000-MJ fusion-pellet microexplosion described above. The results indicated that carbon evaporation rates in a 10-m-diam cavity would be acceptable and would result in a reasonable cavity lifetime at reasonable cost. In comparison, sputtering of the liner by impinging pellet debris was thought not to be significant.

Since then, we have analyzed in greater detail both evaporation and sputtering for this cavity design and pellet output. In addition to carbon-lined cavities, we also considered cavities with bare metal walls. The cavity wall materials and their properties for which calculations were made are listed in Table IX.

Energy-dependent energy deposition distributions in the cavity wall were calculated for x rays and ions in the pellet debris. Time-dependent surface temperatures and temperature distributions were calculated with a computer program written for

this purpose, which also includes calculations of evaporation based on Langmuir theory with Arrhenius expressions for vapor pressure as functions of temperature.

For calculation of sputtering by energetic ions, we used the sputtering model that was developed previously. Because experimental data are not available for the ion-target combinations being considered, theoretical predictions of sputtering yields developed by P. Sigmund³ were used in the analysis. (Where experimental data are available for comparison, Sigmund's theory overestimates sputtering yields by a factor between 2 and 5.)

Our results for evaporation rates of cavity wall materials are qualitatively consistent with the results obtained by the Summer Study group and would not unduly limit cavity wall lifetimes. However, cavity wall erosion is dominated by sputtering. Sputtering for the refractory metals is much more severe than for the graphites, whose sputtering is even much too severe to be acceptable for commercial applications.

Many other questions relating to ion-beam fusion cavity designs must obviously be considered. For example, the ultimate disposition of sputtered and evaporated material has not been studied. Presumably, much of it will recondense on the cavity wall, and the remainder, together with part of the pellet debris, will be pumped from the cavity. Relaxation of the cavity conditions imposed by re-

TABLE IX
ION-BEAM-FUSION CAVITY WALL MATERIALS

<u>Material</u>	<u>Density (g/cm³)</u>	<u>Thermal Conductivity at 2500 K (W/cm·K)</u>	<u>Heat Capacity (cal/g·K)</u>	<u>Melting Point (K)^b</u>	<u>Remarks</u>
Pyrolytic graphite	2.24	1.9 ^a	0.52	--	Expensive, highly anisotropic
ATJ graphite	1.73	0.34	0.52	--	Relatively inexpensive, slightly anisotropic
Niobium	8.57	0.82	0.087	2770	Expensive, limited resource
Molybdenum	10.24	0.86	0.098	2890	Inexpensive, difficult to fabricate, plentiful

^aConductivity along crystal planes.

^bThe graphites do not melt at ordinary pressures; however, they do have finite vapor pressures at elevated temperatures.

quirements for transmitting and focusing ion beams may permit consideration of other cavity-wall protection schemes, and there may be improvements in cavity-wall performance due to specifically optimized fusion-pellet designs.

The reactor blanket also requires much attention. Questions relating to tritium breeding and structural integrity should be addressed.

In addition to these technical questions, a complete assessment of ion-beam fusion will require systems studies and economic analyses.

FUSION PELLETT OUTPUT PARAMETER STUDIES

We have acquired the one-dimensional computer code LACER for calculating fusion-pellet output characteristics. This code is being used in parameter studies investigating the effects of variations in structural materials in pellets on relative yields and energy spectra of x rays, neutrons, and pellet debris. The results of these pellet-output parameter studies will be used to select pellet designs for military applications and in reactor design and system tradeoff studies to select acceptable pellets for commercial applications.

SYSTEMS ANALYSIS COMPUTER PROGRAM DEVELOPMENT

Commercial Applications

We have acquired the computer code CONCEPT that had been written for ERDA⁴ to perform cost estimates of conceptual steam electric power plants. This code is being adapted to run on our

computers, and the necessary modifications have been essentially completed. A cost-estimating subroutine and data file for laser fusion generating stations will be incorporated in the code, permitting us to make cost estimates that are consistent with standard methodology.

Multipurpose Materials Testing and Weapons Research Facilities

A systems analysis computer program is being written for the design and evaluation of new facilities and/or modification of existing facilities for materials testing and weapons-related research. Because the criteria for evaluating such facilities will be totally different from those used to evaluate commercial applications, a completely new systems code is required. The initial draft of this code will be restricted to the calculation of capital costs. Use is being made of the design and costing information being developed for the HEGLF and of the costing data bases included in the computer code CONCEPT.⁴

REFERENCES

1. F. Skoberne, Los Alamos Scientific Laboratory report LA-6050-PR (January 1976).
2. E. Stark and F. Skoberne, Los Alamos Scientific Laboratory report LA-6510-PR (November 1976).
3. P. Sigmund, Phys. Rev. 184, 383-416 (1969).
4. S. T. Brewer, compiler, U S Energy Research and Development Administration report ERDA-108 (June 1975).

VII. RESOURCES, FACILITIES, AND OPERATIONAL SAFETY



The design of HEGLF Facilities continued. Safety policies and procedures continued to be applied to successfully minimize hazards of operating high-energy lasers. Final results of corneal damage-threshold experiments with Nd:YAG, HF, and CO₂ pulsed lasers are reported.

MANPOWER DISTRIBUTION

The distribution of employees assigned to the various categories of the ERDA-supported Laser Fusion Research Program is shown in Table XI.

FACILITIES

HIGH-ENERGY GAS LASER FACILITY (HEGLF)

A review of the Architect-Engineer's design effort at the 30%-point of Title II in early December 1976 disclosed that the design, in general, was progressing well, on schedule. Only the design of electrical installations was lagging somewhat, and this effort is being increased.

In the interest of continuity, we have presented details in HEGLF building design and construction in Section I.

OPERATIONAL SAFETY

General

No incident involving biological damage from laser radiation occurred. Changes in the ANSI 136.1 Standard for "Safe Use of Lasers" were recommended in the Medical Surveillance Section to eliminate unnecessary fundus photography in eye examinations.

The protective-eyewear development program recently completed now specifies corrective lenses

TABLE XI
APPROXIMATE STAFFING LEVEL OF LASER PROGRAM
SEPTEMBER 30, 1976

<u>Program</u>	<u>Direct Employees</u>
Glass Laser Systems Development	1
CO ₂ Laser System Development	100
New Laser Systems R & D	18
Pellet Design & Fabrication	47
Laser Target Experiments	42
Diagnostics Development	25
Systems Studies & Applications	7
Electron-Beam Target Design & Fabrication	1
TOTAL	<u>241</u>

from a variety of Schott Optical Co. filter glasses for lightweight spectacles of high luminous transmission to be used with specific wavelength ranges in the uv, visible, and ir.

Biological Damage-Threshold Studies

A summary of biological damage-threshold values obtained in our laser laboratories to date is presented below.

<u>Laser</u>	<u>Wavelength (μm)</u>	<u>Pulsewidth (s)</u>	<u>Threshold Damage (mJ/cm²)</u>	<u>Organ</u>	<u>Principal Investigator</u>
Nd:YAG	1.06	3.0 x 10 ⁻¹¹	1.1 x 10 ³ ^a	Eye (Retina)	Ham, Virginia Commonwealth U.
Nd:YAG (dbl)	0.53	3.0 x 10 ⁻¹¹	6.5 x 10 ³ ^b	Eye (Retina)	Ham, Virginia Commonwealth U.
HF	2.7	1.0 x 10 ⁻⁷	6 - 10	Eye (Cornea)	Ham, Virginia Commonwealth U.
HF	2.7	1.0 x 10 ⁻⁷	300 ^c	Skin	Rockwell, University of Cincinnati
CO ₂	10.6	1.4 x 10 ⁻⁹	20	Eye (Cornea)	Ham, Virginia Commonwealth U.
CO ₂	10.6	1.4 x 10 ⁻⁹	230 ^c	Skin	Rockwell, University of Cincinnati

^aEnergy incident on cornea, 9 x 10⁻⁶J.

^bEnergy incident on cornea, 18 x 10⁻⁶J.

^cMinimal reactive dose, 50% probability.

VIII. PATENTS, PRESENTATIONS, AND PUBLICATIONS



PATENTS ISSUED

- U S Patent 3 973 213, issued August 3, 1976. "Compact, High Energy Gas Laser," inventors Stephen D. Rockwood, Robert E. Stapleton, and Thomas F. Stratton.
- U S Patent 3 980 397, issued September 14, 1976. "Diffraction Smoothing Aperture for an Optical Beam," inventors O'Dean P. Judd and Bergen R. Suydam.

PRESENTATIONS

The following presentations were made at The Third Summer Colloquium on Electronic Transition Lasers, Aspen, CO, September 7-10, 1976.

- O. P. Judd, "Electron-Collisional Excited State Kinetics in Argon and Mercury Electrical Discharges."
- W. M. Hughes, "Molecular Krypton Kinetics."
- I. J. Bigio, "Radioactive-Source Preionization of Visible and UV Discharge Lasers."
- R. J. Carbone and G. W. York, "Electrical and Optical Properties of a High Pressure Transverse Hg Discharge."

The following papers were presented at the 8th Annual Symposium on Optical Materials for High Power Lasers, National Bureau of Standards, Boulder, CO, July 13-15, 1976.

- D. H. Gill and B. E. Newnam, "Spectral Dependence of Damage Resistance of Refractory Oxide Optical Coatings."
- J. H. Apfel, D. H. Gill, J. S. Matteucci, and B. E. Newnam, "The Role of Electric-Field Strength in Laser Damage of Dielectric Multilayers."
- J. J. Hayden, "Measurements at 10.6 μ m of Damage Threshold in Germanium, Copper, Sodium Chloride, and other Optical Materials at Levels up to 10^{10} W/cm²."

In addition, the following presentations were made at various institutions.

- A. J. Campillo and S. L. Shapiro, "Use of Picosecond Lasers for Studying Photosynthesis," SPIE 20th Annual Technical Symposium (August 23-27, 1976).
- J. Terrell, "Size Limits for Expanding Light Sources," IAU-CNRS Colloquia, Paris, France (September 6-9, 1976).
- O. P. Judd, "Recent Developments in Lasers, and Related Applications to Biology," Gordon Research Conference on Lasers in Medicine and Biology, Kimball Union Academy, Meriden, NH (July 5-9, 1976).
- M. J. Nutter, "Computer Assisted Data Collection, Retrieval, and Control System for the LASL 2.5-kJ, 1-ns CO₂ Laser System," Cube Symposium, Albuquerque, NM (October 26-28, 1976).
- S. Singer, "Optics in Terawatt CO₂ Lasers," Electro-Optics Laser Conference and Exposition, New York, NY (September 14-15, 1976).
- T. G. Frank, "Laser Fusion Hybrid Reactors," invited paper presented at US-USSR Symposium on Fusion-Fission Reactors, Livermore, CA (July 13-16, 1976).
- L. A. Booth, I. O. Bohachevsky, T. G. Frank, and J. H. Pendergrass, "Heat Transfer Problems Associated with Laser Fusion," invited paper presented at 16th Nat. Heat Transfer Conf., St. Louis, MO (August 8-11, 1976).
- L. A. Booth, "Commercial Applications of Laser Fusion," invited paper presented at Advisory Group Meeting on the Technology of Inertial Confinement Experiments, Dubna, USSR (July 19-23, 1976).

L. A. Booth and T. G. Frank, "A Technology Assessment of Laser Fusion Power Development," invited paper presented at 2nd ANS Topical Meeting on the Technology of Controlled Nuclear Fusion, Richland, WA (September 21-23, 1976).

A. G. Engelhardt, "Useless Physics," based on work done to August 15, 1975, University of Illinois Gaseous Electronics Laboratory.

A. Lieber, D. Sutphin, C. Webb, and A. Williams, "Sub-Picosecond X-Ray Streak Camera Development for Laser-Fusion Diagnostics," 12 International Congress on High Speed Photography, Toronto, Canada (August 1-7, 1976).

A. Lieber, D. Sutphin, and C. Webb, "Pico-Second Proximity Focused X-Ray Spectra, National Bureau of Standards, Gaithersburg, MD (August 30-September 2, 1976).

A. Lieber, D. Sutphin, and C. Webb, "Sub-Picosecond Proximity Focused Streak Camera for X-Ray and Visible Light," SPIE 20th Annual Technical Symposium, San Diego, CA (August 23-27, 1976).

W. H. Reichelt, "Mirror and Window Materials for CO₂ Laser Systems," invited talk given at NBS Laser Damage Symposium, Boulder, CO (July 13-15, 1976).

PUBLICATIONS

(This list of publications is prepared by computer from a stored data base. It has been checked for accuracy, but there may be typographical inconsistencies.)

Devaney, Joseph J.; "Very High Intensity Reaction Chamber Design. 2. Stable Resonator Etalon." LASL, 1976. 17P. (LA-6124-MS, Vol. II).

Skoberne, Frederick; "Laser Fusion Program, July 1 - December 31, 1975." LASL, 1976. 11&P. (LA-6245-PR).

Henderson, Dale B.; Stroschio, Michael A.; "Comment on Energy Deposition in Laser Heated Plasmas." LASL, 1976. 2P. (LA-6393-MS).

McCrorry, Robert L.; Morse, Richard L.; "Dependence of Laser-Driven Compression Efficiency on Wavelength." LASL, 1976. 3P. (LA-6420-MS).

Stratton, Thomas F.; "Carbon Dioxide Short Pulse Laser Technology." High-Power Gas Lasers. 1975. Summer School, Capri. Lectures, P.284-311. Institute of Physics, London, 1976.

Gitomer, Steven J.; Adam, J. C.; "Multibeam Instability in a Maxwellian Simulation Plasma." Phys. Fluids, V.19, P.719-22. 1976.

Boyer, Keith; "Overview of Laser Fusion." Laser Induced Fusion and X-Ray Laser Studies, S. F. Jacobs, Ed., Physics of Quantum Electronics, V.3, P.1-12. Addison-Wesley, 1976.

Judd, O'Dean P.; "Lasers Based on the O(¹S) to O(¹D) Transition in Atomic Oxygen." TIC, 1976. 16P. High-Power Gas Lasers. 1975. Summer Institute of Physics, London, 1976. School, Capri. Lectures, P.313-20.

Judd, O'Dean P.; "Interaction of Pulsed Optical Radiation with an Inverted Medium." High-Power Gas Lasers. 1975. Summer Institute of Physics, London, 1976. School, Capri. Lectures, P.45-57.

Judd, O'Dean P.; "Fundamental Kinetic Processes in the Carbon Dioxide Laser." High-Power Gas Lasers. 1975. Summer Institute of Physics, London, 1976. School, Capri. Lectures, P.29-44.

Boyer, Keith; "Laser Isotope Separation Overview." Laser Photochemistry, Tunable Lasers, and Other Topics, S. F. Jacobs, Ed., Physics of Quantum Electronics, V.4, P.1-9. Addison-Wesley, 1976. (535: L343P).

Bigio, Irving J.; Begley, Richard F.; "High Power, Visible Laser Action in Atomic Fluorine." Abstract published in: Opt. Commun., V.18, P.1&3-4. 1976.

McCall, Gene H.; "Laser Fusion - Diagnostics and Experiments." Laser Induced Fusion and X-Ray Laser Studies, S. F. Jacobs, Ed., Physics of Quantum Electronics, V.3, P.251-76. Addison-Wesley, 1976.

Bigio, Irving J.; Begley, Richard F.; "High Power Visible Laser Action in Neutral Atomic Fluorine. Erratum." Appl. Phys. Lett., V.28, P.691. 1976.

Elliot, C. James; Feldman, Barry J.; "Multiple Photon Excitation and Dissociation of Molecules with Short Laser Pulses." Abstract published in: Opt. Commun., V.18, P.72. 1976.

Feldman, Barry J.; Fisher, Robert A; McLellan, Edward J.; Thomas, Scott J.; "Free Induction Decay Generation of 10.6 - Micrometer Subnanosecond Pulses." Abstract published in: Opt. Commun., V.18, P.72. 1976.

Sollid, Jon E.; Sladky, R. E.; Reichelt, Walter H.; Singer, Sidney; "Figure Evaluation of Large Single Point Diamond-Turned Copper Mirrors." Appl. Opt., V.15, P.16568.

Thode, Lester E.; "Plasma Heating by Relativistic Electron Beams: Experiment, Simulation and Theory." Abstract published in: Bull. Am. Phys. Soc., Ser.2, V.21, P.532. 1976.

Ganley, James T.; Leland, Wallace T.; Bentley, Bill.; Thomas, Arlo J.; "Measurement of Potential Distribution and Cathode Fall in Electron Beam Sustained Discharges." TIC, 1976. 6P. MN.

Giovanielli, Damon V.; "Spectra and Angular Distributions of Electrons Emitted from Laser-Produced Plasmas." J. Appl. Physics, V.47, P.2907. 1976.

Czuchlewski, Stephen J.; Ryan, Stewart R.; "Metastable Hydrogen Atom Detector Suitable for Time-of-Flight Studies." Rev. Sci. Instrum., V.47, P.1026. 1976.

Leland, W. T.; Kircher, M. J.; "Gain Uniformity in Large-Aperture Electron-Beam-Stabilized CO₂ Amplifiers." LASL, 1976. 9P. (LA-6493-MS).